1981

The effect of scattering and absorption on noise from a cavitating noise source in subsurface ocean layer.

Tronstad, Yngnar Dag

Monterey, California. Naval Postgraduate School

http://hdl.handle.net/10945/20506

THE EFFECT OF SCATTERING AND ABSORPTION ON NOISE FROM A CAVITATING NOISE SOURCE IN SUBSURFACE OCEAN LAYER

Yngnar Dag Tronstad

NAVAL POSTGRADUATE SCHOOL
Monterey, California

THESIS

THE EFFECT OF SCATTERING AND ABSORPTION
ON NOISE FROM A CAVITATING NOISE SOURCE
IN THE SUBSURFACE OCEAN LAYER

by

Yngvar Dag Tronstad

June 1981

Thesis Advisor: K. E. Woehler

UNCLASSIFIED

SECURITY CLASSIFICATION OF THIS PAGE (When Data Entered)

REPORT DOCUMENTATION PAGE		READ INSTRUCTIONS BEFORE COMPLETING FORM
1. REPORT NUMBER	2. GOVT ACCESSION NO.	3. RECIPIENT'S CATALOG NUMBER
4. TITLE (and Subtitle) The Effect of Scattering and Absorption on Noise from a Cavitating Noise Source in the Subsurface Ocean Layer		5. TYPE OF REPORT & PERIOD COVERED Master's thesis; June 1981
		6. PERFORMING ORG. REPORT NUMBER
7. AUTHOR(s) Yngvar Dag Tronstad		8. CONTRACT OR GRANT NUMBER(s)
9. PERFORMING ORGANIZATION NAME AND ADDRESS Naval Postgraduate School Monterey, California 93940		10. PROGRAM ELEMENT, PROJECT, TASK AREA & WORK UNIT NUMBERS
11. CONTROLLING OFFICE NAME AND ADDRESS Naval Postgraduate School Monterey, California 93940		12. REPORT DATE June 1981
		13. NUMBER OF PAGES 176 pages
14. MONITORING AGENCY NAME & ADDRESS(if different from Controlling Office)		15. SECURITY CLASS. (of this report) Unclassified
		15a. DECLASSIFICATION/DOWNGRADING SCHEDULE

16. DISTRIBUTION STATEMENT (of this Report)

Approved for public release; distribution unlimited

17. DISTRIBUTION STATEMENT (of the abstract entered in Block 20, if different from Report)

Approved

18. SUPPLEMENTARY NOTES

19. KEY WORDS (Continue on reverse side if necessary and identify by block number)

Scattering, absorption, rough sea surface, inhomogeneous bubble-dominated subsurface layer, torpedo, turn rate limitation, cavitating propeller, square law detector.

20. ABSTRACT (Continue on reverse side if necessary and identify by block number)

When investigating the detection performance of a passive homing torpedo used against shallow draft surface ships, certain environmental factors such as the rough sea surface and the bubble-dominated inhomogeneous layer near the sea surface have to be considered. This thesis attempts to gain some insight into the behavior of a homing torpedo system during its critical attack phase, as well as getting some indications of the relative importance of the scattering mechanisms and the induced tactical

DD FORM 1473, 1 JAN 73 EDITION OF 1 NOV 65 IS OBSOLETE
S/N 0102-014-6601 |

UNCLASSIFIED

SECURITY CLASSIFICATION OF THIS PAGE (When Data Entered)

limitations. An idealized propagation model was used as reference of comparison. For a given sea state and target speed, the results stress the importance of low operating frequency as well as a high maximum turn rate. They also point to the importance of having a search depth below the bubble-dominated subsurface layer, and a variable speed capability during the torpedo's attack phase.

The Effect of Scattering and Absorption on Noise from a Cavitating Noise Source in the Subsurface Ocean Layer

by

Yngvar Dag Tronstad
Commander, Norwegian Navy
Marine Engineer, Norwegian Naval Academy, 1969

Submitted in partial fulfillment of the requirements for the degree of

MASTER OF SCIENCE IN ENGINEERING ACOUSTICS

from the

NAVAL POSTGRADUATE SCHOOL
June 1981

ABSTRACT

When investigating the detection performance of a passive homing torpedo used against shallow draft surface ships, certain environmental factors such as the rough sea surface and the bubble-dominated inhomogeneous layer near the sea surface have to be considered. This thesis attempts to gain some insight into the behavior of a homing torpedo system during its critical attack phase, as well as getting some indications of the relative importance of the scattering mechanisms and the induced tactical limitations. An idealized propagation model was used as reference of comparison. For a given sea state and target speed the results stress the importance of low operating frequency as well as a high maximum turn rate. They also point to the importance of having a search depth below the bubble-dominated subsurface layer, and a variable speed capability during the torpedo's attack phase.

TABLE OF CONTENTS

LIST OF TABLES

LIST OF FIGURES

ACKNOWLEDGMENT

The author wishes to gratefully express his appreciation to his advisor, Professor Karlheinz E. Woehler, for his advice, encouragement and guidance in the preparation of this thesis.

I. INTRODUCTION

The following analysis examines several factors that limit the detection performance of a passive homing torpedo with the mission objective of countering shallow-draft targets in Norwegian coastal waters. Generally, these factors can be divided into three main groups:

- -Environmental factors in the ocean
- -Electrical mechanical and hydrodynamical factors in the torpedo system
- -The users tactical situation

The factors that are generated in the ocean itself are the principal subject of this analysis. As our interest is confined to the layer immediately below the surface of the ocean, later called the subsurface ocean layer, the main factors affecting the sound propagation are:

- -Scattering and absorption due to the bubble-dominated inhomogeneous subsurface ocean layer.
- -Scattering from the rough sea surface

The concentration of air bubbles and the roughness of the sea surface are determined by the windspeed. The effectiveness of both these scattering mechanisms depends on the frequency of the incident wave and the geometry of the source and receiver. The following analysis is limited to

high frequencies in the region of 30-60 kHz which are characteristic of existing torpedo systems. At high frequency and low grazing angles for the incident and received signals, the phenomena of "shadowing" of the surface by other parts of the boundary occurs. Under these conditions, the effect from the inhomogeneous subsurface ocean layer becomes increasingly important. Obviously both the above mentioned scattering mechanisms are present simultaneously. Often these two effects cannot be resolved either theoretically or experimentally, as any signal with a finite duration will be scattered from the space near the surface simultaneously with that from the sea surface itself.

In order to adequately describe the scattering mechanisms, this analysis starts with a presentation of the oceanographic background material for:

- Typical windspeed and wave height
- Typical sound speed profiles
- Density and distribution of air bubbles in the subsurface layer
- Statistical description of the sea surface

The analysis proceeds by separately estimating the effect of:

- Scattering from a randomly rough surface
- Scattering and absorption caused by an inhomogeneous subsurface layer,

and comparing their relative importance. The method employed for these estimations is an approximation that is a combination of both ray and wave theories. Ray methods are used to follow the acoustic signal from its source to the vicinity of the scatterer. Wave theory is used to calculate the actual scattering process. Finally, ray theory is again used to follow the scattered signal to the receiver.

An idealized propagation model consisting of an isotropic stratified medium will be used as reference of comparison. This model is founded on:

-A noise source from a cavitating propeller blade.

-The operational characteristics for a square law detector (ROC-curves).

-A transmission loss model based on geometrical spreading and absorption losses in homogeneous sea water.

In this analysis, the passive sonar equation is used to predict the performance of the homing system. The detection range encountering the two scattering effects will be obtained from the sonar equation and compared to the detection range based on the reference model. Thus, the difference in ranges at which the homing device just acquires the target with and without scattering is a measure of efficiency.

II. SCENARIO AND TORPEDO RUN GEOMETRY

In the Norwegian coastal waters, the primary mission of a torpedo system is to counter an amphibious force consisting of escorts, supply ships, and shallow-draft landing crafts. Typical characteristics of these three ship types are as follows:

Supply ships:

- -Displacement 5000 tons
- -Length 100 m.
- -Draft 6 m.
- -Speed 15-20 kts.

Escort ships:

- -Displacement 2000-3000 tons
- -Length 85 m.
- -Draft 3 m.
- -Speed 35 kts.

Landing craft:

- -Displacement 1000 tons
- -Length 80 m.
- -Draft 2 m.
- -Speed 18 kts.

In order to simplify this analysis, moderate sea states (SS 3) are assumed. Since "moderate" wave heights of two meters

are appreciable when compared with the two-meters draft of the landing craft, the possibility of an acoustic torpedo impacting the target at a depth of two meters is very remote without the use of an influence exploder.

Two relevant search and attack schemes will be considered. These are illustrated in Fig. 1 together with the operation of the influence exploder. From target validation to completion of terminal attack, the torpedo continuously tracks in the azimuth plane. In Case A, ascent is inhibited after enable. For Case B, ascent is inhibited after the torpedo reaches terminal attack depth.

An assumed attack depth of six meters is consistent with the activation range of influence exploders and is deep enough to preclude wave or "free surface" induced disturbances of the torpedo. Success of the attack depends primarily on the availability of maintaining azimuth-plane steering to within a short horizontal range of the target, and the subsequent operation of the influence exploder.

Case A is of particular interest to this analysis, as both the search and attack-depth are within the subsurface layer.

III. OCEANOGRAPHIC BACKGROUND MATERIAL

The oceanographic background for predicting typical and extreme conditions of

-wind speed

-wave heights

-bubble densities and distributions

-ambient noise versus self noise

-sound speed profiles

are outlined in detail in Appendix A. Even though most data have beneral validity for Norwegian coastal waters, the region above 68°N are of particular interest. Thus, a typical area combining open as well as confined waters can be represented by "Andfjord" at 70°N, where the oceanographic conditions can be related to the weather station "Andenes," see Fig. 2.

Figures 3 and 4 [Ref. 1] show average windspeed and the occurrence of significant wave heights as a function of time of year at weather station "Andenes," respectively. The bulk of data is centered around a windspeed of Beaufort:4-5 (11-21 kts) and SS:3-4 (significant wave heights: 1-2 m). Table I gives the relationship between SS, windspeed and expected significant wave heights.

TABLE I

RELATIONSHIP BETWEEN SEA STATE (SS), WIND SPEED, AND EXPECTED SIGNIFICANT WAVE HEIGHTS (H_s)

Class Number SS	Significant Wave Height in m H_s	Beaufort Scale
0	0	0
1	0 - 0.1	1
2	0.1 - 0.5	2
3	0.5 - 1.25	3-4
4	1.25 - 2.5	5
5	2.5 - 4.0	6-7
6	4.0 - 6.0	8
7	6.0 - 9.0	9-10
8	9.0 - 14.0	11
9	>14	12

This, together with the low probability of having an amnibious operation occurring in high sea states (SS>5) justifies the assumption of moderate sea state with windspeed in the region of 12 kts and wave heights of 2 m.

The bubble data distribution taken from Ref. 2 was obtained in the area "Tromsö" - "Björnöya" during the period June-November 1978. These data correlate very well with a larger body of data obtained by H. Medwin [Ref. 3].

Figures 5, 6 and 7 [Ref. 2] show the density of resonant bubbles as a function of depth with windspeed as parameter for the 12, 38 and 120 kHz. As seen from these figures, the number of resonant bubbles are an increasing function of frequency and windspeed, and a decreasing function of depth. Below a depth of approximately 15 m, the number of bubbles is negligible for the windspeed of interest.

The effect of SS (windforce) on the ambient noise level is given in Fig. 8 [Ref. 4]. Shallow coastal Norwegian waters are typically 5-10 dB noisier than the corresponding deep water. However, great variability caused by local ship traffic, fishing fleet activity, marine life and local wind conditions makes ambient noise prediction difficult in these areas. This means that for accurate modeling, ambient noise prediction have to be done at each location as its level is both site and time dependent. However, Fig. 8 shows that for frequencies higher than 50 kHz, the

effect of windforce on the ambient noise level decreases to a lower bound determined by the thermal agitation. Based on the above discussion and experience related to noise levels for torpedo systems, the self noise will be assumed to be dominant through this analysis.

Figure 9, obtained from Ref. 5, shows that the sound speed profiles usually encountered in the area of interest results in extremely difficult sonar conditions. This is illustrated in Figs. 10 and 11, which show worst-case ray path derived from Fig. 9. In addition, the presence of bubbles in the subsurface layer causes the sound speed to be a function of frequency. The above two factors may frequently be the ones limiting the detection range of the torpedo. These effects can be minimized by selecting an appropriate search depth for a particular sound speed profile. In addition, for Case B the corresponding curved homing trajectories in the pitch plane give an error in apparent range to target. This effect will normally be taken into account by devising appropriate attack logic which is outside the scope of the present analysis.

IV. THE PASSIVE SONAR EQUATION

A measure of efficiency for a passive homing torpedo is the detection range obtained by solving the passive sonar equation for broadband noise:

$$SL+10\log B-TL(geom)-\alpha R+DI-NL-DT=0 \qquad (1)$$

where

SL = spectral level of the broadband noise radiated by the target (in dB re 1uPa/1Hz at 1m).

R = detection range (in m).

α = attenuation coefficient at the center frequency (in dB/m).

DI = receiving sensitivity (directivity index) (in dB re 1μPa).

NL = noise level at the receiver in the bandwidth B (in dB re 1μPa).

DT = detection threshold; the signal to noise ratio at the transducer output required for a detection probability of p_D and associated false alarm probability p_{FA} (in dB).

V. REFERENCE MODEL

A. INTRODUCTION

In order to produce the reference for the analysis the sonar equation is solved assuming ideal free-field conditions, a simple noise source model, and a generalized square-law detector.

B. IDEALIZER TRANSMISSION LOSS MODEL

Because the presence of refraction, scattering, and of ocean boundaries, free-field conditions associated with homogeneous (isovelocity) and unbounded medium seldom exist in the sea. However, as a basis for comparison, the ubigutuous spherical spreading law plus an added loss term due to "normal absorption" can be used as a reference model for measuring the effects of the previous mentioned scattering and absorption mechanisms. Thus, the reference transmission loss model can be expressed as:

$$TL = 20 \log R + \alpha R \tag{2}$$

where the absorption coefficient, expressed in dB/m, can be obtained from Fig. 14 taken from Ref. 8.

C. NOISE SOURCE MODEL

1. General Characteristics of Noise Sources

Sound is generated in a fluid medium by any process that causes an unsteady pressure field. Physically processes that can cause an unsteady pressure field include:

- Pulsation of a boundary surface of the medium
- The action of a nonsteady source on the fluid
- Turbulent motion in the fluid
- Oscillatory temperatures

It can be shown, e.g., Ref. 10, that each source mechanism mathematically corresponds to a dominant order of multipole. If all sources are of such a nature that their time variation can be described by a Fourier Integral, it can be shown [Ref. 10] that the Helmholtz Equation is

$$\nabla^2 p_\omega(x) + \frac{\omega^2}{C^2} p_\omega(x) = -4\pi f_\omega(x) \qquad (3)$$

$$= \underbrace{\frac{\partial Q_\omega(x)}{\partial t}}_{\text{Term 1}} + \underbrace{\nabla \cdot F_\omega(x)}_{\text{Term 2}} - \underbrace{\frac{\partial^2 T_{\omega ij}}{\partial x_i \partial x_j}}_{\text{Term 3}}$$

where the right hand side describes distributed source terms.

The terms on the right hand side of Eq. (3) have the following interpretations:

Term 1: mass injection

Term 2: external force

Term 3: turbulent shear stress

In the long distance and long wavelength approximation, it can be shown that the mass injection term gives rise to a simple source; a zero order pole called a monopole. The monopole radiates omnidirectional with no angular dependence. At large distances the pressure field from the monopole radition is that of a point source. Examples of this are:

-Pulsating bubbles

-Cavitation

The external force, in the long distance and long wave length approximation, is associated with a dominant dipole which has a cosine directional pattern. Examples of this type of radiation is that caused by the vibratory motion of an unbaffled rigid body.

Radiation from turbulent shear stresses is characterized by a lowest order term of quadrupole nature.

The efficiency of the source terms decreases with increasing dependence on the spatial derivatives. This can be understood when recognizing that wave functions of the general form f(x-ct) have a time derivative

$$\left|\frac{\partial}{\partial t} f(x-ct)\right| = cf_t(x-ct) \tag{4}$$

which is magnitude c (sound speed) greater than the spatial derivative

$$\left|\frac{\partial}{\partial x} f(x-ct)\right| = f_x(x-ct) \tag{5}$$

Other factors being equal, the radiation from an external force is small compared to that from mass injection, and that from turbulent shear stress is the smallest; therefore, monopole radiation is the dominant term.

Propeller cavitation, when it occurs, is usually the dominant noise source for any marine vessel. Submarine and torpedoes often operate at a depth great enough to avoid cavitation. Surface ships, on the other hand, generally have well developed propeller cavitation with the result that their radiated spectrum from 5 Hz to 100 kHz is controlled by this source.

The basic phenomena of cavitation combined with propeller hydrodynamics give the fundamental characteristics of propeller cavitation noise. An excellent qualitatively discussion of this can be found in Ref. 9:Chs. 7 and 8, from which the following is extracted:

> Propeller blades are rotating twisted wings that produce hydrodynamic forces. Depending on operating conditions, they experience cavitation on a number of different places. Of these there are three prominent types:
>
> -Tip vortex cavitation
>
> -Hub vortex cavitation
>
> -Surface blade cavitation

In addition to the two types of vortex cavitation, there normally are two types of blade surface cavitation:

-Back: driving face

-Front: suction surface

Of all kinds of propeller cavitation, surface blade cavitation on the suction surface is normally the most noisy, while hub vortex cavitation is the least noisy.

2. The Noise Source Model

Due to lack of recorded and available noise data from the target in question, the noise source has been generalized on the basis of the following discussion and assumptions:

The noise source will be build up around a surface blade cavitating propeller operating in a good to poor wake; surface cavitation will be assumed to be dominant.

D. Ross [Ref. 9] has developed an approximate theory for cavitation noise, where dimensional analysis is combined with the basic results of cavitation theory that the acoustic pressure is proportional to the product of the collapse pressure of the cavities and the volume of cavitation produced per unit time. From this synthesis it is found that the total acoustic intensity varies as:

$$I \approx K_{ti} \frac{p_o bsD(U_{ti})^3}{r^2} \left[\left(\frac{U_t}{U_{ti}}\right) \left(\frac{U_t}{U_{ti}} - 1\right)^2 \right] \qquad (6)$$

where

r = distance of the hydrophone from the source

K_{ti} = the cavitation inception parameter

U_t = blade tip speed

U_{ti} = blade tip speed for inception of cavitation

This expression shows that propeller cavitation noise power is proportional to the total number of blades, b, the blade chord, s, and to the propeller diameter, D, and is a function of the tip speed with the dependence on the tip speed being the strongest. The different blade surface sections where cavitation exist are uncorrelated and the radiated noise is treated as a single monopole radiation so that at a distance r>>a (where a is the characteristic dimension on the source region) the radiation is similar to that of a point source with no angular dependence.

Submarines and torpedoes with centerline propellers have a relatively symmetric inflow condition. Surface ship propellers, in contrast, operate under nonuniform inflow conditions. Circumferential wake variation causes the radiated sound to be amplitude modulated at the blade rate frequency. Furthermore, slight physical difference between the blades produces modulation at the shaft rate frequency. These amplitude variations gives a very distinct characteristic to the radiated noise that can be used for classification purposes to reduce the probability of false alarm.

The most complete source of data on surface ship radiated noise are measurements made during WWII, reported

in a compendium issued by the U.S. Office of Scientific Research and Development (OSRD) in 1945 and declassified in 1960. When these data are examined the radiated noise is found to depend on tip speed and the number of propeller blades with little dependence on the other variables. For surface ships near cruise speed, the source level for frequency over 100 Hz can be written as:

$$SL = SL' + 20 - 20\log f; \quad f > 100 \text{ Hz} \tag{7}$$

where

f = frequency in Hz

SL' = overall source level in dB re 1μPa.

The overall level can be expressed as:

$$SL' = 175 + 60\log U/25 + 10\log b/4 \tag{8}$$

where

$$U = \pi n D \tag{9}$$

n = rotational speed (rpm)

D = diameter of the propeller (m).

The above expressions are used as the basis for the noise model with the following input data:

n = 300 rpm for maximum cruise speed of 15 kts.

n = 180 rpm for a cruise speed of 10 kts.

D = 2 m.

b = 5.

The resulting noise spectrum, in dB re 1μPa at 1 m, as a function of speed in kts. are tabulated in Table II.

TABLE II

SOURCE LEVEL DATA AND CALCULATION
FOR A BLADE SURFACE CAVITATING PROPELLER

Rotational Frequency n rpm	Rotational Frequency n s^{-1}	Diameter of Propeller D m	Tip Speed U_t m/s	Advance Speed U m/s	Overall Level SL' dB re 1μPa	Average Source Level SL dB re 1μPa
300	5	2	31.4	15	182	106.0
180	3	2	18.9	10	168.6	93.0

and plotted in Fig. 15. A one sigma region (5 dB of uncertainty) is incorporated in Fig. 15.

The above noise spectrum estimation agrees very well in the high frequency limit, with more recent studies by A. Lövik [Refs. 11 and 12]. Here it is found that the cavitation spectra, both theoretically and experimentally, can be divided into four frequency regions, as illustrated in Fig. 16.

Region I is dominated by noise at the blade frequency and its harmonics. The emitted sound is caused by the volume variation of the main cavity.

Region II starts at the bubble frequency, which is the reciprocal of the lifetime of the main cavity. The mean power level is found to decrease with increasing frequency as $f^{-2.5}$.

Region III is an intermediate region.

Region IV associated with the shock waves starts at the mean collapse frequency f_c, given by the mean collapse time. The power level is found to decrease as f^{-2}, as in Eq. 5.

The number of gas bubbles in the water have a pronounced effect on the high frequency cavitation noise from the propeller. This is illustrated in Fig. 17, obtained from Ref. 12, where the power is found to decrease as much as 40 dB with increasing gas content.

Scaling laws are developed [Ref. 12] for each region based on a series of models and full scale measurements. These laws depend on the dynamic pressure induced by the propeller, the model ratio, and the gas content of the water. The full scale measurements were performed in cooperation with the Royal Norwegian Navy and the Marine Institute of Norway. The model experiments were performed in the largest cavitation tunnel at the Ship Research Institute of Norway.

In summary, the scaling of cavitation noise was demonstrated to be a useful tool in predicting a full scale cavitation noise as shown in Fig. 18 [Ref. 12] which compares measured noise spectra for the model and full scale measurements.

For the high frequency region, the source levels are of the same magnitude as predicted by the WWII empirical formula.

D. PASSIVE MODE RECEIVER CHARACTERISTICS

1. Assumptions

For receiver characteristics assume a square law detector with a center frequency f-60 or 30 kHz and a bandwidth B. The detection scheme is shown in Fig. 16. The principal assumptions employed in the derivation are as follows:

-Gaussian signals in Gaussian noise

-Frequency independent signal and noise spectra

-Integration time T is sufficiently long to permit application of the central limit theorem.

2. Derivations

The detector input r(t) is assumed to be a zero-mean Gaussian process composed of noise alone or signal plus noise expressed by the two well known hypotheses

$$H_o\ r(t) = n(t) \tag{10}$$

$$H_1\ r(t) = s(t)+n(t)$$

where:

n(t): noise signal

s(t): signal.

The two signals s(t) and n(t) are assumed to be independent.

Assume that the spectral shape of s(t) and n(t) are the same, such that H_o and H_1 only differ in the total power level. Then the detector-smoother have the form:

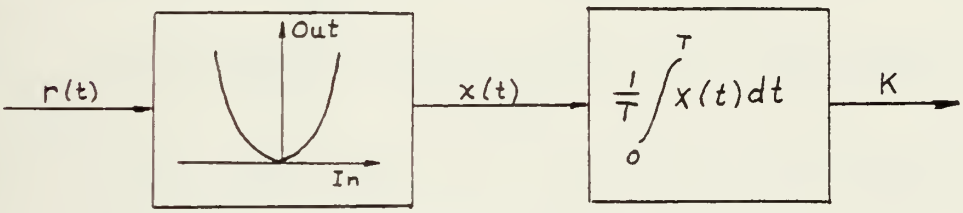

Schematic of detector-smoother

and

$$x(t) = r^2(t) \tag{11}$$

Furthermore, let the noise variance be normalized to unity (for convenience) and the signal variance by denoted by σ^2

$$Var[n(t)]=1 \tag{12}$$

$$Var[s(t)]=\sigma^2$$

Because of the assumed similarity in the spectral shapes, the autocorrelation functions are

$R_n(\tau)=F^{-1}[N(f)]=\rho(\tau)$; $N(f)$ is the noise power spectral density. (13)

$R_s(\tau)=\rho(\tau)\sigma^2$

$$R_n(\tau)= \begin{array}{ll} H_o & \rho(\tau) \\ H_1 & (1+\sigma^2)\rho(\tau) \end{array}$$

Furthermore, assume that the integration time T is long enough so the central limit theorem holds, implying that K also is a Gaussian random variable.

This yields that the probability density function of the output variable and hence the detection and false alarm probabilities are completely determined once the mean and the variance of K are derived.

If a process V(t) is wide-sense stationary, then

$$E[V(t)]=E\frac{1}{T}\int_0^T V(t)dt = \frac{1}{T}\int_0^T E[V(t)]= \nu \text{ (constant)} \tag{14}$$

Thus, assuming that r(t) is a wide-sense stationary process.

$$E[K]=E[x(t)]=E[r(t)]=1+\sigma^2 \tag{15}$$

and similarly

$$Var[V]=E[V^2]-\{E[V]\}^2= \frac{1}{T^2}\int_0^T\int_0^T E[V(t)V(s)]dtds-\nu^2 \tag{16}$$

$$Var[V]=\frac{1}{T^2}\int_0^T\int_0^T [R_V(t-s)-\nu^2]dtds=\frac{1}{T^2}\int_0^T\int_0^T Cov_V(t-s)dtds$$

where $Cov_v(t-s)$ is a covariance function.

Then letting

$$\tau = t-s$$

$\zeta = t+s$, and substituting into Eq. (7) yields

$$Var[V]=\frac{1}{T^2}\iint_{\Diamond} Cov_v(\tau)\frac{d\zeta d\tau}{2}$$

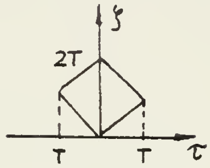

$$Var[V]=\frac{1}{T}\int_{-T}^{T}[1-\frac{|\tau|}{T}]Cov_v(\tau)d\tau \tag{17}$$

Consequently

$$Var[K]=\frac{1}{T}\int_{-T}^{T}[1-\frac{|\tau|}{T}]Cov_v(\tau)d\tau \tag{18}$$

Then, evaluating the covariance function from the auto-correlation function

$$R_x(\tau)=E[x(t)x(t-\tau)] = E[r^2(t)r^2(t-\tau)] \tag{19}$$

Since $r(t)$ is Gaussian, the above fourth moment can be expressed as product and sums of second moments:

$$R_x(\tau)=\overline{r^2(t)}\cdot\overline{r^2(t+\tau)} + 2\overline{r(t)r(t-\tau)}\cdot\overline{r(t)r(t-\tau)}$$

$$=R_r^2(0) + 2R_r^2(\tau)$$

$$R_x(\tau)=(1+\sigma^2)^2+2(1+\sigma^2)^2 \rho^2(\tau) \tag{20}$$

Thus, the covariance function is

$$Cov_x(\tau)=R_x(\tau)-\{E[x(t)]\}^2$$

$$=(1+\sigma^2)^2+2(1+\sigma^2)\rho^2(\tau)-(1+\sigma^2)^2$$

$$Cov_x(\tau)=2(1+\sigma^2)^2\rho^2(\tau) \tag{21}$$

Inserting Eq. (12) into Eq. (9) yields

$$Var[K]=\frac{1}{T}\int_{-T}^{T}\{[1-\frac{|\tau|}{T}]\ 2(1+\sigma^2)^2\rho^2(\tau)\}\ d\tau$$

$$Var[K]=\frac{2(1+\sigma^2)^2}{T}\int_{-T}^{T}[1-\frac{|\tau|}{T}]\ \rho^2(\tau)d\tau \tag{22}$$

If T is large compared to the correlation time

$$TB>>1$$

then we can substitute the limit for Eq. (22) by

$$Var[K]=\frac{2(1+\sigma^2)^2}{T}\int_{-\infty}^{\infty}\rho^2(\tau)d\tau \tag{23}$$

$$=\frac{2(1+\sigma^2)^2}{T}\int_{-\infty}^{\infty}N^2(f)df$$

If we further make the assumption that the signal and noise have ideal flat bandpass spectra:

$$N(f)=\begin{cases}1/2B, & f-B/2<f<f+b/2\\ 0, & \text{otherwise,}\end{cases} \tag{24}$$

Inserting Eq. (24) in Eq. (23) yields

$$Var[K]=\frac{(1+\sigma^2)^2}{BT} \tag{25}$$

The probability density function for the output of the detector have the following form

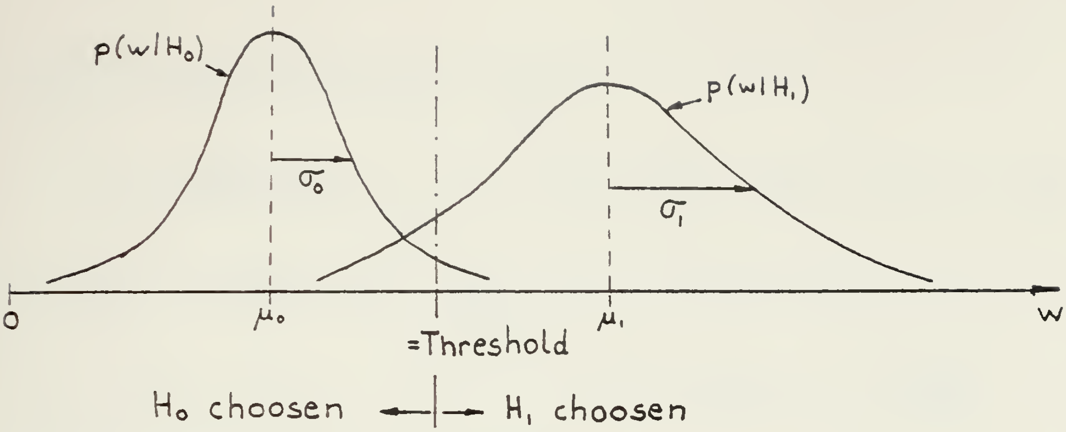

Here w is the outcome of all possible signals. The false alarm probability is obtained by integrating the conditional probability $p(w|H_o)$ over the outcome space for which to choose H_1.

$$P_{FA} = \int_j^{\infty} p(w|H_o)\,dw = Q(\frac{j-\mu_o}{\sigma_o}) \qquad (26)$$

Similarity, the miss probability=1-detection probability is obtained by integrating the conditional probability $p(w|H_1)$ over the outcome space for which to choose H_o.

$$P_M = 1-P_D = \int_{-\infty}^{j} p(w|H_1)\,dw = Q(\frac{\mu_1-j}{\sigma_1}) \qquad (27)$$

Further defining the input and output signal-to-noise ratios as

$$S/N(\text{input}) = \frac{\sigma^2}{1} = \sigma^2 \qquad (28)$$

$$S/N(\text{output}) = \frac{(\mu_1-\mu_0)^2}{\sigma_1{}^2} \qquad (29)$$

For the square law detector where

$$\mu_o = E[n^2(t)] = 1, \quad \mu_1 = E[r^2(t)] = E[K] = 1+\sigma^2 \tag{30}$$

$$\sigma_0{}^2 = Var[n^2(t)] = \frac{1}{BT}, \quad \sigma_1{}^2 = Var[r^2(t)]$$

$$= Var[K] = \frac{(1+\sigma^2)^2}{BT}$$

The output signal-to-noise ratio:

$$S/N(output) = \frac{(1+\sigma^2-1)^2}{\left[\frac{(1+\sigma^2)^2}{BT}\right]} = \frac{BT\ \sigma^4}{(1+\sigma^2)^2} \tag{31}$$

The input signal-to-noise ratio:

$$S/N(input) = \sigma^2 \tag{32}$$

The probability of false alarm:

$$p_{FA} = Q[\sqrt{BT}(j-1)] \tag{33}$$

The probability of detection:

$$p_D = 1-Q\left[\sqrt{BT}\ \left(\frac{1+\sigma^2-j}{1+\sigma^2}\right)\right] \tag{34}$$

The Equations (32), (33), and (34) are plotted for a variety of realistically encountered conditions. Figure 17 gives BT versus S/N(in) (identical to the detection threshold DT) for various combinations of p_D and p_{FA}.

Figure 18 gives p_D versus S/N(in) for various combinations of the threshold j and p_{FA}. This constitutes the ROC-curves for the generalized square law detector.

E. REFERENCE DETECTION PERFORMANCE

1. Introduction

As both the scattering and absorption are frequency dependent, it is necessary to have reference models for both 60 and 30 kHz.

2. 60 kHz Case

The range dependent portion of the sonar Equation (1):

$-20\log r - \alpha R$

is plotted in Fig. 19 for $\alpha=0.021$ dB/m taken from Fig. 14.

Figures 15, 17 and 19 are then used to estimate the detection range:

(a) Select p_D, p_{FA}, B, and the integration time T. The detection threshold DT=S/N(input) is then found from Fig. 17.

(b) Select the speed of the target and find the SL from the noise source model (Fig. 15). Then, reasonable values for the receiver sensitivity DI and the self noise level NL yields the left hand side of the sonar equation (1) except for range dependent term.

(c) Use Fig. 19 to solve the passive equation for R.

A realistic example may illustrate the above procedure.

(a) Entering Fig. 17 with

$p_D = 0.5$

$p_{FA} = 10^{-6}$

$B = 4500$ Hz

$T = 100$ msec

yields

DT = -6.5 dB.

(b) Selecting a target speed of 12 kts. gives (from Fig. 15) SL=100 dB. Selecting a typical transducer sensitivity DI = -180 dB. Assuming the NL to be dominated by self noise of typical value NL=-124 dB. This yields

$$SL+10\log B+DI-NL-DT=87 \text{ dB.}$$

(c) Figure 19 with

$$-20\log R-0.02R=-87$$

yields

R=1200 m. for a=0.02 dB/m and f-50 kHz.

The influence of different design parameters like self noise and detection threshold on the passive detection performance is now easily investigated by the above procedure.

Although outside the main scope of this analysis, the above statement can be confirmed with an example. As seen from Fig. 18, a probability of false alarm $p_{FA} = 10^{-6}$ implies a threshold setting = 0.9 dB above the noise level.

Due to the variability of the noise level together with the practical difficulty in accurately setting the threshold, a more realistic goal for the threshold would typically be 3 dB. Going into Fig. 17 shows that the corresponding value for DT for $p_D = 0.5$ is DT = 0 dB, with a corresponding low value for the p_{FA}.

Letting DT=0 dB and keeping the previous assumed values of SL, DI, and NL yields:

$$SL+10\log B+DI-NL-DT=80.5 \text{ dB}.$$

The corresponding detection range is:

R = 1000 m, for $\alpha = 0.02$ dB/m and f = 60 kHz.

Thus, this change in threshold setting caused a decrease in detection range from 1200 m to 1000 m in return of a significant decrease in the false alarm probability.

3. 30 kHz Case

In order to estimate the reference detection range for an operating frequency of 30 kHz, we utilize the sonar equation (1).

Assume that the receiver has the same generalized passive detector characteristics as in the 60 kHz case:

DI = -180 dB

NL = -124 dB.

DT = -6.5 dB, based on $p_D = 0.5$ and $p_{FA} = 10^{-6}$.

However, the empirical equation (7) for the source level:

$$SL=SL'+20-20\log f$$

shows that the source level falls off as f^{-2}. If the dynamical and dimensional parameters of the propeller are the same, SL will increase by +6 dB when the frequency is reduced from 60 to 30 kHz.

A source level of

$$SL=100+5=106 \text{ dB}$$

gives a range dependent solution of the sonar equation

$$-20\log R - \alpha R=-87-6 = -93 \text{ dB}.$$

A plot of

$$-20\log R-\alpha R$$

is given in Fig. 20 for an absorption coefficient $\alpha=0.01$ dB/m taken from Fig. 14.

Figure 20 then gives a detection range of

$$R = 2400 \text{ m}.$$

Thus, as seen from these ideal reference calculations, halving the frequency gives a higher source level and a lower absorption loss, resulting in a doubling of the detection range.

VI. THE EFFECT OF SURFACE SCATTERING

A. OCEANOGRAPHIC DESCRIPTION OF THE SEA SURFACE

The roughness of the sea surface is the essence of the scattering mechanism. Thus, to adequately describe the scattering of sound from a randomly rough sea surface, it is necessary to formulate a suitable description of the sea surface from an acoustical propagation point of view.

Generally the shape of the rough sea surface is most appropriately described in terms of time and spatial dependent random variables. However, observation of the ocean under the same environmental (meteorological) conditions indicates that the roughness is the same over large areas and for periods of at least several hours. The random processes responsible for the structure of the sea surface, therefore, can be considered stationary at least over periods of hours. With this assumption, the sea surface can be described in terms of the statistical description of the surface displacement function, and the distribution of signals reflected from the sea surface can then be related to this probability distribution function.

The most significant statistical parameters describing the scattering mechanism from the randomly rough surface are:

-the mean square slope

-the mean square surface height

-the correlation length.

Optical measurements made at sea by C. Cox and W. Munk [Ref. 13] showed that the sea surface with an arbitrary wide continuous spectrum of waves is characterized by a Gaussian distributed surface slope. The mean square slope, determined from these optical measurements is

$$<\zeta'^2> = \Sigma^2 = (3+5.12w)x10^{-3} \qquad (35)$$

where

W=wind speed in m/s measured 41 ft (12.5 m) above the sea surface.

The Gaussian distribution of surface slopes implies that the surface displacement function can be described by a Gaussian probability density function with zero mean

$$<\zeta> = 0$$

and variance

$$<\zeta> = \sigma^2$$

and Gaussian correlation function

$$<\zeta(t)\zeta(t+\tau)>$$

The mean square height σ^2, is obtained by integrating the frequency spectrum of the fully developed sea. The frequency spectrum G is given by the commonly accepted semi-empirical expression of Piersom-Moskowitz [Ref. 14] as

$$G(\Omega) = \frac{\alpha g^2}{\Omega^5} \exp[-\beta \frac{\Omega_o}{\Omega}]^4 \tag{36}$$

where

Ω = frequency (in s^{-1})

$\alpha = 8.1$

$\beta = .74$

$\Omega_o = g/W$ (in s^{-1}).

W = wind speed in m/s at 19.5m above the sea surface

g = gravitational acceleration (in m/s^2).

This gives

$$\sigma^2 = \int_0^\infty G(\Omega)\,d\Omega = \frac{\alpha W^4}{4\beta g^2} \tag{37}$$

For a Gaussian autocorrelation function expressed as

$$\psi(\tau) = \frac{1}{\sigma^2} <\zeta(t)\zeta(t+\tau)>= e^{-\tau^2/r^2} \tag{38}$$

where

T = correlation length.

The following relationship for the mean square height holds for sea of small roughness

$$\Sigma^2 = \frac{2\sigma^2}{T^2} \text{, see later Eq. (60)} \tag{39}$$

and the correlation length is thus:

$$T = \sqrt{2}\,\frac{\sigma}{\Sigma} \tag{40}$$

B. SCATTERING THEORY

All real boundaries are rough for radiation with short enough wavelength, and the apparent roughness depends on the "viewing" conditions. The wave reflected by a plane surface has the same properties as the incident wave since the radiation is scattered coherently and there is a definite relation between the incident and scattered waves.

A randomly rough surface, however, such as the wind generated ocean surface, scatters radiation in all directions, i.e., an illuminated area is visible from any direction.

Heuristically there are two distinct approaches to this phenomena.

1. If the boundary is rough most of the radiation is scattered and there is little transmission in the specular direction. Thus, the attenuation caused by the irregularities can be included in the transmission equation.
2. If the surface is truly smooth, it can be assumed that the effect of the boundary is to supplement the original pressure field by an out-of-phase image contribution. For a randomly rough surface the reflected sound neither completely cancels the direct sound nor adds to give +6 dB pressure peaks of the interference pattern. For a rough surface, this supplement is a small fraction of the direct path.

The second approach will be used with the simplified assumption that the sea below the surface has an isotropic statistical description; i.e., the mean acoustic velocity and the mean density are assumed to be constant and have negligibly small mean square fluctuations.

The estimation of the scattering is based on an approximation method employing both ray and wave theory. Ray methods are used to follow the acoustic signal from the noise source to the vicinity of the sea surface. Then, wave theory is used to calculate the scattering process. Finally, ray theory is used to follow the scattered signal to the receiver.

The geometry is given in Fig. 24a. The origin of the coordinate system is at the center of the illuminated area. The x-y plane coincides with the mean of the rough surface as averaged over the illuminated area.

The source and receiver are at distances R_1 and R_2, respectively, from the origin. R_1 is the xz-plane and makes the angle θ_1 with the z-axis. R_2 makes the angle θ_2 with the z-axis and the projection of R_2 on the xy-plane has an angle θ_3 relative to the x-axis.

For high frequencies R_1 and R_2 are much larger than the acoustic wavelength. Then both the incident wave and scattered waves can be treated as nearly plane waves.

The formulation of the scattering problem will be based on the Helmholtz integral which requires known values of the normal derivatives of the incident and reflected waves on the boundary. These are estimated by using the neuristic Kirchhoff's approximation, which assumes that the wave is locally reflected by a plane surface; i.e., an approximation restricted to a surface not too rough and not shadowed.

Further, the receiver derictivity, as indicated by Fig. 24b, will be used to limit the surface area that is illuminated.

Since this procedure is based on a detailed development by I. Tolstoy and C. S. Clay [Ref. 15], only the main points will be outlined here to bring out the assumptions made and the inherent limitations of this approach.

The development starts by considering the inhomogeneous wave equation of the general form:

$$\nabla^2 p(\vec{x}_1 t) - \frac{1}{c^2} \frac{\partial^2 p(\vec{x}_1 t)}{\partial t^2} = -4\pi \; f(\vec{x}_1 t) \qquad (41)$$

where

$f(\vec{x}_1 t)$ = is a known source distribution.

The development is based on the following initial assumptions:

-The medium is homogeneous.

-The medium is bounded by some surface S, onto which an incident wave impinges.

-The boundary is characterized by the specific acoustic admittance and the shape of the boundary.

-The incident wave is harmonic.

The assumed harmonic source implies that $f(\vec{x},t)$ can be decomposed into a Fourier integral. Furthermore, assuming that the solution of Eq. (41) can be decomposed in time, we arrive at the Helmholtz equation

$$\nabla^2 p_\omega(x) + \frac{\omega^2}{c^2} p_\omega(x) = -4\pi f_\omega(x) \tag{42}$$

It should be noted here that L. Fortuin, in [Ref. 16] showed that the Helmholtz equation is not exactly correct for a medium with a time dependent boundary. The equation can, however, be used with a good approximation when the time derivative of the surface elevation is much smaller than the speed of the waves through the medium. For underwater sound waves scattered by the rough sea surface, this means that the wind speed has to be much less than the sound speed; a requirement easily fulfilled for our investigation.

Green's method allows the solution of this linear inhomogeneous wave equation to be expressed in the heuristic Helmholtz integral form:

$$p_\omega(x) = \int_V f_\omega(x^1) G_\omega(xx^1) d^3x^1 + \frac{1}{4\pi}\oint_S \{G(xx^1)\frac{\partial p_\omega(x^1)}{\partial n^1} - p_\omega(x^1)\frac{\partial G_\omega(xx^1)}{\partial n^1}\} da^1 \tag{43}$$

The first integral on the RHS of Eq. (43) contains the sound sources and the bulk (volume) scattering. The second integral represents the surface scattering and is taken over all finite surfaces.

Now, disregarding the direct path, the signal at the receiver is given by the surface integral alone:

$$p_{\omega}^{(s)}(x_2)=\frac{1}{4\pi}\int_{s}\left\{G(x_2x^1)\ \frac{\partial p_{\omega}}{\partial n^1}-p_{\omega}(x^1)\frac{\partial G}{\partial n^1}\right\}da^1 \qquad (44)$$

where the subscript s denotes the scattered field. In order to solve Eq. (44) the following must be done:

- Give an approximate expression for the incident wave.
- Find an appropriate Greens function.
- Make an approximation for $p_{\omega}(x^1)$ and $\partial p_{\omega}/\partial n$ at the surface.

As we already have assumed a simple harmonic source, the incident wave can be expressed as:

$$p_{\omega}^{(i)}(x^1)=\left(\frac{\Pi\rho c}{2\pi}\right)^{\frac{1}{2}}\frac{D}{R}\,e^{ikR}\equiv\frac{BD}{R}\,e^{ikR} \qquad (45)$$

where

Π: power output.

D: illumination function.

Assuming kR>>1, i.e., that the distance of the source is large compared to the wavelength, the wave in the bounded ensonified area can be considered as a plane wave

characterized by its propagation vector

$$k_i = -k\frac{\vec{x}_i}{|\vec{x}_1|}$$

thus obtaining the expression for the incident wave:

$$P_\omega^{(i)}(\vec{x}_1) = \frac{BD}{R} e^{ikR_1} e^{i\vec{k}i \cdot \vec{x}^1} \tag{46}$$

Further assuming that the receiver is sufficiently far removed from the scattering area with the rest of the sea surface not contributing, then the scattering area acts as a small induced source in a free space and we can approximate the propagation of the scattered waves from the ensonified region in terms of the free field Greens function:

$$G(x_2x_1) \approx \frac{e^{ikR_2}}{R_2} e^{-i\vec{k}_s \cdot \vec{x}^1} \tag{47}$$

where

$$k_s = k\frac{\bar{x}_2}{|\bar{x}_2|}$$

We further assume that each surface element da^1 acts as a small reflector, and that the response of da^1 to the incident wave is that of a "local reaction," i.e., independent of any other part of the ensonified area A.

Then, the Kirchhoff's approximation where it is assumed that p and ∂p/∂n vanish everywhere on the surface except at the ensonified area and that the values of p and ∂p/∂n are proportional to the incident wave, allow the scattered

"target" strength for the ensonified area to be approximated as:

$$p_\omega(x^1)\Big|_A = R\, p_\omega^{(i)}(x^1) \quad (48)$$

$$\frac{\partial p}{\partial n^1}\Big|_A = R\frac{\partial p^{(i)}}{\partial n^1}$$

where

p is the locally reflected wave.

R = reflection coefficient.

$$= \frac{p^1c^1\cos\theta - pc\cos\theta^1}{p^1c^1\cos\theta + pc\cos\theta^1};\quad \frac{c}{\sin\theta} = \frac{c^1}{\sin\theta^1}$$

Finally, assuming a Gaussian illumination function:

$$D = e^{-\frac{x^2}{X^2} - \frac{y^2}{Y^2}} \quad (49)$$

where

X and Y are the effective dimensions of the illuminated area.

The scattering integral based on the Kirchhoff's approximation can be expressed as:

$$p_\omega^{(s)}(x_2) = -\frac{ikBe^{ik(R_1+R_2)}}{2\pi R_1R_2} Rf(\theta_1\theta_2\theta_3) \iint_{-\infty}^{\infty} De^{2i(\alpha x^1+\beta y^1)} e^{2i\zeta(x^1y^1)}\, dx^1dy^1 \quad (50)$$

where

$\alpha = \frac{k}{2}(\sin\theta_1 - \sin\theta_2\cos\theta_3)$

$\beta = -\frac{k}{2}\sin\theta_2\sin\theta_3$

$\gamma = -\frac{k}{2}(\cos\theta_1 + \cos\theta_2)$

$\zeta(x^1 y^1)$ = surface displacement function.

The above scattering integral is then applied to a randomly rough surface where the surface displacement function ζ is a random variable assumed to be represented by a Gaussian PDF expressed as

$$W(\zeta) = \frac{1}{\sigma\sqrt{2\pi}} e^{-\zeta^2/2\sigma^2} \tag{51}$$

with zero mean and variance σ^2.

Also, assume that the surface is slowly varying so that the signal reflects from an essentially stationary surface and that the succession of received scattered signals p_n are assumed to form a satistically independent set of sample functions from which sequence N the first and second moment of the field can be investigated. Doing so Clay and Tolstoy [Ref. 15] found that the mean reflected signal can be expressed as

$$\langle p_\omega^{(s)}(x_2)\rangle_\zeta = P_o e^{-2\gamma^2\sigma^2} \tag{52}$$

where

$$P_o = p_\omega^{(s)}(x_2)\big|_{\zeta=0}$$

is the signal reflected by a mirror-like surface, other factors being the same.

It is seen from the above that

1. For $\sigma \to 0$, all displacements ζ have zero probability and the mean signal tends to p_o. Furthermore, all elements contribute to the scattering coherently.

2. For $\sigma >> k$, all displacements ζ are equally probable. There are large phase shifts between contributions from different surface elements and they tend to cancel each other and the scattering radiation is incoherent.

The second moment is defined as:

$$<s^2(t) \triangleq \frac{1}{T} \int_0^T s^2(t)dt = <pp^*>_T - <\bar{p}\bar{p}^*>_T \qquad (53)$$

where

$$s^2(t) = \frac{1}{N}[\sum_1^N p_n{}^2(t) - N<p(t)>_N^2] \qquad (54)$$

In this expression the operation of squaring the signal has to be considered. However, each surface element has a different ζ for a random surface. Thus, the probability of finding element dx' dy' with ζ_1, and element ζ_2 with dx" dy" is expressed in the bivariate distribution function assumed to be Gaussian and of the form:

$$W(\zeta_1\zeta_2) = \frac{1}{2\pi\sigma^2(1-\psi^2)^{\frac{1}{2}}} e[-\frac{1}{2(1-\psi^2)\sigma^2}(\zeta_1{}^2+\zeta_1{}^2-2\zeta_1\zeta_2\psi)] \qquad (55)$$

where

$$\psi(\xi,\eta) = \frac{1}{\sigma^2} <\zeta_1(x^1y^1t)\ \zeta_2(x''y''t)> \qquad (56)$$

is the cross-correlation function characterizing the surface shape.

Changing to polar coordinate leads to Eq. 6.51 of Ref. 15 where:

$$<s^2> \alpha \int_0^\infty D\, J_o(2\kappa r)\,[e^{-4\gamma^2\sigma^2(1-\psi)} - e^{-4\gamma^2\sigma^2}]\; rdr \qquad (57)$$

Here J_o is the Bessel function of zero order and x is the transformation parameter given as

$$\kappa = \frac{\alpha}{\cos\,\theta}$$

As seen from Eq. (57)

1. For rough surface, $\gamma^2\sigma^2$ is large and the second term in the bracket, the coherent part, is negligible.
2. For smooth surface, $\gamma^2\sigma^2$ is zero and the whole bracket is zero.

Since Eq. (57) cannot be integrated directly, Clay and Tolstoy [Ref. 15] consider it for small and large $\gamma\sigma$ separately.

Thus, concentrating on the high frequency limit, Clay and Tolstoy assumed $\gamma^2\sigma^2 >> 1$ and showed that:

-The coherent component is negligible.

-$<s^2> \cong <pp^*>$, as the means tends to zero,

$$<s^2> \cong <pp^*> \alpha \int_0^\infty J_o(2\kappa r)\, e^{-4\gamma^2\sigma^2(1-\psi)}\, rdr;\; \gamma^2\sigma^2 >> 1 \qquad (58)$$

Equation (58) consists of the product of an oscillatory function and an exponential function. Because of the Bessel function, the main contribution to the integral is near r=0. Near r=0 the phase changes slowly and the expression can be evaluated by the method of stationary phase. Thus, the expression of ψ about r=0 is given as:

$$\psi \simeq 1+\psi''(0)\frac{r^2}{2} \tag{59}$$

Furthermore, Clay and Tolstoy show that $\psi''(0)$ can be related to the characteristics of the surface as:

$$|\psi''(0)| = \frac{1}{\sigma^2} <\zeta'^2> \tag{60}$$

Finally, Clay and Tolstoy show that the scattering signal can be expressed as:

$$<s^2> = <pp^*> = <P_1P_1^*> \frac{A}{R_2{}^2} S_{hf}; \quad \begin{matrix} 4\gamma^2\sigma^2>>1 \\ (2\gamma^2<\zeta'^2>)>>\frac{1}{R^2} \end{matrix} \tag{61}$$

where

A = ensonified area

$<p_1p_1^*>$: the expected average value of $p_1{}^2$, where p_1 is the incoming pressure to the luminated area.

S_{hf} = scattering function

$$= \frac{f^2(\theta)R^2}{2\pi(\cos\theta_1 + \cos\theta_2)^2<\zeta'^2>} e^{-\frac{x^2}{(2\gamma^2<\zeta'^2>)}}$$

$$f(\theta) = f(\theta_1\theta_2\theta_3) = \frac{1+\cos\theta_1\cos\theta_2-\sin\theta_1\sin\theta_2\cos\theta_3}{\cos\theta_1+\cos\theta_2}$$

$$R = \frac{\rho^1 c^1\cos\theta - \rho c \cos\theta^1}{\rho^1 c^1\cos\theta + \rho c \cos\theta^1}; \quad \frac{c}{\sin\theta} = \frac{c^1}{\sin\theta^1}$$

$$\gamma = -\frac{k}{2}(\cos\theta_1 + \cos\theta_2)$$

$$\kappa = \frac{\alpha}{\cos\theta}$$

$$\alpha = \frac{k}{2}(\sin\theta_1 - \sin\theta_2\cos\theta_3)$$

$$k = \frac{2\pi}{\lambda}$$

$<\zeta^{12}> = (3 + 5.12W) \times 10^{-3}$; W = wind speed in m/s.

Equation (61) is valid for:

$$4\gamma^2\sigma^2 >> 1$$

$$(2\gamma^2<\zeta^{12}>) >> \frac{1}{R^2}$$

In summary, the reflection of high frequency signals yields scattered radiation which is incoherent. Furthermore, as pointed out by Clay and Tolstoy in [Ref. 15] although the radiation is primarily scattered in the specular direction, parts are scattered in all directions. As seen from Eq. (61) the scattering function S_{hf} is primarily dependent on the mean square slope of the surface $<\zeta^{12}>$ and neither the mean square wave height σ^2 nor the correlation distance are important. Furthermore, it is noticeable that in the

high frequency limit the scattering function is independent of the frequency since

$$e - \frac{k^2}{(2\gamma^2 \langle \zeta'^2 \rangle)} \to 1 \text{ when } r^2 \to \infty$$

C. GEOMETRICAL SHADOWING

The phenomena of shadowing of some surface areas by others has to be considered either when the surface irregularities are large with respect to the incident wavelength or when the grazing angle is small.

The few papers devoted to this subject are aimed mainly towards calculation of a "Shadowing function" based on the statistics of the surface.

An explicit method, geometrical shadowing, has been introduced by P. Bechmann [Ref. 17] where the shadowing function $S(\theta)$ is the probability that the point ζ (Fig. 25) is illuminated.

$$S(\theta) = \exp\left[-\int_0^\infty q(x)\,dx\right] \tag{62}$$

where:

$q(x)$ is the probability that ζ is shaded by ζ in the interval $(x, x+dx)$ given that it is not shaded in $(0,x)$.

This calculation of $S(\theta)$ only considers the elevation of the surface observation point. However, the slope also plays a role in that if its value exceeds $\cot\theta$ the point

will certainly be shaded. Thus, R. Wagner, in Ref. 18, incorporated both ζ and ζ^1 using P. Bechmann's method and found that the conditional probability that a point on the surface is illuminated, given that it has height ζ and slope ζ^1, can be expressed as:

$$S(\theta_1|\zeta_1,\zeta_1{}^1) = \exp[-\int_0^\infty q(x)dx] \quad u(\cot\theta - \zeta^1) \qquad (63)$$

where

u: is the unit step function.

q(x): is the conditional probability that ζ is shadowed in the interval (x,x+dx) given that it is not shadowed in (0,x).

The function q(x) cannot be calculated exactly. Thus, R. Wagner made the approximation that, for all x, the probability that ζ crosses the ray in dx is independent of the values of ζ and ζ^1 at x=0. In the above, no mention has been made of the direction of observation. However, in this respect, R. Wagner [Ref. 18] points out that in the high frequency limit only those portions of the surface which are illuminated simultaneously by rays in the direction of incidence and observation can contribute to the observed scattered power. For this condition, R. Wagner introduced both directions as independent variables in the so-called bistatic shadowing probabilities where he defines:

1. $S(\theta_1\theta_2|\zeta_1,\zeta_1')$ to be the conditional probability that the surface will not cross the incoming ray (Ray 1) or the outgoing ray (Ray 2) anywhere, given that both rays pass through an arbitrary point or the surface with displacement ζ and slope ζ^1.
2. $S(\theta_1|\theta_2,\zeta_1,\zeta_1')$ to be the conditional probability that the surface does not cross Ray 1, given that it does not cross Ray 2 and that both rays pass through the point ζ having slope ζ'.

Thus, the conditional shadowing function can be expressed as:

$$S(\theta_1,\theta_2|\zeta_1,\zeta_1') = S(\theta_1|\theta_2,\zeta_1,\zeta_1')\ S(\theta_2|\zeta_1,\zeta_1') \quad (64)$$

The shadowing function is then obtained by averaging over all possible heights and slopes

$$S(\theta_1,\theta_2) = \iint_0^\infty S(\theta_1,\theta_2|\zeta,\zeta')\ W(\zeta,\zeta')d\zeta\ d\zeta' \quad (65)$$

Here $w(\zeta,\zeta')$ is the bivariate PDF of the surface height and slope, assumed to be Gaussian

$$w(\zeta,\zeta') = \frac{1}{2\pi}\ (\psi_0|\psi_0''|)^{-\frac{1}{2}}\ \exp\{-\frac{\zeta^2}{2\psi} - \frac{\zeta^1}{2|\psi_0''|}\} \quad (66)$$

where $\psi_0 = \sigma^2$ and ψ'' are the values at $\tau=0$ of the correlation function and its second derivatives, respectively.

For the region $0<\theta<\frac{\pi}{2}$ where the probability of crossing one ray is assumed independent of that of crossing the other, R. Wagner found that the bistatic shadowing function

could be expressed as:

$$S(\theta_1,\theta_2) = \frac{\{1-\exp[-2(B_1+B_2)]\}x\{\text{erf } v_1+\text{erf } v_2\}}{4(B_1+B_2)} \qquad (67)$$

where

$$B_i = \frac{\exp(-v_i^2)-\sqrt{\pi}\ v_i \text{ erfc } v_i}{4\pi\ v_i} \ ; \quad i = 1,2$$

$$v_i = \frac{\eta_i}{2\sigma^2|\psi_o''|} = \frac{|\eta_i|}{2\Sigma^2} \ ; \ i = 1,2$$

as we from Eq. (60) have that $\sigma^2|\psi''(0)|$ $= \langle\zeta'^2\rangle = \Sigma^2$

$$\eta_i = \cot\theta;\ i = 1,2$$

and noting that

$$\text{Error function erf}(x) = \frac{2}{\sqrt{\pi}} \int_0^x e^{-t^2}\,dt$$

$$\text{Complementary error function erfc}(x) = \frac{2}{\pi} \int_x^\infty e^{-t^2}\,dt$$

The shadowing function $S(\theta_1,\theta_2)$ is, in short, the fraction of the surface still illuminated. As seen from Eq. (60), the scattered field, in the high frequency case, is proportional to the illuminated area. Hence, the shadowing effect of a rough surface can be introduced by multiplying the ensonified area A by the shadowing function $S(\theta_1,\theta_2)$.

D. ESTIMATING THE SURFACE SCATTERING EFFECT

The following estimations are based on calculations in the specular direction, which is, as pointed out earlier, expected to give the maximum supplementary scattering effect. Hence, in the specular direction where $\theta_1 = \theta_2 = \theta$ and $\theta_3 = 0^{\circ}$, the scattering function S_{hf} reduces to the following expression:

$$S_{hf} = \frac{f^2(\theta)\ R^2}{2\ (\cos\theta_1+\cos\theta_2)^2 <\zeta'^2>} e^{-\frac{K^2}{(2\gamma^2<\zeta'^2>)}} \qquad (68)$$

$$S_{hf} = \frac{R^2}{8\pi<\zeta'^2>}$$

as

$$f(\theta) = \cos\theta$$

$$\gamma = k\cos\theta$$

$$\alpha = 0$$

$$x = \frac{\alpha}{\cos\theta} = 0$$

As pointed out in the previous paragraph, the reflection of very high frequency signals by the sea surface yields scattered radiation that is incoherent under the assumption that

$$4\gamma^2\sigma^2 >> 1$$

$$(2\gamma^2<\zeta'^2>) >> \frac{1}{R^2}$$

Before we launch into the calculations, we will verify these criteria for the frequency range of interest: 60 and 30 kHz.

Utilizing

$$\gamma^2 = k^2 \cos^2\theta \qquad \alpha = 8.1 \times 10^{-3}$$

$$\sigma^2 = \frac{\alpha W^4}{4\beta g^2} \qquad \beta = 0.74$$

$$<\zeta'^2> = (3 + 5.12W) \times 10^{-3} \qquad g = 9.81 \text{ m/s}^2$$

and assuming a windspeed of 10 m/s (SS3) yields

$$\alpha^2 = 0.30 \text{ m}^2 \; ; \; \sigma = 0.55 \text{ m}$$

$$<\zeta'^2> = 5.42 \times 10^{-2}$$

For 60 kHz(λ = .025 m) and low grazing angles, e.g., $\theta = 85^{\circ}$

$$4\gamma^2\sigma^2 = 5.75 \times 10^2 >>1$$

$$(2\gamma^2<\zeta'^2>) = 5.2 \times 10^1 >> \frac{1}{R^2}$$

and the first order $5.2>>\frac{1}{R^2}$, $R \gtrsim 0.5$m.

Thus, for the 60 kHz case, the criteria are fulfilled.

For 30 kHz (λ=.05m) and $\theta=85^{\circ}$.

$$4\sigma^2\gamma^2 = 1.44 \times 10^2>>1$$

$$(2\gamma^2<\zeta'^2>) = 13>> \frac{1}{R^2}$$

again the first order $R > 1.0$ m.

Thus, also for the 30 kHz case the criteria are fulfilled.

Similarly, for the shadowing function in the specular direction

$$0<\theta_1 = \theta_2 = \theta < \pi/2 \quad \text{and } \theta_3 = 0$$

we obtain the following simplified expression

$$S(\theta) = S(\theta_1,\theta_2) = \frac{[1-\exp(-4B)]\mathrm{erf}v}{4B} \qquad (69)$$

as

$$v_1 = v_2 = v = \frac{|\eta|}{(2\sigma^2|\psi_o''|^{\frac{1}{2}}} = \frac{|\eta|}{(2\Sigma^2)^{\frac{1}{2}}}$$

$$\eta_1 = \eta_2 = \eta = \cot\theta$$

$$B_1 = B_2 = B = \frac{[\exp(-v^2)-\sqrt{\pi}\ v\ \mathrm{erfc}\ v]}{4\sqrt{\pi}\ v}$$

In summary, for specular scattering at the high frequency limit, the expected average value of p^2, where p is the pressure field at the receiver, is then obtained from the following simplified expressions:

$$<s^2> = <pp^*> \frac{AS(\theta)}{R_2{}^2} S_{hf} \qquad (70)$$

$$<s^2> = <pp^*> \frac{AS(\theta)R^2}{8\pi R_2{}^2<\zeta^{12}>}$$

where

$$S(\theta) = \frac{1-\exp(-4B)\mathrm{erf}v}{4B}$$

$$v = \frac{|\eta|}{(2\Sigma^2)^{\frac{1}{2}}}$$

$$|\eta| = \cot\theta$$

$$B = \frac{[\exp(-v^2)-\sqrt{\pi}v\ \mathrm{erfc}\ v]}{4(\pi)^{\frac{1}{2}}\ v}$$

$$\langle \zeta'^2 \rangle = \Sigma^2 = (3 + 5.12W) \times 10^{-3} \; ; \; W = \text{windspeed in m/s.}$$

$$R = \frac{\rho' c' \cos\theta - \rho\, c \cos\theta'}{\rho' c' \cos\theta + \rho\, c \cos\theta'} \; ; \; \frac{c}{\sin\theta} = \frac{c'}{\sin\theta'}$$

From Ref. 19 we use the following air/sea water interface data:

1. For air $c' = 343$ m/s and $\rho' c' = 415$ Rayls.
2. For sea water $c = 1500$ m/s and $\rho c = 1.54 \times 10^6$ Rayls.

The estimation of the illuminated area A for specular scattering where $\theta_1 = \theta_2 = 0$ and $\theta_3 = 0$, is based on the geometry illustrated in Fig. 24b. The illuminated area is given by

$$A = \pi a b \tag{71}$$

Assuming the following data to be known

h_s = depth of the source

h_r = depth of the receiver

$\Delta\phi$ = the half beam width of the directional receiver.

Both a and b of Eq. (71) can be calculated in terms of the detection range R_D as follows:

$$x_2 = \frac{R_D\, h_r}{h_s + h_r} \tag{72}$$

$$x_1 = R_D - x_2 = R_D\left(1 - \frac{h_r}{h_s + h_r}\right) \; ; \; \theta = \tan^{-1}\left(\frac{R_D}{h_s + h_r}\right)$$

$$R_1 = \frac{x_1}{\sin\theta}$$

$$R_2 = \frac{x_2}{\sin\theta}$$

To a good approximation when $\theta = \pi/2$, we have

$$a = x_1 = R_D(1 - \frac{h_r}{h_s+h_r}) \qquad (73)$$

$$b = R \sin(\Delta\phi) = \frac{R_D \; h_r}{(h_s+h_r)\sin\theta} \sin(\Delta\phi)$$

The expression for $<s^2>$ is then introduced as a supplement to the direct path to the receiver in the following way:

By utilizing the relationship

$$I = \frac{\overline{p^2}}{\rho c} \qquad (74)$$

for the intensity, the scattering intensity at the receiver and the intensity at the ensonified area are, respectively,

$$I_s = \frac{\overline{p^2}}{\rho c} = \frac{<s^2>}{c}$$

$$I_1 = \frac{\overline{p_1^2}}{\rho c} = \frac{<p_1 p_1{}^*>}{\rho c}$$

Equation (70) can thus be written as

$$I_s = I_1 \frac{AS(\theta) \;\; R^2}{8\pi R_2{}^2 <\zeta^{1\,2}>}$$

$$I_s/I_1 = \frac{AS(\theta) \;\; R^2}{8\pi R_2{}^2 <\zeta^{1\,2}>}$$

$$10\log I_s/I_1 = 10\log \frac{I_s/I_{ref}}{I_1/I_{ref}} = K_o$$

$$IL_s = IL(R_1) = K_o \qquad (75)$$

We then have to determine $IL(R_1)$

$$TL = SPL(1) - SPL(R_1) = 20\log R_1 \qquad (76)$$

$$SPL(R_1) = IL(R_1) = 10\log I_1$$

$$SPL(1) = SL$$

yielding

$$IL(R_1) = SL - 20\log R_1 = K_1 \qquad (77)$$

Then

$$IL_{suppl} = K_o + K_1 \qquad (78)$$

is the supplement to the direct path, and

$$IL_{direct} = SL - 20\log R_D = K_3$$

$$I_{direct}/I_{ref} = \text{anti log} \frac{IL_{direct}}{10} = K_4$$

$$I_{suppl}/I_{ref} = \text{anti log} \frac{IL_s}{10} = K_5$$

The total intensity of the receiver is thus

$$I_{Tot}/I_{ref} = \frac{I_{direct} + I_{suppl}}{I_{ref}} = K_4 + K_5 = K_6$$

$$IL_{Tot} = 10\log K_6 = K_7 \qquad (79)$$

Thus, the effect of the randomly rough surface compared to the idealized free-field condition can be expressed as

$$\Delta IL = IL_{Tot} - IL_{direct} = K_8 \qquad (80)$$

A calculator program on a Texas Instrument 59 (later called TI 59) was developed to perform these calculations. A block diagram of the program is outlined in Fig. (26) and the programs steps together with a detailed description is given in Appendix B. The calculations are based on the following fixed data

$h_s = 2$ m

$h_r = 6$ m

$\Delta\phi = 10^{\circ}$

$W = 10$ m/s (SS3)

Then, varying the detection range from R = 2000 m to 100 m gives the difference between IL_{Tot} and IL_{direct} plotted in Fig. (27).

E. CONCLUSION AND DISCUSSION

As seen from Fig. (27) the supplementary effect of the scattering from a rough surface in the high frequency case is negligible compared to the direct path.

In saying so, it also should be pointed out that the Helmholtz-Kirchhoff's approach may be limited as it does not take into account the diffraction effects from crests

and throughs of the ensonified area, an effect which becomes increasingly important at low grazing angles, high frequency and when the rough surface is a superposition of swell and capillary waves.

VII. THE EFFECT OF SCATTERING AND ABSORPTION FROM THE SUB-SURFACE OCEAN LAYER

A. GENERAL SCATTERING THEORY

Generally when a region (volume) scatters sound, some of the energy carried by the incident wave is dispersed.

The energy lost by the incident wave may be absorbed by the scatterers or it may be simply deflected from its original course. The amount of energy lost per second by the incident wave divided by the incident wave's intensity is called the total cross section σ_e of the region and is the sum of the absorption and scattering cross sections

$$\sigma_e = \frac{\Pi_s + \Pi_a}{I_p}$$

where

Π_s = scattered power

Π_a = absorbed power

The existence of gas bubbles in the subsurface ocean layer modifies the forward scattering in the following two major ways:

1. The bubbles can resonate. When the bubbles are excited at a frequency near its natural frequency, it very efficiently absorbs and scatters the incident wave. At resonance, the scattering and

absorption cross section of a typical bubble at sea is of the order 10^3 times its geometrical cross section.

2. The bubbles change the effective compressibility of the water and cause the speed of sound to be a function of frequency, i.e., the medium is dispersive.

We will investigate and discuss these effects by separately estimating:

1. The attenuation due to the bubbles and
2. the refraction by bubbles.

B. ABSORPTION MODEL

The choice of model for the subsurface ocean layer depends on whether the medium has a teneous or a dense distribution of scatterers. When the bubble density is teneous, both "single scattering" and "first order multiple scattering" approximation solutions are applicable.

On the other extreme, when the bubble density is high, the so-called "diffusion" approximation can be used. Between these two extremes, multiple scattering effects are important.

The multiple scattering theory, which in the limit also contains the first order approximation, will be used to estimate effects of attenuation due to bubbles, on the propagation of propeller noise from the target to the torpedo.

The geometry of the propagation model is illustrated in Fig. (28) where it is assumed that a plane wave is incident on a semi-infinite (disregarding the sea surface) slab of thickness x containing a number of randomly distributed bubbles. The plane wave approximation is valid if the incident sound has a wavelength λ much greater than the bubble-radius a

$$ka<<1$$

where

$$k=\omega/c=2T/\lambda$$

The receiver is located outside the slab and the beam pattern of the receiver is represented by the solid angle Ω_r.

We are interested in the estimating of the total power received, taking into account the multiple scattering process in the inhomogeneous slab as well as the beam pattern of the receiver.

The mathematical formulation of this problem is based on Twersky's theory of multiple scattering. Since the theory is presented in Ref. 20 only, the basic formulation, major assumptions, and the end results will be presented here.

The total intensity is the average of the square of the magnitude of the total field:

$$<|\psi^a|^2> = <|<\psi^a> + \psi_f^{\,a}|^2> = |<\psi^a>|^2 + <|\psi_f^{\,a}|^2> \quad (81)$$

where

$$\psi^a = \psi_i^{\,a} + \sum_{s=1}^{N} u_s^{\,a}$$

the scalar field at the receiver location $\vec{r}_a$, see Fig. (29), is the sum of the incident wave ϕ_i and the contribution from all N scatterers. $|<\psi^a>|^2$ is the coherent intensity based on the average field $<\psi^a>$. $<|\psi_f^{\,a}|^2>$ is the incoherent intensity based on the fluctuating field $\psi_f^{\,a}$.

In Twersky's theory, the multiple scattering process is described by the following set of integral equations which Eq. (81) must satisfy:

$$<|\psi^a|^2> = |<\psi^a>|^2 + \quad |v_s^{\,a}|^2 <|\psi^s|^2>\rho(\vec{r}_s)d\vec{r}_s \quad (82)$$

where

$$v_s^{\,a} = U_s^{\,a} + \quad U_t^{\,a}\, v_s^{\,t}\, \rho(\vec{r}_t)dt$$

is an operator representing all the scattering processes from s to a. (See Fig. (28).) It should be noted that Twersky's theory includes all the multiply scattered waves that involve chains of successive scattering going through different scatterers. (See Fig. (29a).) However, the theory neglects the terms which include an individual scatterer more than once, as illustrated by Fig. (29b).

Thus Twersky's theory is expected to give good results when back scattering is insignificant compared to the scattering in other directions.

As typical for most integral equations, Twersky being no exception, detailed complete solutions are difficult to obtain. However, Twersky gave an approximate solution to Eq. (81) and Eq. (82), which according to Ref. 20 have been found to agree reasonably well with experimental data. This solution is based on the following main assumptions:

- Backscattering is assumed to be small compared to scattering in other directions.
- Scattering is mostly concentrated in the forward direction. This is reasonable based on the assumed random distribution of the bubbles; i.e., no reinforcement of the radiation pattern occurs except in the direction of the incident wave.
- The angle θ_{as} is small, i.e., $\theta_{as} = 0^{\circ}$.

This leads to the following expression for the total intensity at the receiver:

$$\langle|\psi^a|^2\rangle = T = \exp(-\rho\sigma_a x)\ \exp(-\rho\sigma_s x) + q[1-\exp(-\rho\sigma_s x)] \quad (83$$

where

σ_a = absorption cross section

σ_s = scattering cross section

$$q = \frac{\int_{\Omega_r} |f|^2 d\Omega_s}{\int_{4\pi} |f|^2 d\Omega_s}$$

where

f = the amplitude function

q = the fraction of total scattered power collected by the receiver as illustrated in Fig. 30 and

ρ = is the bubble density, i.e., the number of scatterers per unit volume.

For small values of ρx we see from Eq. (82) that the coherent part dominates:

$$\ln T \approx -(\sigma_a+\sigma_s)\rho x \tag{84}$$

In this limit the multiple scattering result is equivalent to that obtained from single scattering considerations.

For large values of ρx which corresponds to very dense or very wide slab of scatterers, the incoherent intensity dominates

$$\ln T \approx \ln q - \sigma_a \rho x \tag{85}$$

In this latter case, it is notable that when $\Omega_r \geq 2\pi$, the receiver collects almost all the scattered power

$$\ln T \approx - \sigma_a \rho x \tag{86}$$

The first case, representing the situation for teneous density of scatterers and/or narrow beam pattern of the receiver, gives a good approximation to the situation of interest in the thesis. It also represents the case for

which no scattered power is received. This will be approximately true for a narrow-beam width receiver. We will, therefore, investigate the coherent intensity first.

Also, the incoherent case, as represented by Eq. (86) will be investigated, where only losses due to absorption are incorporated.

C. THE COHERENT INTENSITY CASE

For the coherent case the intensity level after the incident wave has traversed a distance x is

$$I_x = I_p \exp[-(\sigma_a+\sigma_s)\rho x] \tag{87}$$

where

I_p = incident plane wave intensity.

The change in intensity over the distance x is

$$\Delta IL = 10\log\frac{I_x}{I_p} = \frac{I_p \exp[-(\sigma_a+\sigma_s)\rho x]}{I_p} \tag{88}$$

$$= 10\log\exp[-(\sigma_a+\sigma_s)\rho x]$$

The excess attenuation per unit distance due to bubbles is thus

$$\alpha = -\frac{\Delta IL}{x} = -\left[\frac{-(\sigma_a+\sigma_s)\ \rho x \log e}{x}\right]$$

$$= (\sigma_a+\sigma_s)\ \rho \log e$$

$$\alpha = 4.34\ \sigma_e\ \rho, \text{ in dB/m.} \tag{89}$$

However, this only takes into account bubbles of one size. In a bubbly medium there is a spectrum of radii.

The probability density function for finding a bubble size between radii a and a+da is

$$W(a) = \frac{n(a)}{\rho} \tag{90}$$

where

$$\int_0^\infty W(a)da = 1$$

$n(a)da$ is the number of bubbles per unit volume having radii between a and a+da. It is common to use da=1 μm.

$\rho = \int_0^\infty n(a)da$ is the total number of bubbles per unit volume.

As the extinction cross section also is a function of the radius (See Eq. (93).), the absorption due to bubbles is obtained by integrating Eq. (89) over all possible radii

$$\alpha = 4.34 \int_0^\infty \sigma_e(a)n(a)da \tag{91}$$

To calculate the absorption coefficient, the extinction cross section σ_e must be derived from the general bubble dynamic relationship. This is done in detail by C. Clay and H. Medwin [Ref. 21] from which the following results are taken.

The scattering cross section

$$\sigma_s = \frac{\Pi_s}{I_p} \tag{92}$$

$$= \frac{4\pi a^2}{[(f_r/f)^2-1]^2+\delta^2}$$

where

f_r = resonance frequency = $\frac{1}{2\pi a}\left(\frac{2\gamma b\beta P_A}{\rho_A}\right)^{\frac{1}{2}}$

$f = f_o$ = operating frequency

δ = damping constant = $\delta_r + \delta_t + \delta_v$

$= ka + (\frac{d}{b})(\frac{f_r}{f})^2 + \frac{4\mu}{\rho_A \omega a^2}$

a = bubble radii

$\frac{d}{b} = 3(\gamma-1)\left[\frac{\underline{X}(\sin h\ \underline{X} + \sin \underline{X}) - 2(\cos h\ \underline{X} - \cos \underline{X})}{\underline{X}^2(\cos h\ \underline{X} - \cos \underline{X}) + 3(\gamma-1)(\sin h\ \underline{X} - \sin \underline{X}}\right]$

$\underline{X} = a\left(\frac{3w_{\rho g} C_{\rho g}}{k_g}\right)^{\frac{1}{2}}$

k_g = thermal conductivity of gas

ρ_g = density of gas = $\rho_{gA}[1+\frac{2\tau}{(\rho_A a)}](1+0.1z)$

ρ_{gA} = density of gas at sea level

τ = surface tension

$P_A = 1.013 \times 10^6(1+0.1z)$

z = bubble depth in m.

C_{pg} = specific heat of constant pressure of gas

μ = shear viscosity of water

γ = 7/5, for diatomic gas

ρ_A = density for sea water

$$b = [1+(\frac{d}{b})^2]^{-1} \; [1 + \frac{3\gamma-1}{\underline{X}} \; \frac{\sin h \, \underline{X} - \sin \underline{X}}{\cos h \, \underline{X} - \cos \underline{X}}]^{-1}$$

$$\beta = 1 + \frac{2\tau}{P_A a} (1 - \frac{1}{3\gamma b})$$

Furthermore:

$$\sigma_e = \sigma_a + \sigma_s = \frac{4\pi a^2 (\delta/ka)}{[(f_r/f)^2 - 1]^2 + \delta^2} \tag{93}$$

and

$$\sigma_a = \sigma_e - \sigma_s \tag{94}$$

A detailed computer program, as outlined in Appendix B, was developed for the TI 59 to handle the derivation of σ_s, σ_e, and σ_a based on an assumed receiver depth of z = 6 m.

For the 60 kHz case, both the extinction cross section σ_e and the absorption cross section σ_a are given in Fig. 31 as a function of bubble radius a.

Similarly, Fig. 32 gives σ_e and σ_a for the 30 kHz case. Superimposed on these figures are the curves for n(a)da as calculated from the following: Figures 5 - 7 of Ref. 2 give the resonant bubble densities in a 1 μm band as a function of depth and with the wind speed as parameter for the three discrete frequencies 12 kHz, 38 kHz and 120 kHz.

Based on these data, Fig. 33 shows the interpolated bubble density as a function of resonance frequency for sea state 2, 3, and 6.

Furthermore, both A. Lövik [Ref. 2] and H. Medwin [Ref. 3] found that the bubble density function n(a) decreases with increasing bubble radii as

$$n \alpha a^{-x}$$

where H. Medwin [Ref. 3] found the power law of:

$x = 4$ for $a < 50\text{-}80$ μm.

$x = 2$ for $a > 50\text{-}80$ μm.

and A. Lövik [Ref. 2] found the power law of:

$x = 4.2$ between 38 kHz and 120 kHz

$x = 2.6$ between 12 kHz and 38 kHz

which, averaged over the depth interval, corresponds to the bubble radii of 380 μm(12 kHz), 120 μm (38 kHz) and 49 μm (120 kHz).

As suggested by A. Lövik [Ref. 2], the discrepancy between the two observations is not great and may be due to the few measuring frequencies used in the work of A. Lövik.

In summary, Fig. 33, from which we obtain the appropriate resonant bubble density in a 1 μm band $n(a_R)$ together with the power law $n \alpha a^{-x}$, comprise the full knowledge of n(a)da.

Performing a multiplication of σ_e and n(a)da, we obtain Fig. 34 and Fig. 35 for the 60 kHz and the 30 kHz case, respectively.

Finally, the integral

$$\int_0^\infty \sigma_e(a)n(a)da$$

was evaluated using a numerical integration based on Simpson's discrete approximation programmed for the TI 59 and documented in Appendix C.

Based on the above, the following absorption coefficient for the coherent case is obtained for f = 60 kHz

$$\alpha = 4.34 \int_0^\infty \sigma_e(a)n(a)da = 4.34\ (2.016 \times 10^{-1})$$

$$= 8.75 \times 10^{-1}\ \text{dB/m}.$$

$$\alpha \approx 0.88\ \text{dB/m} \tag{95}$$

with

$n(a_R) = 1000$

$n(a)\ \alpha\ a^{-4}$

$z = 6$ m.

Thus, it is seen that the attenuation due to bubbles is considerably greater than the "normal attenuation" due to chemical and viscous relaxation processes in sea water, which for the 60 kHz case is

$\alpha = 0.02$ dB/m.

Thus, the total absorption coefficient for the 60 kHz case is

$$\alpha \approx 0.90 \text{ dB/m.} \tag{96}$$

For f = 30 kHz, the absorption coefficient due to bubbles in the coherent case is

$$\alpha = 4.34 \int_0^\infty \sigma_e(a)n(a)da = 4.34\ (3.8375 \times 10^{-2})$$

$$= 1.665 \times 10^{-1} \text{ dB/m.}$$

$$\alpha \approx 0.17 \text{ dB/m} \tag{97}$$

with

$$n(a_R) = 20$$

$$n(a)\ \alpha\ a^{-2.6}$$

$$z = 6 \text{ m.}$$

For this case, the power law dependence of $n(a)\ \alpha\ a^{-2}$ gives

$$\alpha = 1.655 \times 10^{-1}$$

Thus, the difference in power law dependence makes no significant difference in the absorption coefficient.

The absorption coefficient due to chemical and viscous relaxation processes is at 30 kHz

$$\alpha = 0.012 \text{ dB/m.}$$

The total absorption coefficient in the coherent case is

$$\alpha \approx 0.18 \text{ dB/m.} \tag{98}$$

D. THE INCOHERENT INTENSITY CASE

For the incoherent case, where only losses due to absorption are included, the product σ_a and n(a)da for the 60 kHz and 30 kHz cases are given in Fig. 36 and Fig. 37, respectively. Performing a numerical integration based on the Simpson's discrete approximation leads to the following results:

For f = 60 kHz, the absorption coefficient due to bubbles is

$$\alpha = 4.34 \int_0^\infty \alpha_a(a)n(a)da = 4.34\ (1.66 \times 10^{-1})$$

$$\alpha \approx 0.72 \text{ dB/m.} \tag{99}$$

with

$$n(a_R) = 1000$$

$$n(a)\ \alpha\ a^{-4}$$

$$z = 6 \text{ m.}$$

Adding the "normal attenuation" in sea water for f = kHz, yields a total absorption coefficient of

$$\alpha \approx 0.74 \text{ dB/m} \tag{100}$$

For f = 30 kHz, the absorption coefficient due to bubbles is

$$\alpha = 4.34 \int_0^\infty \sigma_a(a)n(a)da = 4.34\ (2.975 \times 10^{-2}) \tag{101}$$

$$\alpha \approx 0.13 \text{ dB/m}$$

with

$$n(a_R) = 20$$

$$n(a) \propto a^{-2}$$

$$z = 6 \text{ m.}$$

Adding the "normal attenuation" in sea water for $f = 30$ kHz yields a total absorption coefficient in the incoherent case of

$$\alpha \approx 0.14 \text{ dB/m} \qquad (102)$$

E. SUMMARY AND DISCUSSION OF THE BUBBLE ATTENUATION

As seen from the above, the attenuation due to bubbles in the subsurface ocean layer is important for high frequency and high Sea State.

Accounting for the effect of bubbles at Sea State 3 in summary we found the following absorption coefficients in dB/m:

f = 60 kHz		f = 30 kHz	
coherent	incoherent	coherent	incoherent
$\alpha = 0.88$	$\alpha = 0.72$	$\alpha = 0.17$	$\alpha = 0.13$

The main assumptions were:

- -the back scattering is small compared to that in other directions.
- -the scattering is mostly concentrated in the forward direction.

-the angle θ_{as} between the scatterer and the receiver is small, i.e., $\theta_{as} \simeq 0^{\circ}$.

-the depth of the receiver is z = 6 m.

-the sea state is 3.

The range dependent portion of the passive sonar Eq. (1) $TL=-20\log R-\alpha R$ for both the 60 kHz and 30 kHz scattering results can now be compared with the reference data obtained in Section V.

For f = 60 kHz, Fig. 22 gives $TL=-20\log R-\alpha R$ as a function of R with

1. α = 0.021 dB/m, the "normal attenuation" due to chemical and viscous relaxation processes.
2. α = 0.9 dB/m, the total attenuation including the effect of bubbles in the coherent case.
3. α = 0.74 dB/m, the total attenuation including the effect of bubbles in the incoherent case.

For the same example as in the reference model, Fig. 22 yields the detection ranges for 60 kHz.

$$R = 1200 \text{ m for } \alpha = 0.021 \text{ dB/m} \tag{103}$$

$$R = 60 \text{ m for } \alpha = 0.90 \text{ dB/m}$$

$$R = 70 \text{ m for } \alpha = 0.74 \text{ dB/m}$$

Not surprisingly, this result seems to exclude the possibility or having both a searching and attack depth near the surface, i.e., z = 6 m, for a torpedo system operating in a high frequency region, f = 60 kHz.

Similarly, for $f = 30$ kHz, Fig. 23 gives $TL=-20\log R-\alpha R$ as a function of R with

1. $\alpha = 0.012$ dB/m, the "normal attenuation" in sea water.
2. $\alpha = 0.18$ dB/m, the total attenuation including the effect of bubbles in the coherent case.
3. $\alpha = 0.14$ dB/m, the total attenuation including the effect of bubbles in the incoherent case.

For the same detection example as in the reference model, Fig. 23 yields the detection ranges for 30 kHz:

$$R = 2400 \text{ m for } \alpha = 0.012 \text{ dB/m} \tag{104}$$

$$R = 250 \text{ m for } \alpha = 0.18 \text{ dB/m}$$

$$R = 310 \text{ m for } \alpha = 0.14 \text{ dB/m.}$$

Again, the bubbles give a major decrease in the detection range. A detection range of R = 250 m seems marginally acceptable as the turn rate requirement for a pursuit homing trajectory may become excessive.

The above results are summarized in Tables III and IV for the 60 kHz and 30 kHz, respectively.

F. THE REFRACTION BY BUBBLES

The presence of bubbles in the sea water affects the speed of sound (phase speed) primarily because of the change in compressibility. The derivation of this dispersive relationship on the sound speed has been done by H. Medwin

TABLE III

DETECTION PARAMETERS AND RANGES FOR f=60 kHz

SL	DI	NL	P_D	P_{FA}	DT	Detection Range (m)			SS	f
dB	dB	dB			dB	α=.021	α=.9	α=.74		kHz
100	-180	-124	.5	10^{-6}	-6.5	1200	60	70	3	60
100	-180	-124	.5	10^{-99}	0	1000	--	--	3	60

TABLE IV

DETECTION PARAMETERS AND RANGES FOR f=30 kHz

SL	DI	NL	P_D	P_{FA}	DT	Detection Range (m)			SS	f
dB	dB	dB			dB	α=.012	α=.18	α=.14		kHz
106	-180	-124	.5	10^{-6}	-6.5	2400	250	310	3	30
106	-180	-124	.5	10^{-99}	0	2200	220	290	3	30

[Ref. 22]. H. Medwin showed that the bubbles with resonant frequencies greater than the incident frequency decrease the sound speed, while bubbles with resonant frequency lower than the incident wave increase the sound speed.

Furthermore, H. Medwin [Ref. 22] predicts the sound speed gradient due to bubbles as a function of depth for a frequency range and wind speed compatible with our domain of interest. He found the gradients

$$g = \partial c/\partial z = 0.26 \text{ s}^{-1} \text{ at } z = 0 \text{ m.}$$

$$g = \partial c/\partial z = 0.016 \text{ s}^{-1} \text{ at } z = 10 \text{ m.}$$

$$g = \partial c/\partial z = 0.005 \text{ s}^{-1} \text{ at } z = 20 \text{ m.}$$

For comparison, the sound speed gradient due to pressure in an isothermal water is

$$g = 0.017 \text{ s}^{-1}$$

This shows that the rays in the top 10 m are strongly influenced by bubbles. However, with respect to our surface scattering model (Section VI) where both the source and the receiver are situated very close to the surface and where relatively short propagation distances are encountered, this refraction phenomenon is assumed to have negligible effect.

VIII. THE TURN RATE LIMITATION

As pointed out in the previous section, the presence of bubbles near the surface may significantly reduce the range at which the target can be detected.

In this section, the turn rate necessary during pursuit homing at the previous estimated detection ranges will be studied. A computational procedure will be used to determine the range of angles on the bow (AOB) of the target at the beginning of homing which lead to miss on the initial attack. A trajectory where the torpedo velocity vector always is directed towards the instantaneous target position is called a pursuit homing trajectory. The derivation of the pursuit homing trajectory follows P. van Nostrand [Ref. 23] and is based on the geometry of Fig. 38, where

r = approach angle, i.e., angle between ship velocity vector and the line of sight.

AOB = 180 - ϕ

The equation of motion is obtained by taking the component along r and the normal to r, yielding

$$\dot{r} = V_s \cos \phi - V_T \tag{105}$$

$$r\dot{\phi} = -V_s \sin \phi \tag{106}$$

where

$\dot{r}$ = range rate

$\dot{\phi}$ = turn rate

V_s = target speed

V_T = torpedo speed.

Dividing Eq. (105) by Eq. (106) yields:

$$\frac{\dot{r}}{r} = \left(\frac{V_T}{V_s}\frac{1}{\sin\phi} - \cot\phi\right)\dot{\phi} \quad ; \; r \neq 0$$

and defining

$$\frac{V_T}{V_s} \triangleq p$$

yields

$$\frac{\dot{r}}{r} = \left(\frac{P}{\sin\phi} - \cot\phi\right)\dot{\phi} \tag{107}$$

$$r = K\frac{(\sin\phi)^{P-1}}{(1+\cos\phi)^{P}} \tag{108}$$

Then, introducing the initial conditions: r_o, ϕ_o where

r_o: initial detection range

ϕ_o: initial approaching angle

yields

$$K = r_o\frac{(1+\cos\phi_o)^{P}}{(\sin\phi_o)^{P-1}} \tag{109}$$

For the geometry of Fig. 38, the turning rate is given by Eq. (105).

$$\dot{\phi} = -\frac{V_s}{r} \sin \phi \tag{110}$$

Substituting Eq. (108) into Eq. (110) yields:

$$\dot{\phi} = -\frac{V_s (1+\cos \phi)^P}{K(\sin \phi)^{P-2}} \tag{111}$$

From Eq. (108) we see that $r \to 0$ as $\phi \to 0$, i.e., ϕ tends to zero as the torpedo approaches the target ship. It is further of interest to determine the limiting value of the turning rate as the torpedo approaches the target for various values of the parameter p. This is done by taking the derivative of $\dot{\phi}$ with respect to ϕ. Thus, from Eq. (109) we get

$$\frac{d\dot{\phi}}{d\phi} = -\frac{V_s}{K} (\sin \phi)^{1-P} \, [1+\cos\phi]^P \, [2 \cos \phi - p] \tag{112}$$

For $1<p<2$, we see that Eq. (112) is zero at

$$\cos \dot{\phi} = P/2 \tag{113}$$

$$\dot{\phi} = \cos^{-1}(P/2)$$

with an associated maxima

$$|\dot{\phi}_{max}| = \frac{V_s (1+P/2)^P [1-(P/2)^2]^{1-P/2}}{K} \tag{114}$$

Furthermore, the turn rate for $p<2$ at impact is zero as the limit of Eq. (109) yields:

$$\lim_{\phi \to 0} \dot{\phi} = -\frac{V_s}{K} \lim_{\phi \to 0} (\sin \phi)^{2-P} [1+\cos \phi]^P \to 0 \tag{115}$$

For p=2 we see from Dq. (111) that

$$\lim_{\phi\to 0} \dot{\phi} = -\frac{V_s}{K} \lim_{\phi\to 0}(1+\cos\phi)^2 = -\frac{4V_s}{K} \qquad (116)$$

For p>2 we see from Eq. (111) that there is no zero value of $d\dot{\phi}/d\phi$ between $\phi = 0^\circ$ and $\phi = 180^\circ$, since all terms of Eq. (112) are nonzero terms for $0^\circ < \phi < 180^\circ$. Furthermore, the turn rate for p>2 at impact is

$$\left|\lim_{\phi\to 0} \dot{\phi}\right| = \left|-\frac{V_T}{K} \lim \frac{(1+\cos\phi)^P}{(\sin\phi)^{P-2}}\right| \to \infty \qquad (117)$$

as $(\sin\phi) \to \infty$ since $(p-2) > 0$.

Furthermore, as $\phi \to 180^\circ$, we get from Eq. (112)

$$\lim_{\phi\to 180} \frac{d\dot{\phi}}{d\phi} = \frac{V_o}{K}(2+p) \lim (\sin\phi)^{1-P}(1+\cos\phi)^P$$

Evaluating

$$\lim_{\phi\to 180} (\sin\phi)^{1-P} (1+\cos\phi)^P = \lim_{\phi\to 180} (\sin\phi)\left(\frac{1+\cos\phi}{\sin\phi}\right)^P$$

by applying l' Hopitale rule to the term

$$\lim_{\phi\to 180} \frac{1+\cos\phi}{\sin\phi} = \lim_{\phi\to 180} \frac{-\sin\phi}{\cos\phi} \to 0$$

Thus, the product $\sin\phi\left(\frac{1+\cos\phi}{\sin\phi}\right)^P$ approaches zero for any p>1, since both terms in this product approach zero as $\phi \to 180$.

Figure 39 shows a plot of computed values of $|\dot{\phi}K/V_s|$ for different values of p>1. From this we can draw the following summarizing conclusions.

For 1<p<2 the turn rate has

- a maximum value at $\dot{\phi}=\cos^{-1}(p/2)$
- the zero value at $\phi=0^{\circ}$ and $\phi=180^{\circ}$.

For p=2 the turn rate

- is zero at $\phi=180^{\circ}$.
- monotonically increasing with decreasing ϕ approaching the value $(4V_s/K)$ when $\phi=0^{\circ}$.

For p 2 the turn rate

- is zero at $\phi=180^{\circ}$.
- is monotonically increasing with decreasing ϕ approaching ∞ as $\phi=0^{\circ}$.

As seen from the above for p>2, the turn rate increases monotonically with decreasing approaching an infinite turn rate to hit a point target. To avoid this singularly we must make some provision. If the torpedo's maximum turn rate is exceeded only at some very small range, a hit is likely.

Figure 40 illustrates the hit criterion used. Assume a rudder of length L_R is situated directly behind the propeller which is idealizer as an acoustic point source.

If the torpedo becomes turn rate limited at some range r=r', it at best can proceed along a circular path which lags the desired pursuit trajectory, or at worst it can

loose acoustic contact and go into "hold-in," maintaining a constant heading at the angle ϕ'. In this last case, it will cross the line of target ship's course in the time:

$$t = r'/V_r \tag{118}$$

If this advance is less than the length of the rudder L_R, the torpedo will impact the rudder. Hence, the limiting condition is

$$\frac{r'}{p} = L_R$$

$$r' = pL_R \tag{119}$$

For this analysis, we have arbitrarily chosen

$$L_R = 3 \text{ m} \tag{120}$$

Thus, the torpedo's turn rate has not been exceeded when the range to the target is

$$r' = pL_R = 3\ p \tag{121}$$

and a hit is assumed.

Now we can analyze the cases $p>2$ and $1<p<2$ on the same footing. If we match the torpedo's maximum turn rate to a particular range r', it is certain that its turn rate has not been exceeded earlier in the run.

This turn rate-range matching is done by substituting the "hit-range" defined as $r' = 3\ p$ into Eq. (106) and solving it for $\sin\phi$, yielding

$$\dot{\phi}_{max} = -\frac{V_s}{3p} \sin \phi$$

$$\sin \phi = -\frac{\dot{\phi}_{max}(3p)}{V_s}$$

Since $\dot{\phi}$ is always negative, sin ϕ is always positive and equal to

$$\sin \phi = \frac{3p|\dot{\phi}|_{max}}{V_s} \tag{122}$$

Two values of ϕ satisfies this equation, and they are denoted

$$\phi_A = \sin^{-1} \frac{3p|\dot{\phi}|max}{V_s}; \text{ for } \phi \leq 90^{\circ} \tag{123}$$

$$\phi_B = 180^{\circ} - \phi_A$$

A unique value of K may now be found using Eq. (111) for each of the angles ϕ_A and ϕ_B.

$$K = \frac{V_s(1+\cos \phi)^P}{|\dot{\phi}|_{max}(\sin \phi)^{P-2}}$$

These values of K are designated as K_A and K_B, and for each there is a corresponding value of ϕ_o from Eq. (109) with ϕ_o given by the initial detection range

$$(\phi_o)_A \text{ and } (\phi_o)_B$$

In the case of $1<p<2$, the turn rate does not necessarily increase monotonically during the pursuit homing trajectory, and we must check that either ϕ_A or ϕ_B, respectively, is not beyond the angle corresponding to $\dot{\phi}_{max}$.

As seen from Eq. (113), the turn rate reaches a maximum at an angle given by

$$\phi^* = \cos^{-1}(P/2)$$

with a corresponding turn rate given by

$$|\dot{\phi}|_{max} = \frac{V_s(1+P/2)^P \ [1-(P/2)^2]^{1-P/2}}{K}$$

Thus, the value of K = K* for which the limiting turn rate is achieved

$$K = \frac{_s(1+P/2)^P[1-(P/2)^2]^{1-P/2}}{|\dot{\phi}|_{max}}$$

It is important to note that, if $\phi_A<\phi^*<(\phi_o)_A$, the "A" trajectory is invalid since the maximum turn rate of the torpedo, reached at the range r = 3p at $\phi = \phi_A$ is exceeded earlier in the trajectory. In that case, the limiting trajectory is the "*" trajectory. Along the same lines, we argue that the "B" trajectory always is a limiting trajectory, since the equality $\phi_B<\phi^* \ (\phi_o)_B$ cannot be satisfied. This follows from the fact that

$$0^o<\phi^* < 90^o$$

and ϕ_B 90^o as ϕ_B is the supplement of ϕ_A.

Below some critical ship speed, the torpedo will not be turn rate limited. This speed is obtained when the trajectory is normal to the ships velocity vector, $\phi=90^o$, at a range of r = 3p.

Thus, from Eq. (106), we obtain

$$(3p)|\dot{\phi}|_{max} = (V_s)_{NL} \sin 90^{\circ}$$

yielding

$$(V_s)_{NL} = (3p)|\dot{\phi}|_{max} \tag{124}$$

Then introducing $p = V_T/(V_s)_{NL}$, we get

$$(V_s)_{NL} = [3V_T|\dot{\phi}|_{max}]^{\frac{1}{2}} \tag{125}$$

Furthermore, we see from Eq. (108) that for $\phi=90^{\circ}$

$$(K)_{NL} = 3p \tag{126}$$

Again, by probing Eq. (88) we can obtain the corresponding values of ϕ_o, designated $(\phi_o)_{NL}$, where the subscript "NL" is used to indicate the "no-limit" boundary point.

The computational procedure is based on:

1. Assuming a torpedo speed V = 35 kts.
2. Using an initial detection range (beginning of homing) r_o = 250 m.
3. Assuming the following maximum turn rates:

   a. 8 o/s b. 12 o/s c. 16 o/s

   d. 24 o/s e. 36 o/s f. 48 o/s
4. The following range of target speeds

   $0<V_s<25$ kts

The aim of the computation is to determine whether the limiting ϕ_o, and hence AOB, is governed by ϕ^* or by the turn rate at the range r = 3p.

The calculations are devided into two parts, and are performed on a TI 59 calculator.

For a given ship speed, Part I gives the sequential calculations of ϕ_A, K_A, ϕ_B, K_B, 0^* and K^* for each of the turn rates. The computer program is given in Appendix E.

Then, in Part II, the probe calculation for $(\phi_o)_A$, $(\phi_o)_B$, $(\phi_o)^* = (\phi_o)_{A,B,*}$ are performed. The program is given in Appendix E.

The limiting results are given on a polar plot, Fig. 41 with

$$(AOB)_{A,B,*} = 180^o - (\phi_o)_{A,B,*}$$

As seen from Fig. 41, for a target speed of 15 kts, we need AOB>85^o at ϕ_o for a maximum turn rate 16 o/s in order to have a hit at the first attack.

IX. CONCLUSIONS AND RECOMMENDATIONS

The detection performance of a passive homing torpedo used against shallow-draft surface ships operating in moderate sea states was investigated. Attention was focused on the effects of scattering from the randomly rough sea surface and scattering and absorption from the bubble-dominated inhomogeneous layer just below the sea surface. The effects of these two scattering mechanisms were separately estimated and their relative importance were compared.

The passive sonar equation was used to predict the performance of the homing system, and the detection range considering these two scattering effects was obtained and compared to the detection range based on a reference model. An idealized propagation model was used as reference of comparison. This reference model was based on a noise source model for a cavitating propeller, the operational characteristics for a square-law detector, and a transmission model associated with a homogeneous, unbounded medium.

Due to high frequency, moderate sea state and low grazing angles, the scattering from the randomly rough sea surface was found to be dominated by the direct path.

This result includes effects from geometrical shadowing.

The effect of scattering and absorption from the bubble-dominated, inhomogeneous subsurface layer was investigated using multiple scattering theory. Both the coherent and incoherent limits were investigated by incorporating the associated absorption coefficient into the transmission equation.

The effect on the sound speed from the bubble content was found to be negligible.

At the assumed depth setting of 6 m for the torpedo's search and attack phase, the scattering from the bubbles increased the transmission loss. This increase depended on the frequency and the wind speed.

Two operating frequencies were investigated, 60 kHz and 30 kHz. For both cases, bubbles significantly decreased the detection range.

For a torpedo system operating at the high frequencies, e.g., 60 kHz, the result indicates the inadvisability of using a searching and attack depth near the surface, i.e., z = 6 m.

For an operating frequency around 30 kHz, the calculated detection ranges is such that the turn rate requirements for a pursuit homing trajectory become excessive. For a maximum turn rate of 16 o/s, this limitation can be avoided

by adapting a tactical procedure where the angle on bow (AOB) at the beginning of the torpedo attack is greater than 85°.

At sea state 3, the results show a consistent and general trend towards the need for lower operating frequency in order to increase the detection range. An operating frequency below 30 kHz seems indicated.

Furthermore, a search depth below the bubble-dominated subsurface layer, i.e., $z>15-20$ m would result in an increased detection range.

To reduce the operational limitations induced by the scattering and absorption effects, a high maximum turn rate together with a variable speed capability, where $p \leq 2$ would be beneficial.

The result of this analysis has clearly demonstrated the importance of environmental factors on the torpedo capability, and is useful in giving insight into the behavior of a homing torpedo during its critical attack phase.

A valuable follow-on of this study would be an investigation of the effects of the bubble-dominated subsurface layer on target validation and pitch plane steering when the torpedo search depth is 50-60 m.

APPENDIX A

DETAILED OCEANOGRAPHIC BACKGROUND MATERIAL

A. GEOGRAPHIC DESCRIPTION

The Norwegian coastal waters constitute the eastern boundary of the Norwegian Sea. Although some general aspects related to the Norwegian Sea will be covered, this analysis will be concentrated on the Norwegian coastal waters above $68^{\circ}N$.

B. WIND

The northern region of the Norwegian Sea is affected by the Polar Easterlies and the southern region by the prevailing Westerlies. There are two dominant air masses which are relatively permanent:

-The Greenland high.

-The Iceland low.

These pressure systems produce storms which are carried across the Norwegian Sea in a belt from Iceland towards the Norwegian Coast causing steady precipitation and wind most of the year. The steep Norwegian Coast has a considerable influence on the winds and consequently also on the waves in the coastal waters. The main general modifications are that the streamlines tend to run parallel

to the coast and that wind and sea increases with distance from the sheltered coast into open ocean.

Strong local variation may occur. The most important of these are the marked local increase in wind speed in areas where the coast sharply changes direction. One such "corner effect," caused by the confluence of the streamlines, occurs near "Nordkapp" (North Cape). Also of importance are monsoonal effects due to the different heat capacities between the ocean and the continent. Drainage of cold air from the inland valleys in the wintertime causes a marked increase in the wind speed in several areas along the coast. Most of these coastal effects are significantly dissipated at distances of approximately 50 nmi. from the coast. The fact that the wind tends to blow along the coast is clearly demonstrated in Figs. 12 and 13 which include data from weather stations from "Hillesöy" to "Ona" and "Myken" to "Furuholmen" respectively. The high frequency of offshore winds is caused by the drainage of cold air from the inland valleys during winter time. That this phenomenon is closely connected to the coast is illustrated by the fact that it is missing at weather station "Skomvaer" situated approximately 50 nmi. off the main coast. A frequency distribution of observed wind speeds along the coast, obtained from Ref. 1, is presented in Table V. A summary of this table follows:

TABLE V

FREQUENCY DISTRIBUTION OF WIND SPEED IN PERCENT PER YEAR AT WEATHER STATIONS ALONG THE NORWEGIAN COAST

m/sec	0-7	8-13	14-20	$\geqq$21	
Beaufort	0-4	5+6	7+8	$\geqq$9	
Ferder	67	28	5	0.1	
Lyngor	79	19	2	0.2	
Lista	67	28	5	0.2	
Utsira	73	22	5	0.3	
Hellisöy	77	19	4	0.2	
Krakenes	58	28	11	2.7	Jan-Dec 1949-1975
Ona	70	22	7	0.7	
Sula	61	30	8	1.1	
Nordoyan	49	35	14	1.9	
Myken	64	26	9	1.2	
Skomvær	58	31	10	0.9	
Andenes	79	18	3	0.1	
Torsvar	72	23	5	0.4	
Fruholmen	54	32	12	1.8	
Vardo	75	22	3	0.1	
Biornoya	63	31	6	0.4	1956-1975
Polarfront	46	30	14	1.4	

The highest winds are reported from the areas between 62^{O}N and 68^{O}N. The frequency of high winds in this area are significantly greater than those found at stations to the south of 62^{O}N and also to the north of 68^{O}N. The wind condition around North Cape, are very severe. This area can be compared with the other coastal area of high wind speed such as "Stadt" (represented by the weather station, "Krakenes"). In these areas the frequency of storms is greater than at "Polarfront" situated in the open Norwegian Sea.

C. WAVES

Frequency distribution of significant wave heights are represented in Table VI.

The station north of 68^{O}N is characterized by comparatively small frequency of high waves. Even at "Furuholmen" where wind conditions are very severe, the frequency distribution of significant wave heights is similar to more sheltered areas like "Utsira."

The seasonal variation for the area of interest around 70^{O}N is given in Figs. 3 and 4. The average monthly distribution of significant wave heights for a typical station like "Andenes" is given in Fig. 3 and Fig. 4 gives the yearly distribution for this station.

TABLE VI

FREQUENCY DISTRIBUTION OF SIGNIFICANT WAVE HEIGHT IN PERCENT AT THE WEATHER STATION "ANDENES"

STATION: Andenes YEARS: 1949-1972

SS	0+1+2	3	4	5	6	7	8	9	
H_S	0 - 0.4	0.5 - 1.2	1.3 - 2.4	2.5 - 3.9	4.0 5.9	6.0 - 8.9	9.0- 13.9	13.9	N
JAN	15.3	26.9	33.3	15.5	6.6	2.3	0.18	0.00	2542
FEB	17.7	28.7	31.3	14.2	5.9	2.0	0.14	0.00	2295
MAR	18.1	28.9	30.8	14.3	5.8	1.9	0.17	0.00	2529
APR	24.5	33.1	27.4	10.8	3.4	0.8	0.04		2293
MAY	30.9	35.5	23.9	7.7	1.7	0.3	0.01		1720
JUN	37.4	36.9	20.2	4.8	0.6	0.1	0.00		1565
JUL	42.6	36.2	17.1	3.7	0.4	0.0	0.00		1618
AUG	40.6	36.4	18.0	4.3	0.5	0.1			1621
SEP	29.7	34.3	24.4	8.9	2.1	0.5	0.01		2301
OCT	21.8	31.3	29.4	12.4	4.1	1.0	0.01		2374
NOV	21.7	31.5	29.9	11.7	4.1	1.1	0.06		2303
DEC	18.5	30.1	32.2	13.2	4.7	1.2	0.09		2379
YEAR	26.6	32.5	26.5	10.1	3.3	0.9	0.06	0.00	

N = Number of Observations
SS = Class Interval, State of Sea
H_S = Significant Wave Height

D. AMBIENT NOISE

Due to the fact that the Norwegian Sea is physically separated from the Atlantic by the Faeröy-Shetland-Iceland ridge, and from the Greenland Sea by the Jan Mayan ridge, little long distance shipping noise is transferred into the area. This, combined with relatively low shipping traffic in the central and northern parts of the Norwegian Sea, produces a relatively low ambient noise level for the frequency band $100<f<1000$ Hz, especially when noise from marine life is not included. Further, in the absence of nearby shipping and marine life, the ambient noise level in the frequency band $1<f<50$ kHz is, according to Ref. 4, dominated by the wind.

A typical area for the central part of the Norwegian Sea can be represented by the weather station "Polarfront" at 66°N, 2°E. Reference 1 shows that there is approximately a 15% chance of finding wind forces of Beaufort>6. These effects predict a moderate ambient noise level in the frequency range 100 Hz-50 kHz for the central and northern regions of the Norwegian Sea.

The shallow coastal Norwegian waters are, according to Ref. 4, typically 5-10 dB noisier than the corresponding deep waters. However, great variability caused by local traffic, fishing fleet activity, marine life, and local wind conditions makes ambient noise level prediction

difficult in these areas. This means that accurate ambient noise level determinations have to be made on the spot, as it is both site and time dependent.

A noticeable influence on the ambient noise level is rain, which is a year around feature along the Norwegian coast. As seen from Fig. 8, taken from Ref. 4, rain has a tendency to produce a constant high ambient noise level over a large frequency range, thus dominating other effects. Furthermore, for the upper frequency of interest, i.e., around 60 kHz the lower bound for the ambient noise is determined by the thermal agitation, see Fig. 8.

In determining the figure of merit (FOM) for a passive sonar system, the noise level will be the larger of either the self noise or the ambient noise. For a torpedo the self noise will typically be dominant.

E. SOUND SPEED PROFILES

Again, concentrate on data relevant to Norwegian coastal waters. According to Ref. 6, which covers the southern part of the Norwegian coast, low sound speeds are common because of the influence of water from the Baltic Sea combined with fresh water drainage from the fjords. Furthermore, great variability, both seasonal and within seasons, is encountered. Figure 9 obtained from Ref. 5 gives a picture of the sound speed profiles

for the northern Norwegian coast. Again, large variations are common. Noticeable in both sets of data is a typical seasonal pattern of strong cooling of the surface layer during winter and a similarly strong heating during summer. Furthermore, note that the minimum and maximum are relatively shallow, i.e., less than 50 m.

Also characteristic is the influence of the cold and fresh melt waters drained out through the fjord-arms during spring and summer.

To illustrate the sonar problems associated with these sound speed profiles, ray paths for the extremes of Fig. 9 are shown in Figs. 10 and 11, where the source is 3 m below the sea surface.

APPENDIX B

SURFACE SCATTERING TI 59 PROGRAM

A. INTRODUCTION

This program gives specular scattered power at the receiver versus incoming power at the randomly rough surface in the high frequency limit according to Eq. (70).

Shadowing of surface areas by other parts of the boundary are taken into account by the bistatic shadowing function $S(\theta)$.

Furthermore, the program gives the effect of the randomly rough surface compared to the idealized free-field condition as expressed in Eq. (80). The results of these calculations is given in Fig. 27.

B. PROGRAM STEPS

A block-diagram of the computer program is given in Fig. 26.

The program uses the partitioning ratio of program to data space according to code 4 OP17. The users instructions are as follows:

Procedure	Enter	Press	Display
Enter data	Detection range	2nd A	R_D[1]
Enter data	Source depth	R/S	h_s[1]
Enter data	Receiver depth	R/S	h_r[1]
Enter data	Beam width	R/S	ϕ[1]
Enter data	Wind speed	R/S	w[1]
Calculate θ, R_1, R_2, A	--	2nd B	A (θ, R_1, R_2, A)[1]
Calculate $<\zeta^{12}>$	--	2nd C	$<\zeta^{12}>$[1]
Calculate v	--	2nd D	v[1]
Calculate erfc v	--	A	erfc v[1]
Calculate $S(\theta)$	--	B	$S(\theta)$[1]
Calculate $\frac{<s^2>}{<p_1 p_1^*>}$	--	C	$\frac{<s^2>}{<p_1 p_1^*>}$[1]
Calculate ΔIL	--	D	ΔIL[1]

[1]These values are printed automatically if the calculator is connected to the PC-100A Print Cradle.

For the error function complement we have

$$\mathrm{erfc}(v) = \frac{2}{\sqrt{\pi}} \int_v^\infty e^{-\alpha^2} d\alpha$$

in contrast to the normal distribution

$$Q(u) = \frac{1}{\sqrt{2\pi}} \int_\alpha^\infty e^{-t^2/2} dt$$

However, there is a linear relationship between the two functions.

The numerical equation used to calculate the erfc(v) is a modified program from Texas Instruments [Ref. 24].

$$\mathrm{erfc}(v) = Z(v)\,[b_1\alpha+b_2\alpha^2+b_3\alpha^3+b_4\alpha^4+b_5\alpha^5]$$

where

$$\alpha = \frac{1}{1+\rho v}$$

$p = .231649$

$b_1 = .451673691$

$b_2 = -.504257336$

$b_3 = 2.51939026$

$b_4 = -2.563346623$

$b_5 = 1.881292139$

The program steps are listed below, giving location (LOC), code (COD), key symbol (KEY), and comments.

000	76	LBL
001	16	A'
002	42	ST
003	00	00
004	99	PRT
005	91	R/S
006	42	STO
007	01	01
008	99	PRT
009	91	R/S
010	42	STO
011	02	02
012	99	PRT
013	91	R/S
014	42	STO
015	03	03
016	99	PRT
017	91	R/S
018	42	STO
019	04	04
020	99	PRT
021	91	R/S
022	76	LBL
023	17	B'
024	53	(
025	53	(
026	43	RCL
027	00	00
028	65	x
029	43	RCL
030	02	02
031	54	)
032	55	÷
033	53	(
034	43	RCL
035	01	01
036	85	+
037	43	RCL
038	02	02
039	54	)
040	54	)
041	42	STO
042	05	05
043	53	(
044	53	(
045	43	RCL
046	05	05
047	55	÷
048	43	RCL
049	02	02
050	54	)
051	22	INV
052	30	TAN
053	54	)
054	42	STO
055	06	06
056	99	PRT
057	53	(
058	53	(
059	43	RCL
060	05	05
061	55	÷
062	53	(
063	43	RCL
064	06	06
065	38	SIN
066	54	)
067	54	)
068	42	STO

069	07	07
070	99	PRT
071	53	(
072	53	(
073	43	RCL
074	00	00
075	75	-
076	43	RCL
077	05	05
078	54	)
079	55	÷
080	53	(
081	43	RCL
082	06	06
083	38	SIN
084	54	)
085	54	)
086	42	STO
087	08	08
088	99	PRT
089	53	(
090	43	RCL
091	07	07
092	85	+
093	43	RCL
094	08	08
095	54	)
096	42	STO
097	09	09
098	25	CLR
099	69	OP
100	00	00
101	01	1
102	03	3
103	03	3
104	05	5
105	01	1
106	07	7
107	01	1
108	03	3
109	69	OP
110	04	04
111	53	(
112	53	(
113	89	π
114	65	x
115	43	RCL
116	08	08
117	54	)
118	65	x
119	53	(
120	43	RCL
121	03	03
122	38	SIN
123	65	x
124	43	RCL
125	07	07
126	54	)
127	54	)
128	42	STO
129	10	10
130	69	OP
131	06	06
132	91	R/S
133	76	LBL
134	18	C'
135	25	CLR
136	69	OP
137	00	00
138	00	00
139	06	6
140	02	2
141	07	7
142	03	3
143	02	2
144	03	3
145	03	3
146	69	OP
147	04	04
148	53	(
149	53	(
150	53	(
151	43	RCL
152	04	04
153	65	x
154	05	5
155	93	.
156	01	1
157	02	2
158	54	)
159	85	+
160	03	3
161	54	)
162	65	x
163	93	.
164	00	0
165	00	0
166	01	1
167	54	)
168	50	lxl
169	42	STO
170	11	11
171	69	OP
172	06	06
173	91	R/S
174	76	LBL
175	19	D'
176	53	(
177	43	RCL
178	06	06
179	30	TAN
180	35	1/x
181	54	)
182	42	STO
183	12	12
184	53	(
185	43	RCL
186	12	12
187	55	÷
188	53	(
189	53	(
190	02	2
191	65	x
192	43	RCL
193	11	11
194	54	)
195	34	$\sqrt{x}$
196	54	)
197	54	)
198	42	STO
199	13	13
200	99	PRT
201	91	R/S
202	76	LBL
203	11	A
204	53	(
205	53	(
206	53	(
207	53	(
208	43	RCL
209	13	13
210	33	x^2
211	54	(
212	55	÷
213	02	2
214	54	)
215	94	+/-
216	22	INV
217	23	LNX
218	54	)
219	65	x
220	53	(
221	53	(

222	89	π
223	34	$\sqrt{x}$
224	65	x
225	02	2
226	54	)
227	35	1/X
228	54	)
229	54	)
230	42	STO
231	14	14
232	53	(
233	53	(
234	53	(
235	53	(
236	43	RCL
237	13	13
238	65	x
239	93	.
240	02	2
241	03	3
242	01	1
243	06	6
244	04	4
245	01	1
246	09	9
247	86	+
248	01	1
249	54	)
250	35	1/x
251	54	)
252	42	STO
253	15	15
254	53	(
255	53	(
256	43	RCL
257	14	14
258	65	x
259	01	1
260	93	.
261	08	8
262	01	1
263	54	)
264	65	x
265	53	(
266	43	RCL
267	15	15
268	65	x
269	93	.
270	03	3
271	01	1
272	09	9
273	03	3
274	08	8
275	01	1
276	05	5
277	03	3
278	75	-
279	93	.
280	03	3
281	05	5
282	06	6
283	05	5
284	06	6
285	03	3
286	07	7
287	08	8
288	02	2
289	65	x
290	43	RCL
291	15	15
292	33	x^2
293	85	+
294	01	1
295	93	.
296	97	7
297	08	8
298	01	1
299	04	4
300	07	7
301	07	7
302	09	9
303	03	3
304	07	7
305	65	x
306	43	RCL
307	15	15
308	45	Y^x
309	03	3
310	75	-
311	01	1
312	93	.
313	08	8
314	02	2
315	01	1
316	02	2
317	05	5
318	05	5
319	09	9
320	07	7
321	08	8
322	00	0
323	65	x
324	43	RCL
325	15	15
326	45	Y^x
327	04	4
328	85	+
329	01	1
330	93	.
331	03	3
332	03	3
333	00	0
334	02	2
335	07	7
336	04	4
337	04	4
338	02	2
339	09	9
340	00	0
341	65	x
342	43	RCL
343	15	15
344	45	Y^x
345	05	5
346	54	)
347	54	)
348	42	STO
349	16	16
350	99	PRT
351	91	R/S
352	76	LBL
353	12	B
354	53	(
355	53	(
356	53	(
357	43	RCL
358	13	13
359	33	x^2
360	94	+/-
361	22	INV
362	23	LNX
363	54	)
364	75	-
365	53	(
366	89	π
367	34	$\sqrt{x}$
368	65	x
369	43	RCL
370	13	13
371	65	x
372	43	RCL
373	16	16
374	54	)

```
375  54 )
376  55 ÷
377  53 (
378  89 π
379  34 √x
380  65 x
381  04 4
382  65 x
383  43 RCL
384  13 13
385  54 )
386  54 )
387  42 STO
388  17 17
389  53 (
390  53 (
391  53 (
392  01 1
393  75 -
394  53 (
395  53 (
396  53 (
397  43 RCL
398  17 17
399  65 x
400  04 4
401  54 )
402  94 +/-
403  54 )
404  22 INV
405  23 LNX
406  54 )
407  54 )
408  65 x
409  53 (
410  01 1
411  75 -
412  43 RCL
413  16 16
414  54 )
415  54 )
416  55 ÷
417  53 (
418  43 RCL
419  17 17
420  65 x
421  04 4
422  54 )
423  54 )
424  42 STO
425  18 18
426  99 PRT
427  91 R/S
428  76 LBL
429  13 C
430  25 CLR
431  69 OP
432  00 00
433  03 3
434  06 6
435  01 1
436  05 5
437  01 1
438  03 3
439  03 3
440  07 7
441  69 OP
442  04 04
443  53 (
444  53 (
445  43 RCL
446  10 10
447  65 x
448  43 RCL
449  18 18
450  54 )
451  55 ÷
452  53 (
453  53 (
454  53 (
455  53 (
456  43 RCL
457  07 07
458  33 x²
459  54 )
460  65 x
461  08 8
462  54 )
463  65 x
464  89 π
465  54 )
466  65 x
467  43 RCL
468  11 11
469  54 )
470  54 )
471  42 STO
472  19 19
473  69 OP
474  06 06
475  91 R/S
476  76 LBL
477  14 D
478  25 CLR
479  69 OP
480  00 00
481  01 1
482  06 6
483  01 1
484  04 4
485  69 OP
486  04 04
487  53 (
488  53 (
489  43 RCL
490  19 19
491  28 LOG
492  54 )
493  65 x
494  01 1
495  00 0
496  54 )
497  42 STO
498  20 20
499  69 OP
500  06 06
501  91 R/S
```

APPENDIX C

BUBBLE DYNAMICS TI 59 PROGRAM

A. INTRODUCTION

This program gives the resonant frequency f_r and the damping constant δ for bubbles according to Eq. (92). Furthermore, the program gives scattering cross section σ_s, extinction cross section σ_e, and absorption cross section σ_a as a function of bubble radius a, incoming frequency f, and depth z. The results of the calculations are given in Figs. 31 and 32.

B. PROGRAM STEPS

The user's instructions are as follows:

Procedure	Enter	Press	Display
Enter data	Bubble Radius	2nd A	a[1]
Enter data	Incoming Frequency	R/S	f[1]
Enter data	Depth	R/S	z[1]
Calculate X	--	2nd B	X[1]
Calculate coshX and sinhX	--	2nd C	coshX[1] sinhX[1]
Calculate d/b	--	2nd D	d/b[1]
Calculate b	--	2nd E	b[1]
Calculate β	--	A	β[1]
Calculate f_r	--	B	f_r[1]
Calculate δ	--	C	δ[1]
Calculate σ	--	D	σ_e[1]
Calculate σ_s and σ_a	--	E	σ_s[1] σ_a[1]

[1]These values are printed automatically if the calculator is connected to PC-100A Print Cradle.

The program steps are listed below giving location (LOC), code (COD), key (KEY) and comments.

000	76	LBL
001	16	A'
002	42	STO
003	11	11
004	99	PRT
005	91	R/S
006	42	STO
007	12	12
008	99	PRT
009	91	R/S
010	42	STO
011	13	13
012	99	PRT
013	91	R/S
014	76	LBL
015	17	B'
016	53	(
017	53	(
018	53	(
019	53	(
020	53	(
021	53	(
022	04	4
023	65	x
024	89	π
025	54	)
026	65	x
027	43	RCL
028	12	12
029	54	)
030	65	x
031	53	(
032	53	(
033	93	.
034	00	0
035	00	0
036	00	0
037	00	0
038	00	0
039	00	0
040	01	0
041	09	9
042	01	1
043	55	÷
044	43	RCL
045	11	11
046	54	)
047	85	+
048	93	.
049	00	0
050	00	0
051	01	1
052	02	2
053	09	9
054	65	x
055	53	(
056	01	1
057	85	+
058	93	.
059	01	1
060	65	x
061	43	RCL
062	13	13
063	54	)
064	54	)
065	54	)
066	65	x
067	93	
068	02	2
069	04	4
070	54	)
071	55	÷
072	93	.
073	00	0
074	00	0
075	00	0
076	00	0
077	05	5
078	06	6
079	54	)
080	34	$\sqrt{x}$
081	65	x
082	43	RCL
083	11	11
084	54	)
085	42	STO
086	01	01
087	99	PRT
088	91	R/S
089	76	LBL
090	18	C'
091	53	(
092	53	(
093	43	RCL
094	01	01
095	22	INV
096	23	LNX
097	85	+
098	43	RCL
099	01	01
100	94	X/-
101	22	INV
102	23	LNX
103	54	)
104	55	÷
105	02	2
106	54	)
107	42	STO
108	02	02
109	99	PRT
110	53	(
111	53	(
112	43	RCL
113	01	01
114	22	INV
115	23	LNX
116	75	-
117	43	RCL
118	01	01
119	94	+/-
120	22	INV
121	23	LNX
122	54	)
123	55	÷
124	02	2
125	54	)
126	42	STO
127	03	03
128	99	PRT

129	91	R/S
130	76	LBL
131	17	D'
132	53	(
133	53	(
134	53	(
135	53	(
136	43	RCL
137	01	01
138	65	x
139	53	(
140	43	RCL
141	03	03
142	85	+
143	43	RCL
144	01	01
145	38	SIN
146	54	)
147	54	)
148	75	-
149	02	2
150	65	x
151	53	(
152	43	RCL
153	02	02
154	75	-
155	43	RCL
156	01	01
157	39	COS
158	54	)
159	54	)
160	55	÷
161	53	(
162	53	(
163	53	(
164	43	RCL
165	01	01
166	33	X^2
167	54	)
168	65	x
169	53	(
170	43	RCL
171	02	02
172	75	-
173	43	RCL
174	01	01
175	39	COS
176	54	)
177	54	)
178	85	+
179	53	(
180	53	(
181	01	1
182	93	.
183	02	2
184	65	x
185	43	RCL
186	01	01
187	54	)
188	65	x
189	53	(
190	43	RCL
191	03	03
192	75	-
193	43	RCL
194	01	01
195	38	SIN
196	54	)
197	54	)
198	54	)
199	54	)
200	65	x
201	01	1
202	93	.
203	02	2
204	54	)
205	42	STO
206	04	04
207	99	PRT
208	91	R/S
209	76	LBL
210	10	E
211	53	(
212	53	(
213	53	(
214	53	(
215	53	(
216	03	3
217	93	.
218	02	2
219	55	÷
220	43	RCL
221	01	01
222	54	)
223	65	x
224	53	(
225	43	RCL
226	03	03
227	75	-
228	43	RCL
229	01	01
230	38	SIN
231	54	)
232	54	)
233	55	÷
234	53	(
235	43	RCL
236	02	02
237	75	-
238	43	RCL
239	01	01
240	39	COS
241	54	)
242	54	)
243	85	+
244	01	1
245	54	)
246	35	1/x
247	65	x
248	53	(
249	54	(
250	43	RCL
251	04	04
252	33	x^2
253	54	)
254	85	+
255	01	1
256	54	)
257	35	1/x
258	54	)
259	42	STO
260	05	05
261	99	PRT
262	91	R/S
263	76	LBL
264	11	A
265	53	(
266	53	(
267	53	(
268	01	1
269	05	5
270	00	0
271	55	÷
272	53	(
273	01	1
274	00	0
275	01	1
276	03	3
277	00	0
278	00	0
279	00	0
280	65	x
281	43	RCL

282	11	11
283	65	x
284	53	(
285	01	1
286	85	+
287	93	.
288	01	1
289	65	x
290	43	RCL
291	13	13
292	54	)
293	54	)
294	54	)
295	65	x
296	53	)
297	01	1
298	75	-
299	53	(
300	53	(
301	04	4
302	93	.
303	02	2
304	65	x
305	43	RCL
306	05	05
307	54	)
308	35	1/x
309	54	)
310	54	)
311	54	)
312	85	+
313	01	1
314	54	)
315	42	STO
316	06	06
317	99	PRT
318	91	R/S
319	76	LBL
320	12	B
321	53	(
322	53	(
323	53	(
324	53	(
325	04	4
326	93	.
327	02	2
328	65	x
329	43	RCL
330	05	05
331	65	x
332	43	RCL
333	06	06
334	65	x
335	01	1
336	00	0
337	01	1
338	03	3
339	00	0
340	00	0
341	00	0
342	54	)
343	65	x
344	53	(
345	01	1
346	85	+
347	93	.
348	01	1
349	65	x
350	43	RCL
351	13	13
352	52	)
353	54	)
354	55	÷
355	01	1
356	93	.
357	00	0
358	02	2
359	06	6
360	54	)
361	50	1x1
362	34	$\sqrt{x}$
363	65	x
364	53	(
365	53	(
366	89	π
367	65	x
368	02	2
369	65	x
370	43	RCL
371	11	11
372	54	)
373	35	1/x
374	54	)
375	54	)
376	42	STO
377	07	07
378	99	PRT
379	91	R/S
380	76	LBL
381	13	C
382	53	(
383	53	(
384	53	(
385	93	.
386	00	0
387	00	0
388	00	0
389	00	0
390	04	4
391	01	1
392	08	8
393	08	8
394	07	7
395	09	9
396	65	x
397	43	RCL
398	12	12
399	65	x
400	43	RCL
401	11	11
402	54	)
403	85	+
404	53	(
405	43	RCL
406	04	04
407	65	x
408	53	(
409	53	(
410	43	RCL
411	07	07
412	55	÷
413	43	RCL
414	12	12
415	54	)
416	33	x^2
417	54	)
418	54	)
419	54	)
420	85	+
421	53	(
422	93	=
423	00	0
424	00	0
425	06	6
426	02	2
427	00	0
428	05	5
429	55	÷
430	53	(
431	43	RCL
432	12	12
433	65	x
434	53	(

435	43	RCL
436	11	11
437	33	x^2
438	54	)
439	54	)
440	54	)
441	54	)
442	42	STO
443	08	08
444	99	PRT
445	91	R/S
446	76	LBL
447	14	D
448	53	(
449	53	(
450	04	4
451	65	x
452	89	π
453	65	x
454	43	RCL
455	11	11
456	54	)
457	65	x
458	53	(
459	53	(
460	43	RCL
461	08	08
462	65	x
463	01	1
464	05	5
465	00	0
466	00	0
467	00	0
468	00	0
469	55	÷
470	53	(
471	89	π
472	65	x
473	02	2
474	65	x
475	43	RCL
476	12	12
477	54	)
478	54	)
479	54	)
480	55	÷
481	53	(
482	53	(
483	53	(
484	53	(
485	53	(
486	43	RCL
487	07	07
488	55	÷
489	43	RCL
490	12	12
491	54	)
492	33	x^2
493	54	)
494	75	-
495	01	1
496	54	)
497	33	x^2
498	54	)
499	85	+
500	53	(
501	43	RCL
502	08	08
503	33	x^2
504	54	)
505	54	)
506	54	)
507	42	STO
508	09	09
509	99	PRT
510	91	R/S
511	76	LBL
512	15	E
513	53	(
514	53	(
515	04	4
516	65	x
517	89	π
518	65	x
519	53	(
520	43	RCL
521	11	11
522	33	x^2
523	54	)
524	54	)
525	55	÷
526	53	(
527	53	(
528	53	(
529	53	(
530	53	(
531	43	RCL
532	07	07
533	55	÷
534	43	RCL
535	12	12
536	54	)
537	33	x^2
538	54	)
539	75	-
540	01	1
541	54	)
542	33	X^2
543	53	)
544	85	+
545	53	(
546	43	RCL
547	08	08
548	33	x^2
549	54	)
550	54	)
551	54	)
552	42	STO
553	10	10
554	99	PRT
555	66	PAU
556	53	(
557	43	RCL
558	09	09
559	75	-
560	43	RCL
561	10	10
562	54	)
563	42	STO
564	11	11
565	99	PRT
566	91	R/S

APPENDIX D

NUMERICAL INTEGRATION TI 59 PROGRAM

A. INTRODUCTION

In order to perform the numerical integration of $\sigma n(a)da$, a standard Texas Instrument's program was used [Ref. 25]. This program performs the integration by using Simpson's discrete approximation based on the following expression

$$I = \int_{x_o}^{x_n} f(x)dx \simeq \frac{h}{3}(f_o+4f_1+2f_2+4f_3+2f_4+\ldots+2f_{n-2}+4f_{n-1}+f_n)$$

where

$f(x)$ must be known at $n+1$ equally spaced points $(f_o - f_n)$.

$$h = \frac{x_n - x_o}{n} \; ; \; x_n > x_o$$

$n+7 \leq$ number of data registers available

n = number of subintervals = 2, 4, 6, ...

B. PROGRAM INSTRUCTIONS

The program is taken from the master library program package by using the code 2nd Pgm 10 on the calculator.

The user's instructions are as follows

Procedure	Enter	Press	Display
Enter data	Subintervals	A	n[1]
Enter data	h	B	h[1]
Enter data	Function values		
	0	C	0
	f_o	R/S	f_o[1]
	f_1	R/S	f_1[1]
	.	.	
	.	.	
	.	.	
	f_n	R/S	f_n[1]
Calculate	-	D	I[1]

[1]These values are printed automatically if the calculator is connected to PC-100A Print Cradle.

The program steps are listed below giving location (LOC), key symbol (KEY), and comments.

000	76	LBL
001	11	A
002	53	(
003	50	lxl
004	42	STO
005	05	05
006	55	÷
007	02	2
008	54	)
009	42	STO
010	02	02
011	22	INV
012	59	INT
013	29	CP
014	22	INV
015	67	EQ
016	52	EE
017	43	RCL
018	05	05
019	99	PRT
020	92	RTN
021	76	LBL
022	52	EE
023	00	0
024	35	1/x
025	92	RTN
026	76	LBL
027	12	B
028	42	STO
029	03	03
030	99	PRT
031	92	RTN
032	76	LBL
033	13	C
034	53	(
035	24	CE
036	85	+
037	32	$x \gtrless t$
038	06	6
039	54	)
040	42	STO
041	01	01
042	32	$x \gtrless t$
043	98	ADV
044	92	RTN
045	76	LBL
046	50	lxl
047	76	ST*
048	01	01
049	32	$x \gtrless t$
050	01	1
051	44	SUM
052	01	01
053	32	$x \gtrless t$
054	99	PRT
055	92	RTN
056	61	GTO

```
057  50 |x|
058  76 LBL
059  14 D
060  53 (
061  43 RCL
062  05 05
063  85 +
064  06 6
065  54 )
066  42 STO
067  01 01
068  73 RC*
069  01 01
070  42 STO
071  04 04
072  76 LBL
073  45 y^x
074  01 1
075  22 INV
076  44 SUM
077  01 01
078  53 (
079  73 RC*
080  01 01
081  65 x
082  04 4
083  54 )
084  44 SUM
085  04 04
086  01 1
087  22 INV
088  44 SUM
089  01 01
090  22 INV
091  97 DSZ
092  02 02
093  33 x^2
094  53 (
095  73 RC*
096  01 01
097  65 x
098  02 2
099  54 )
100  44 SUM
101  04 04
102  61 GTO
103  45 y^x
104  76 LBL
105  33 x^2
106  73 RC*
107  01 01
108  44 SUM
109  04 04
110  53 (
111  43 RCL
112  03 03
113  55 ÷
114  03 3
115  54 )
116  49 PRD
117  04 04
118  43 RCL
119  04 04
120  98 ADV
121  99 PRT
122  92 RTN
```

APPENDIX E

TURN RATE LIMITATION TI 59 PROGRAMS

A. INTRODUCTION

The turn rate limitation calculations are divided into two parts with separate programs.

B. PART I PROGRAM

For a given initial detection range and a given ship speed, Part I performs a sequential calculation of $\phi_A, K_A, \phi_B, K_B, \phi^*$ and K^* for each of the maximum turn rates investigated, together with the "no limit" conditions $(V_s)_{NL}$ and K_{NL} based on

$$\phi_A = \sin^{-1} \left(\frac{3p|\dot{\phi}|max}{V_s}\right.; \lesssim 90^o$$

$$\phi_B = 180^o - \phi_A$$

$$K_{A,B} = \frac{V_s(1+\cos\phi_{A,B})^P}{|\dot{\phi}|_{max}(\sin\phi_{A,B})^{P-2}}$$

$$\phi^* = \cos^{-1}(P-2)$$

$$K^* = \frac{V_s(1+P/2)^P[1-(P/2)^2]^{1-P/2}}{|\dot{\phi}|_{max}}$$

$$(V_s)_{NL} = (3V_T|\dot{\phi}|_{max})^{\frac{1}{2}}$$

$$K_{NL} = 3p$$

For p>2, the solution for * and K* are not valid. Furthermore, for V_s $(V_s)_{NL}$ no solutions are valid for any of the quantities.

The program is based on the fixed torpedo speed of V_T = 35 kts (18 m/s) and an initial detection range of T_o = = R_D = 250 m.

The user instructions for the program are as follows:

Prodcedure	Enter	Press	Display
Enter data	Maximum Turn Rate	A	$\lvert\phi\rvert_{max}$ [1]
Enter data	Ship speed	B	V_T [1]
Calculate ϕ* and K*	--	C	ϕ*,K* [1]
Calculate ϕ_A and ϕ_B	--	D	ϕ_A, ϕ_B [1]
Calculate K_A and K_B	--	E	K_A,K_B [1]

[1]These values are printed automatically if the calculator is connected to PC-100A Print Cradle.

A listing of the program steps follows giving location (LOC), code (COD), key symbol (KEY), and comments.

000	76	LBL
001	11	A
002	42	STO
003	01	01
004	99	PRT
005	91	R/S
006	76	LBL
007	12	B
008	42	STO
009	02	02
010	99	PRT
011	25	CLR
012	69	OP
013	00	00
014	03	3
015	03	3
016	69	OP
017	04	04
018	53	(
019	01	1
020	08	8
021	55	÷
022	43	RCL
023	02	02
024	54	)
025	42	STO
026	03	03
027	69	OP
028	06	06
029	25	CLR
030	69	OP
031	00	00
032	02	2
033	06	6
034	03	3
035	01	1

036	02	2
037	07	7
038	69	OP
039	04	04
040	53	(
041	43	RCL
042	03	03
043	65	x
044	03	3
045	54	)
046	42	STO
047	10	10
048	69	OP
049	06	06
050	25	CLR
051	69	OP
052	00	00
053	04	4
054	02	2
055	03	3
056	06	6
057	03	3
058	01	1
059	02	2
060	07	7
061	69	OP
062	04	04
063	53	(
064	53	(
065	53	(
066	03	3
067	65	x
068	01	1
069	08	8
070	54	)
071	65	x
072	43	RCL
073	01	01
074	54	)
075	34	$\sqrt{x}$
076	54	)
077	42	STO
078	11	11
079	69	OP
080	06	06
081	91	R/S
082	76	LBL
083	13	C
084	25	CLR
085	69	OP
086	00	00
087	03	3
088	03	3
089	02	2
090	03	3
091	05	5
092	01	1
093	69	OP
094	04	04
095	53	(
096	53	(
097	53	(
098	43	RCL
099	03	03
100	55	÷
101	02	2
102	54	)
103	22	INV
104	39	COS
105	54	)
106	54	)
107	42	STO
108	04	04
109	69	OP
110	06	06
111	25	CLR
112	69	OP
113	00	00
114	02	2
115	06	6
116	05	5
117	01	1
118	69	OP
119	04	04
120	53	(
121	53	(
122	53	(
123	53	(
124	43	RCL
125	02	02
126	65	x
127	53	(
128	53	(
129	01	1
130	85	+
131	53	(
132	43	RCL
133	03	03
134	55	÷
135	02	2
136	54	)
137	54	)
138	45	y^x
139	43	RCL
140	03	03
141	54	)
142	54	)
143	65	x
144	53	(
145	53	(
146	01	1
147	75	-
148	53	(
149	53	(
150	43	RCL
151	03	03
152	55	÷
153	02	2
154	54	)
155	33	x^2
156	54	)
157	54	)
158	45	y^x
159	53	(
160	01	1
161	75	-
162	53	(
163	43	RCL
164	03	03
165	55	÷
166	02	2
167	54	)
168	54	)
169	54	)
170	54	)
171	55	÷
172	43	RCL
173	01	01
174	54	)
175	42	STO
176	05	05
177	69	OP
178	06	06
179	91	R/S
180	76	LBL
181	14	D
182	25	CLR
183	69	OP
184	00	00
185	03	3
186	03	3
187	02	2
188	03	3

189	01	1
190	03	3
191	69	OP
192	04	04
193	53	(
194	53	(
195	53	(
196	53	(
197	53	(
198	43	RCL
199	03	03
200	65	x
201	03	3
202	54	)
203	65	x
204	43	RCL
205	01	01
206	54	)
207	55	÷
208	43	RCL
209	02	02
210	54	)
211	22	INV
212	38	SIN
213	54	)
214	42	STO
215	06	06
216	69	OP
217	06	06
218	25	CLR
219	69	OP
220	00	00
221	03	3
222	03	3
223	02	2
224	03	3
225	01	1
226	04	4
227	69	OP
228	04	04
229	53	(
230	01	1
231	08	8
232	00	0
233	75	-
234	43	RCL
235	06	06
236	54	)
237	42	STO
238	07	07
239	69	OP
240	06	06
241	91	R/S
242	76	LBL
243	15	E
244	25	CLR
245	69	OP
246	00	00
247	02	2
248	06	6
249	01	1
250	03	3
251	69	OP
252	04	04
253	53	(
254	53	(
255	43	RCL
256	02	02
257	65	x
258	53	(
259	53	(
260	01	1
261	85	+
262	53	(
263	43	RCL
264	06	06
265	39	COS
266	54	)
267	54	)
268	45	y^x
269	43	RCL
270	03	03
271	54	)
272	54	)
273	55	÷
274	53	(
275	43	RCL
276	01	01
277	65	x
278	53	(
279	53	(
280	43	RCL
281	06	06
282	38	SIN
283	54	)
284	45	y^x
285	53	(
286	43	RCL
287	03	03
288	75	-
289	02	2
290	54	)
291	54	)
292	54	)
293	54	)
294	42	STO
295	08	08
296	69	OP
297	06	06
298	25	CLR
299	69	OP
300	00	00
301	02	2
302	06	6
303	01	1
304	04	4
305	69	OP
306	04	04
307	53	(
308	53	(
309	43	RCL
310	02	02
311	65	x
312	53	(
313	53	(
314	01	1
315	85	+
316	53	(
317	43	RCL
318	07	07
319	39	COS
320	54	)
321	54	)
322	45	y^x
323	43	RCL
324	03	03
325	54	)
326	54	)
327	55	÷
328	53	(
329	43	RCL
330	01	01
331	65	x
332	53	(
333	53	(
334	43	RCL
335	07	07
336	38	SIN
337	54	)
338	45	y^x
339	53	(
340	43	RCL
341	03	03

```
342  75 -
343  02 2
344  54 )
345  54 )
346  54 )
347  54 )
348  42 STO
349  09 09
350  69 OP
351  06 06
352  91 R/S
353  02 2
354  54 )
355  54 )
356  54 )
357  54 )
358  42 STO
359  09 09
360  69 OP
361  06 06
362  91 R/S
```

C. PART II PROGRAM

Given K from Part I, Part II program performs the probe calculations of the corresponding initial approach angles $(\phi_o)_A, (\phi_o)_B, (\phi_o)^*$, and $(\phi_o)_{NL}$ based on the relationship

$$f(\phi_o) = K_{A,B,*,NL}[\sin(\phi_o)_{A,B,*,NL}]^{P-1}$$
$$-r_o[(1+(\cos\phi_o)_{A,B,*,NL})^P] = 0$$

The program used a fixed torpedo speed of V_T = 35 kts (18 m/s) and an initial detection range of $r_o = R_D$ = 250 m. The purpose of this general probe program is to locate roots of the given function $y = f(\phi_o)$ to evaluate the slope of the tangent line, and to find the maximum and minimum points on a graph. We will only use the first feature.

The program requires a subroutine for the function to be investigated. This subroutine starts at program location 140 and is located at label 2nd C. The user's instructions for the program are as follows:

Procedure	Enter	Press	Display
Enter data	Starting Value of ϕ_o	2nd D	ϕ_o
Enter data	The increment $\Delta\phi_o$	2nd E	$\Delta\phi_o$
Calculate $f(\phi_o+\Delta\phi_o)$	--	A	$f(\phi_o+\Delta\phi_o)$
Calculate $f(\phi_o-\Delta\phi_o)$	--	B	$f(\phi_o-\Delta\phi_o)$
Display current value of ϕ_o	--	E	ϕ_o

If the value of $\Delta\phi_o$ is chosen too large, $\Delta\phi_o$ may be replaced by $\Delta\phi_o/10$ by pressing label 2nd A. Similarly, if a larger value of $\Delta\phi_o$ is required, $\Delta\phi_o$ can be replaced by $10\Delta\phi_o$ by pressing label 2nd B. A listing of the program steps follows, giving location (LOC), code (COD), key symbol (KEY), and comments.

Associated with the subroutine, it should be noted that the value of K, r_o and p are entered separately in the memory locations 10, 11, and 12, respectively.

000	76	LBL
001	19	D'
002	42	STO
003	01	01
004	91	R/S
005	76	LBL
006	10	E'
007	42	STO
008	02	02
009	91	R/S
010	76	LBL
011	11	A
012	53	(
013	43	RCL
014	01	01
015	85	+
016	43	RCL
017	02	02
018	54	)
019	42	STO
020	01	01
021	71	SBR
022	18	C'
023	91	R/S
024	76	LBL
025	12	B
026	53	(
027	43	RCL
028	01	01
029	75	-
030	43	RCL
031	02	02
032	54	)
033	42	STO
034	01	01
035	71	SBR
036	18	C'
037	91	R/S
038	76	LBL
039	13	C
040	53	(
041	43	RCL
042	01	01
043	85	+
044	43	RCL
045	02	02
046	55	÷
047	02	2
048	54	)
049	71	SBR
050	18	C'
051	42	STO
052	03	03
053	53	(
054	43	RCL
055	01	01
056	75	-
057	43	RCL
058	02	02
059	55	÷
060	02	2
061	54	)
062	71	SBR
063	18	C'
064	42	STO
065	04	04
066	53	(
067	53	(
068	43	RCL
069	03	03
070	75	-
071	43	RCL
072	04	04
073	54	)
074	55	÷
075	43	RCL
076	02	02
077	54	)
078	91	R/S
079	76	LBL
080	14	D
081	53	(
082	43	RCL
083	01	01
084	85	+
085	43	RCL
086	02	02
087	54	)
088	71	SBR
089	18	C'
090	42	STO
091	03	03
092	43	RCL
093	01	01
094	71	SBR
095	18	C'
096	42	STO
097	04	04
098	53	(
099	53	(
100	43	RCL
101	43	RCL
102	75	-
103	43	RCL
104	04	04
105	54	)
106	55	÷
107	43	RCL
108	02	02
109	54	)
110	91	R/S
111	76	LBL
112	15	E
113	43	RCL
114	01	01
115	91	R/S
116	76	LBL
117	16	A'
118	53	(
119	43	RCL
120	02	02
121	55	÷
122	01	1
123	00	0
124	54	)
125	42	STO
126	02	02
127	91	R/S
128	76	LBL
129	17	B'
130	53	(
131	43	RCL
132	02	02
133	65	x
134	01	1
135	00	0
136	54	)
137	42	STO
138	02	02
139	91	R/S
140	76	LBL
141	18	C'
142	42	STO
143	00	00
144	70	RAD
145	53	(
146	53	(
147	43	RCL
148	10	10
149	65	x
150	53	(
151	53	(
152	43	RCL

```
153  00 00
154  38 SIN
155  54 )
156  45 y^x
157  43 RCL
158  13 13
159  54 )
160  54 )
161  75 -
162  53 (
163  43 RCL
164  11 11
165  65 x
166  53 (
167  53 (
168  01 1
169  85 +
170  53 (
171  43 RCL
172  00 00
173  39 COS
174  54 )
175  54 )
176  45 y^x
177  43 RCL
178  12 12
179  54 )
180  54 )
181  54 )
182  92 RTN
```

APPENDIX F

FIGURES

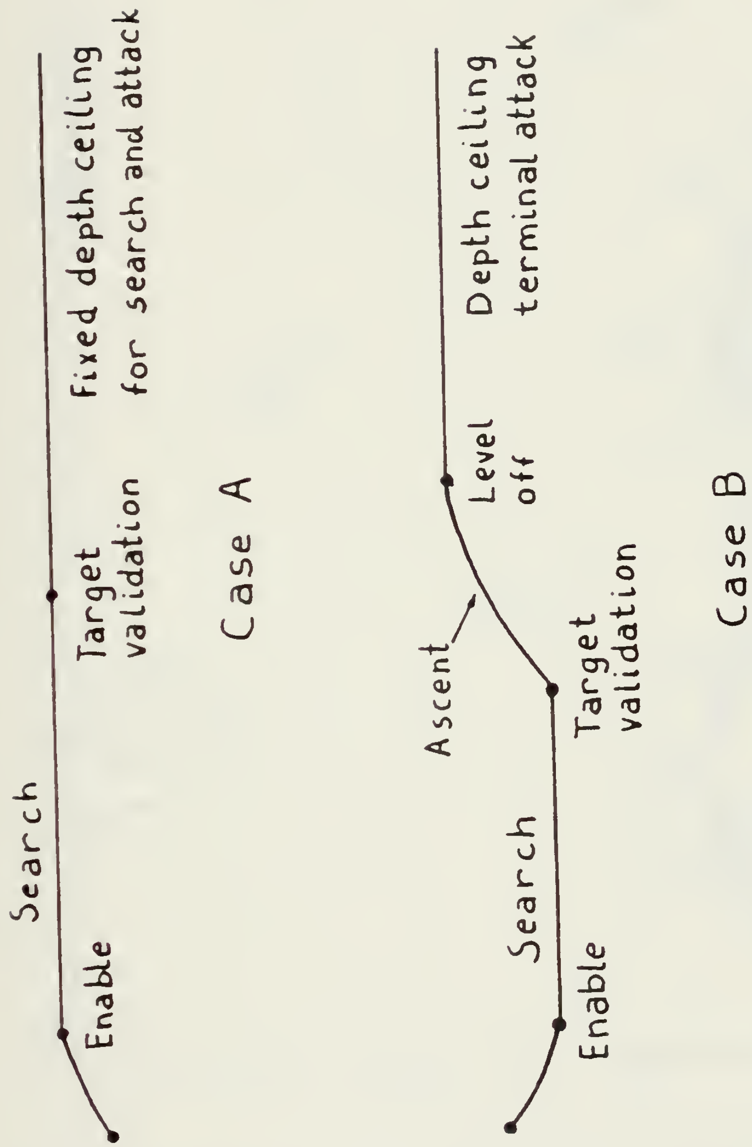

Fig. 1. Torpedo Search and Attack Geometry.

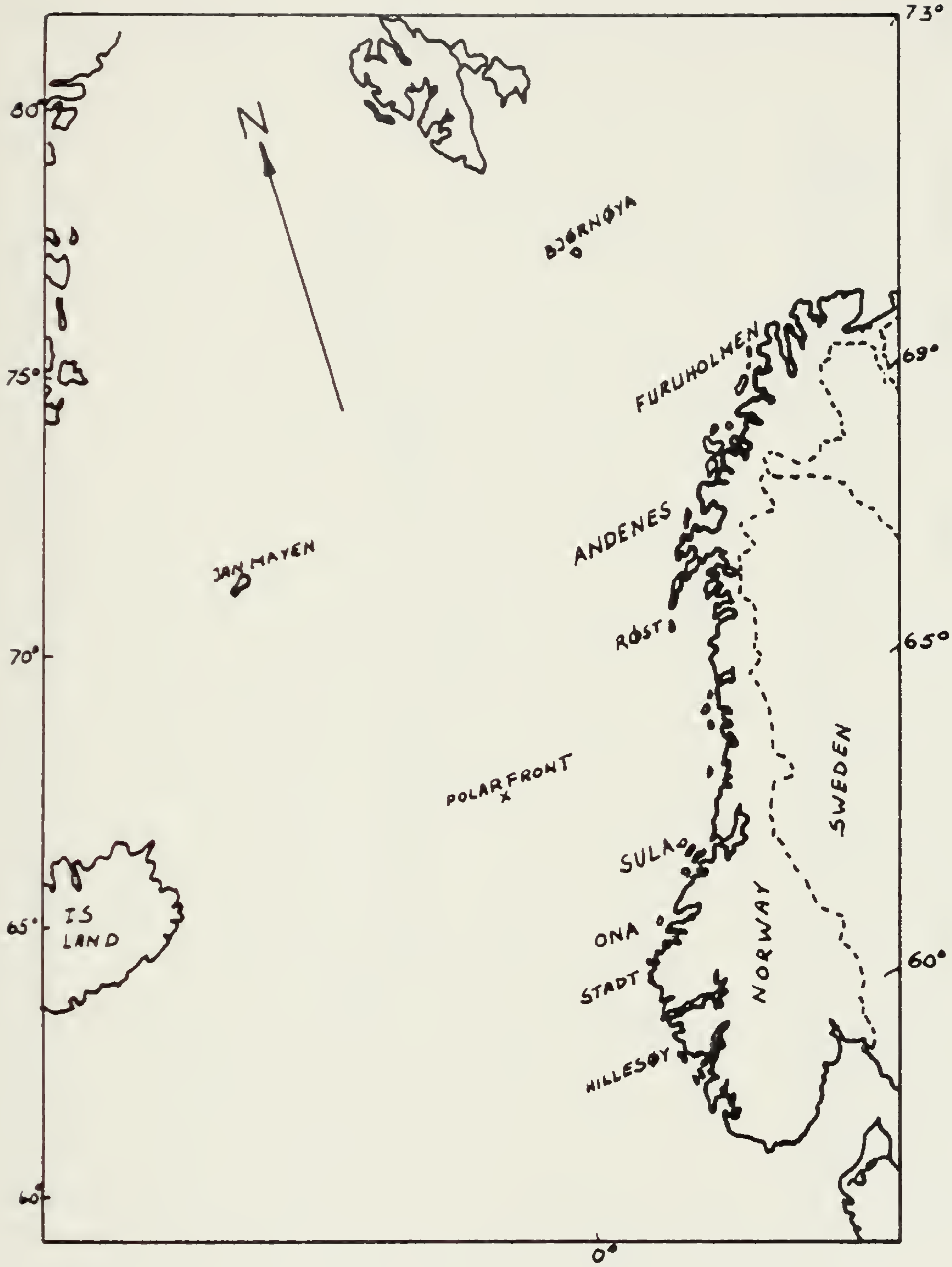

Fig. 2. Location of Weather Stations Along the Norwegian Coast.

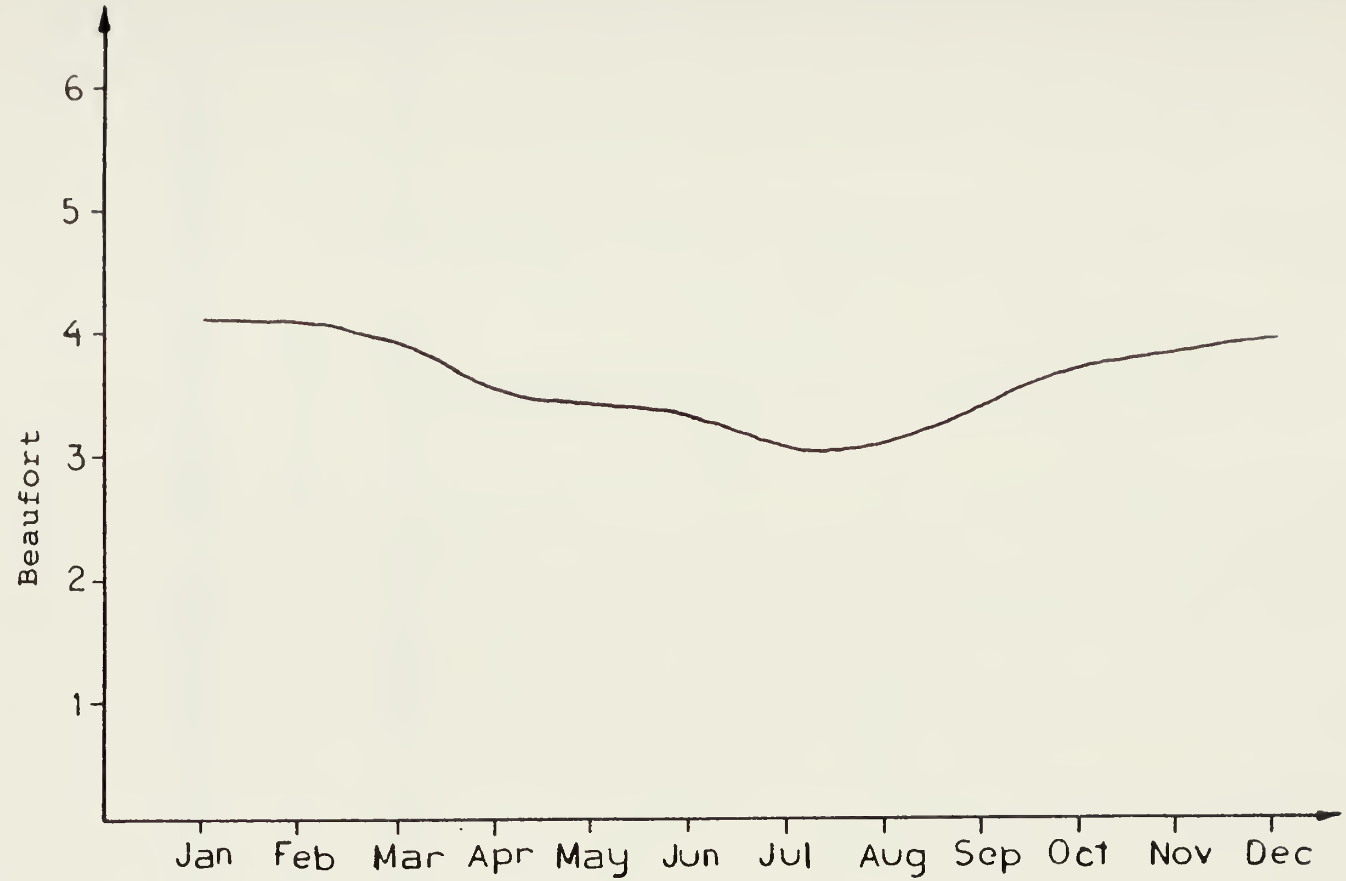

Fig. 3. Average Monthly Wind Speed in Beaufort from the Weather Station "Andenes."

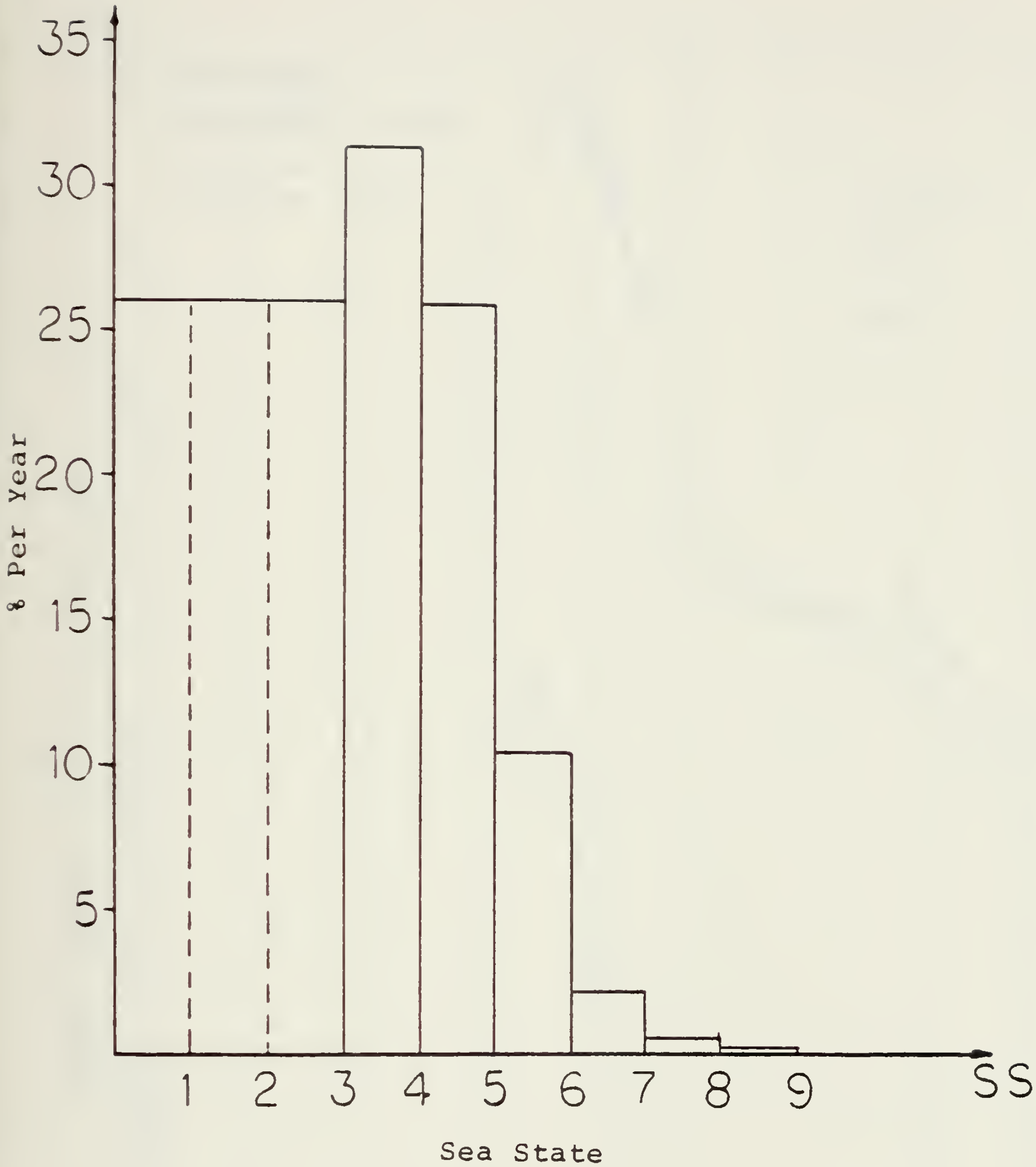

Fig. 4. Histogram of Significant Wave in Percent per Year from the Weather Station "Andenes."

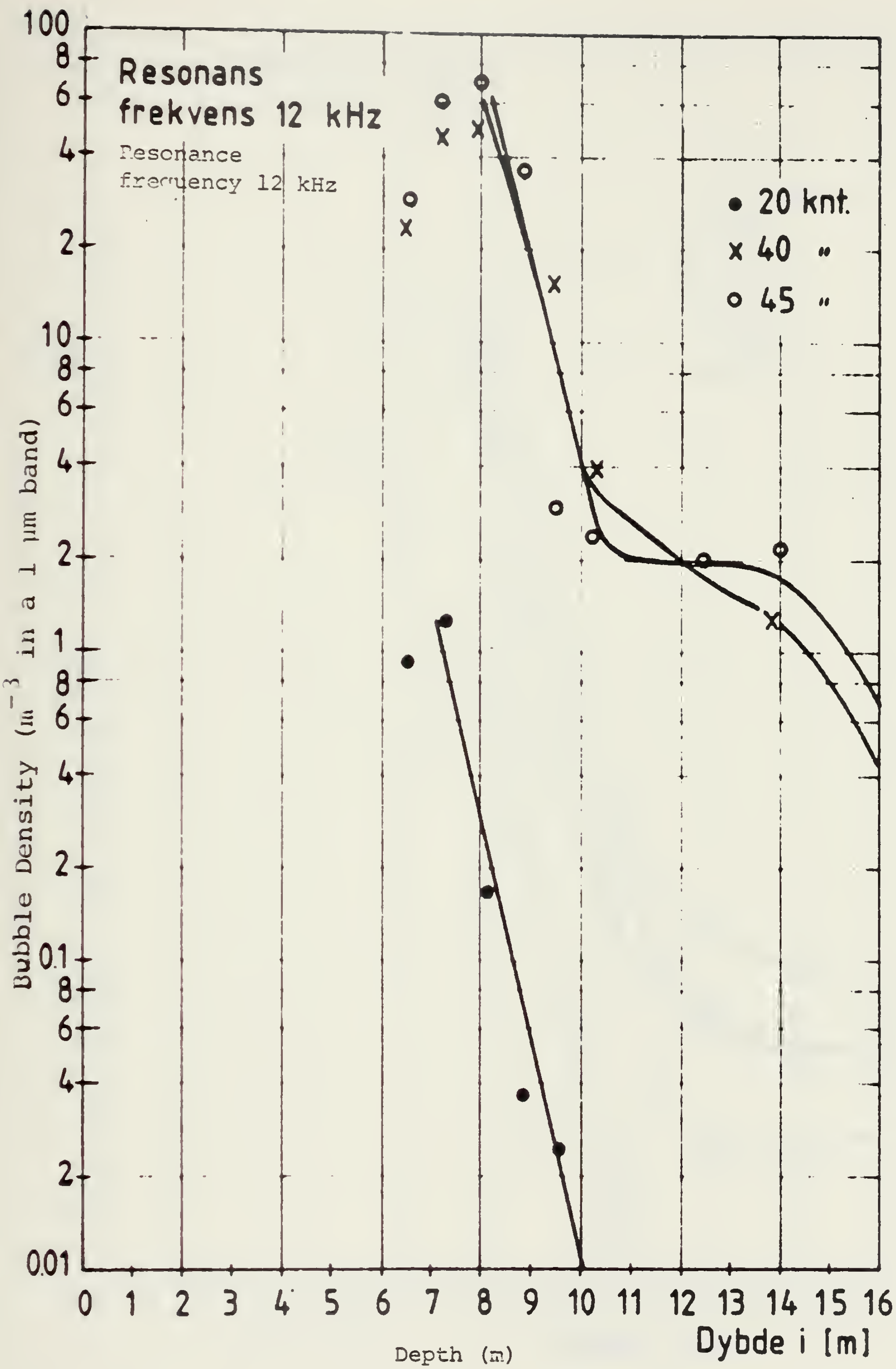

Fig. 5. Resonant Bubble Density at 12 kHz as a Function of Depth.

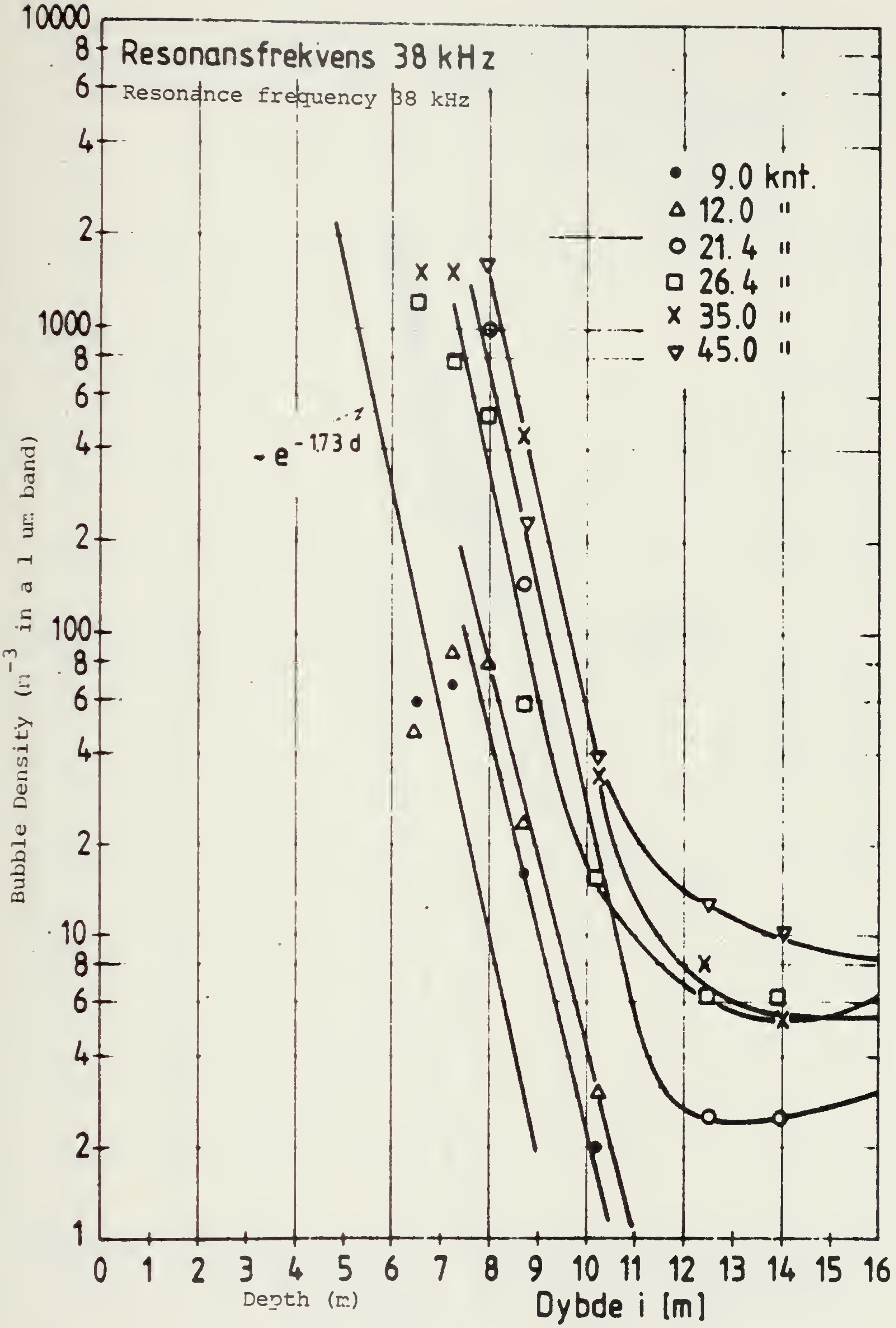

Fig. 6. Resonant Bubble Density at 38 kHz as a Function of Depth.

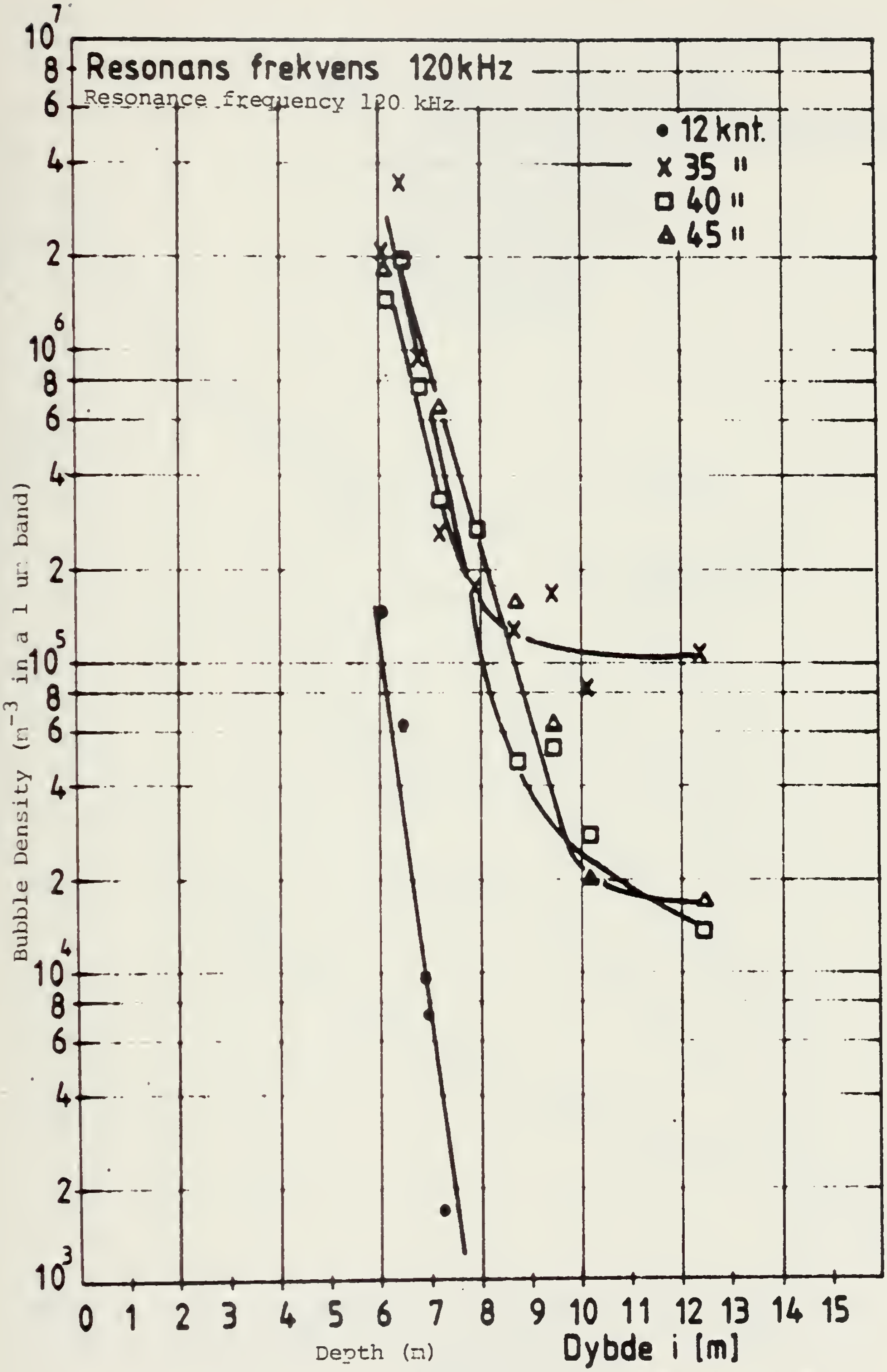

Fig. 7. Resonant Bubble Density at 120 kHz as a Function of Depth.

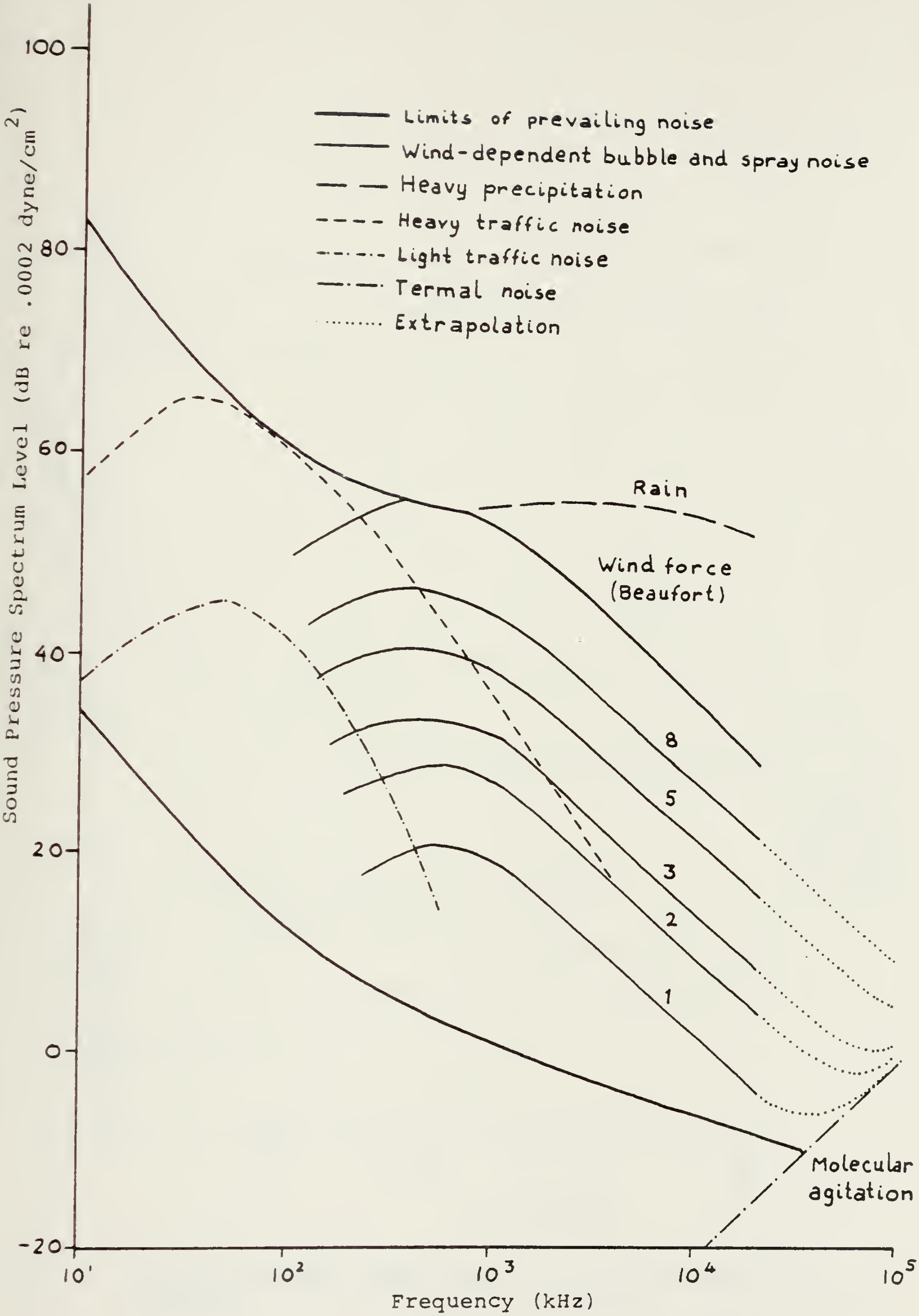

Fig. 8. Ambient Noise Level Curves.

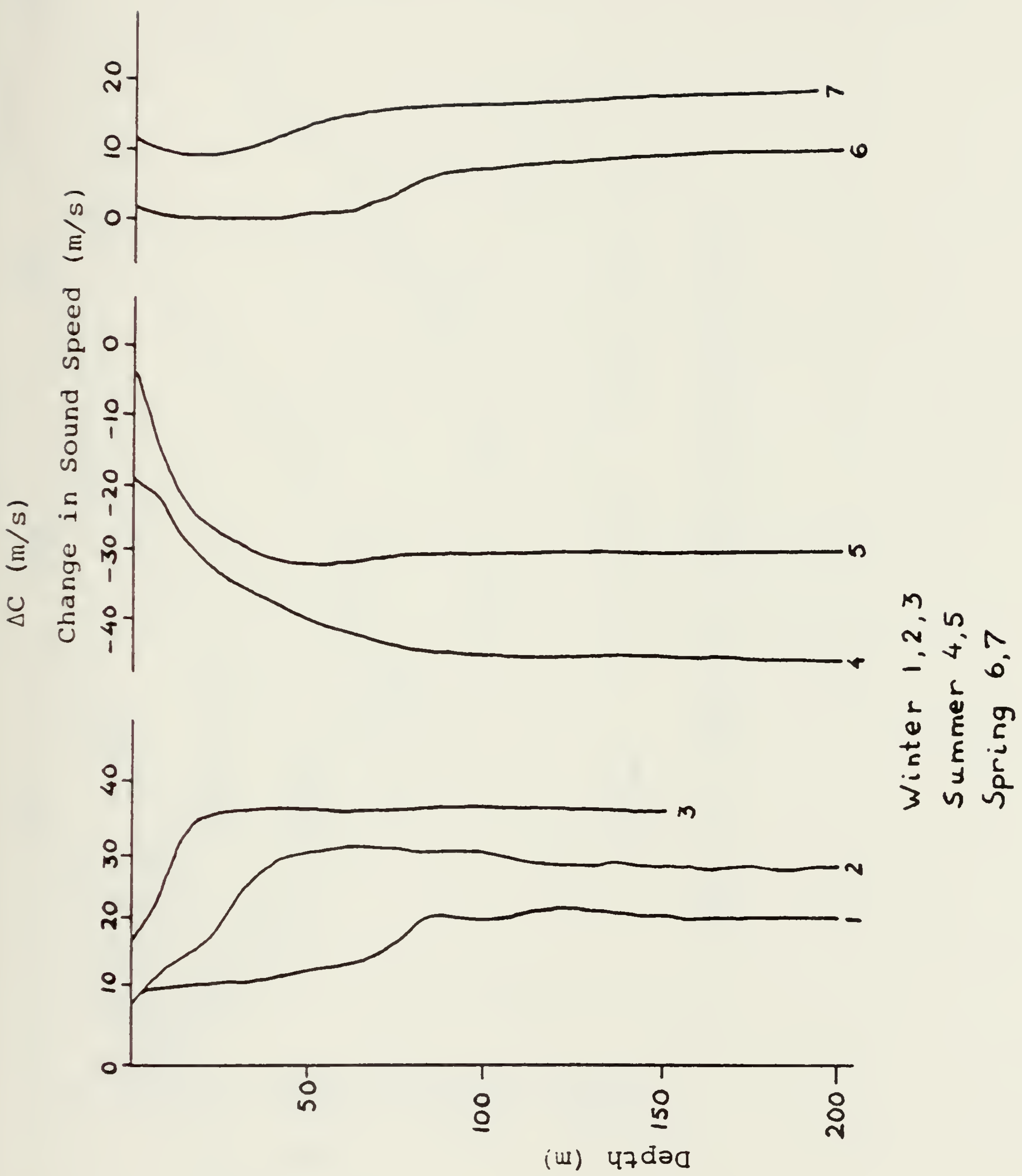

Fig. 9. Typical Sound Speed Profiles in Norwegian Coastal Waters.

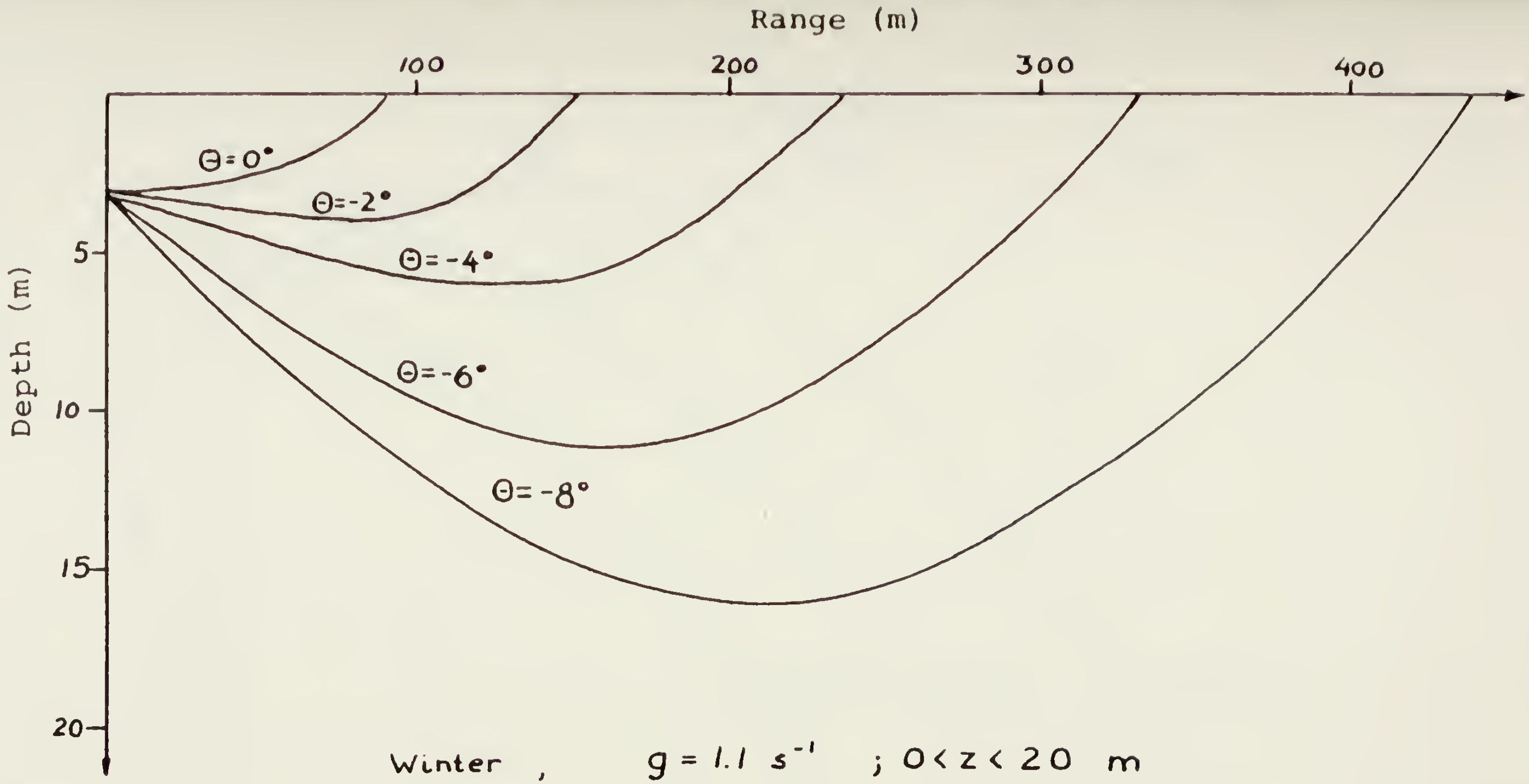

Fig. 10. Worst Case Ray Path During Winter.

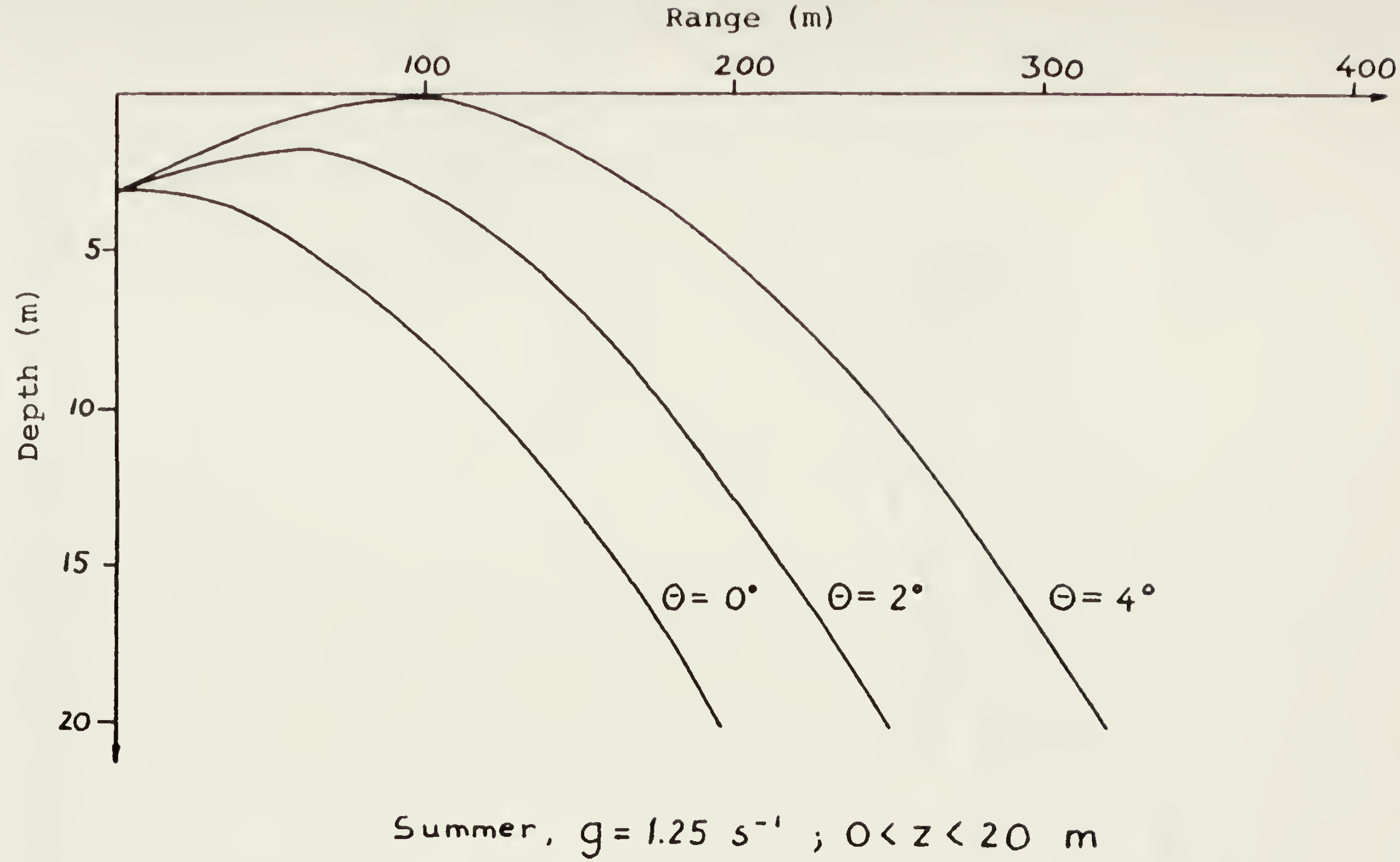

Fig. 11. Worst Case Ray Path During Summer.

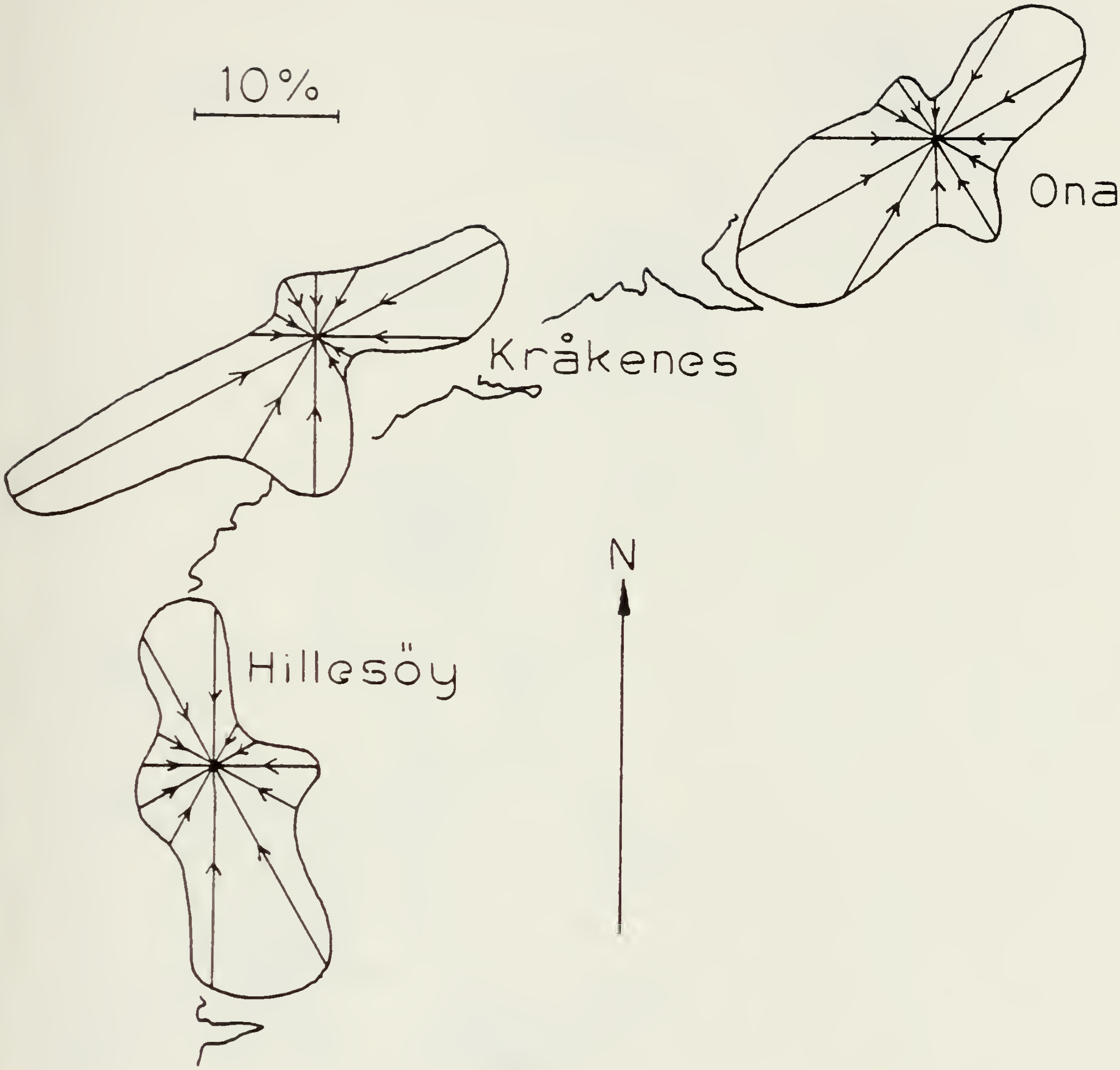

Fig. 12. Frequencies of Wind Directions in Percent for Stations Along the Coast from "Hillesöy" to "Ona."

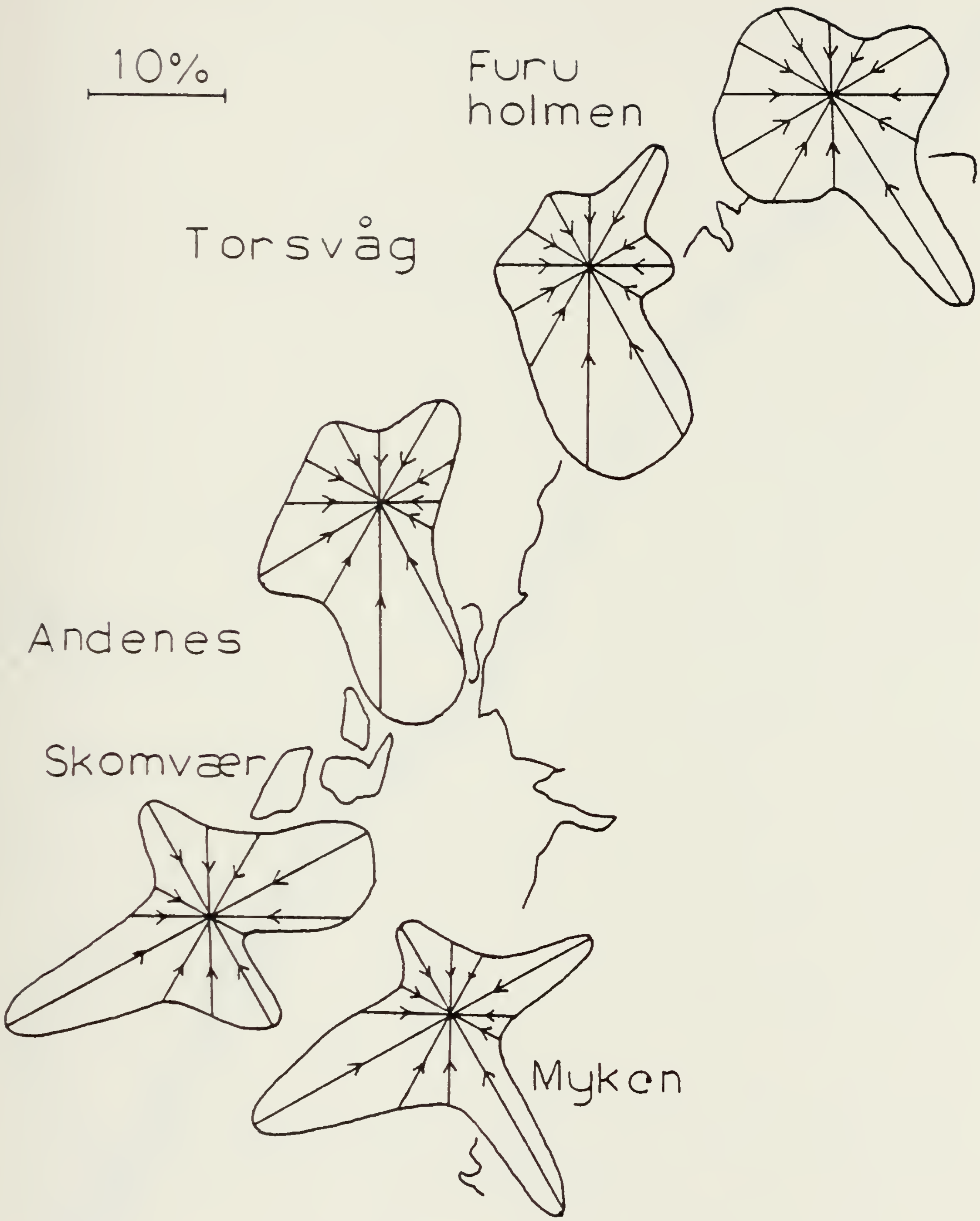

Fig. 13. Frequencies of Wind Directions in Percent for Stations Along the Coast from "Myken" to "Furuholmen."

Fig. 14. Absorption Coefficient in dB/m as a Function of Frequency.

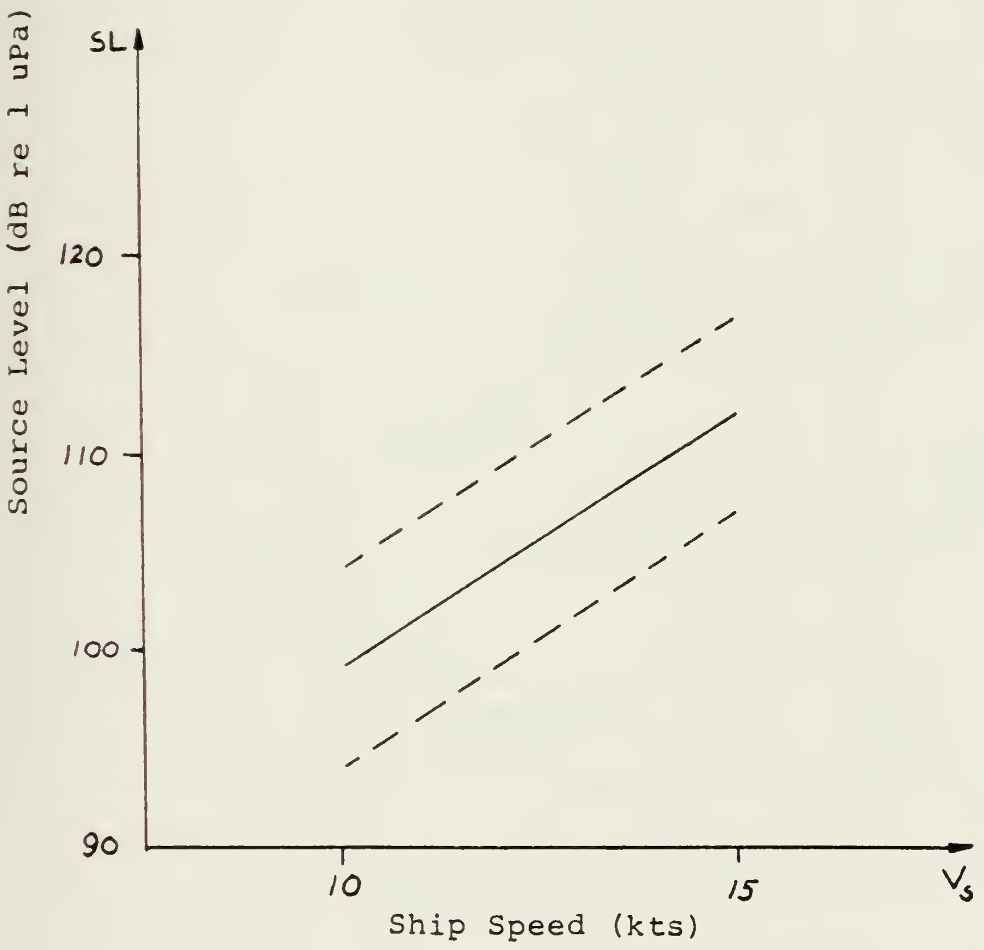

Fig. 15. Average Radiated Spectrum Level for Surface Ship as a Function of Speed in kts.

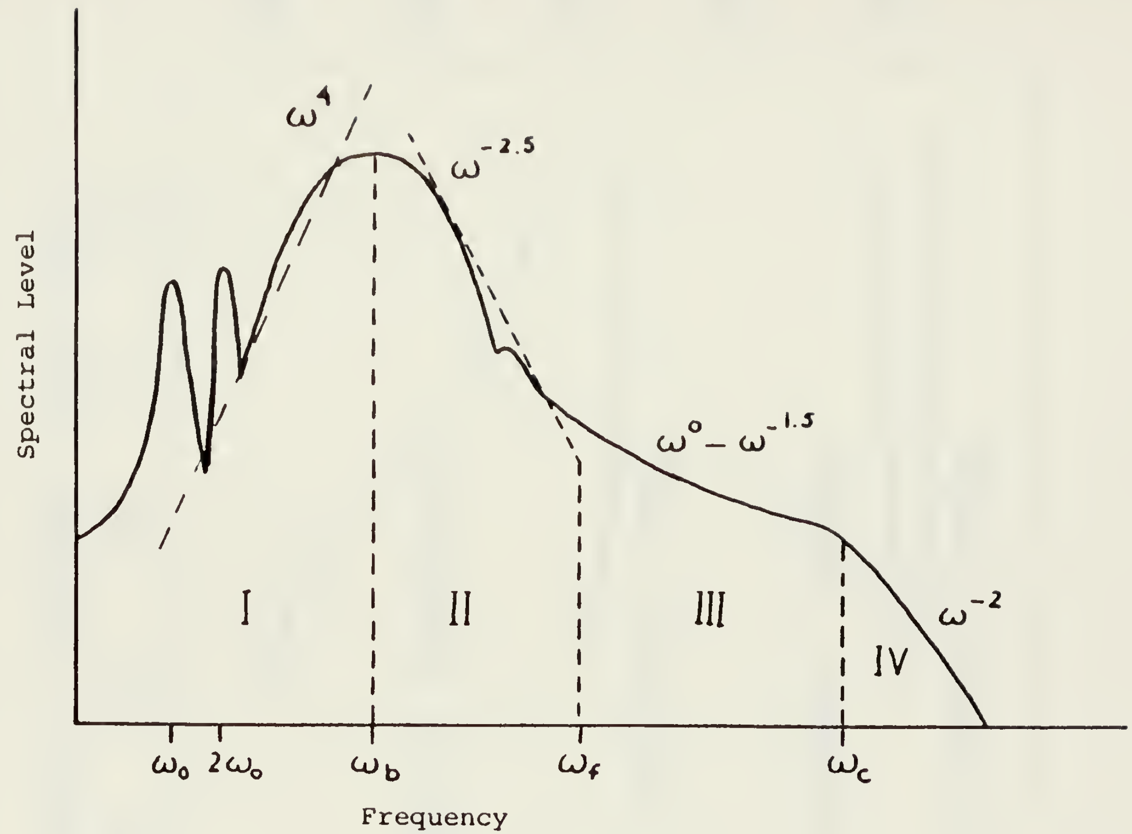

Fig. 16. General Noise Spectrum for a Cavitating Propeller.

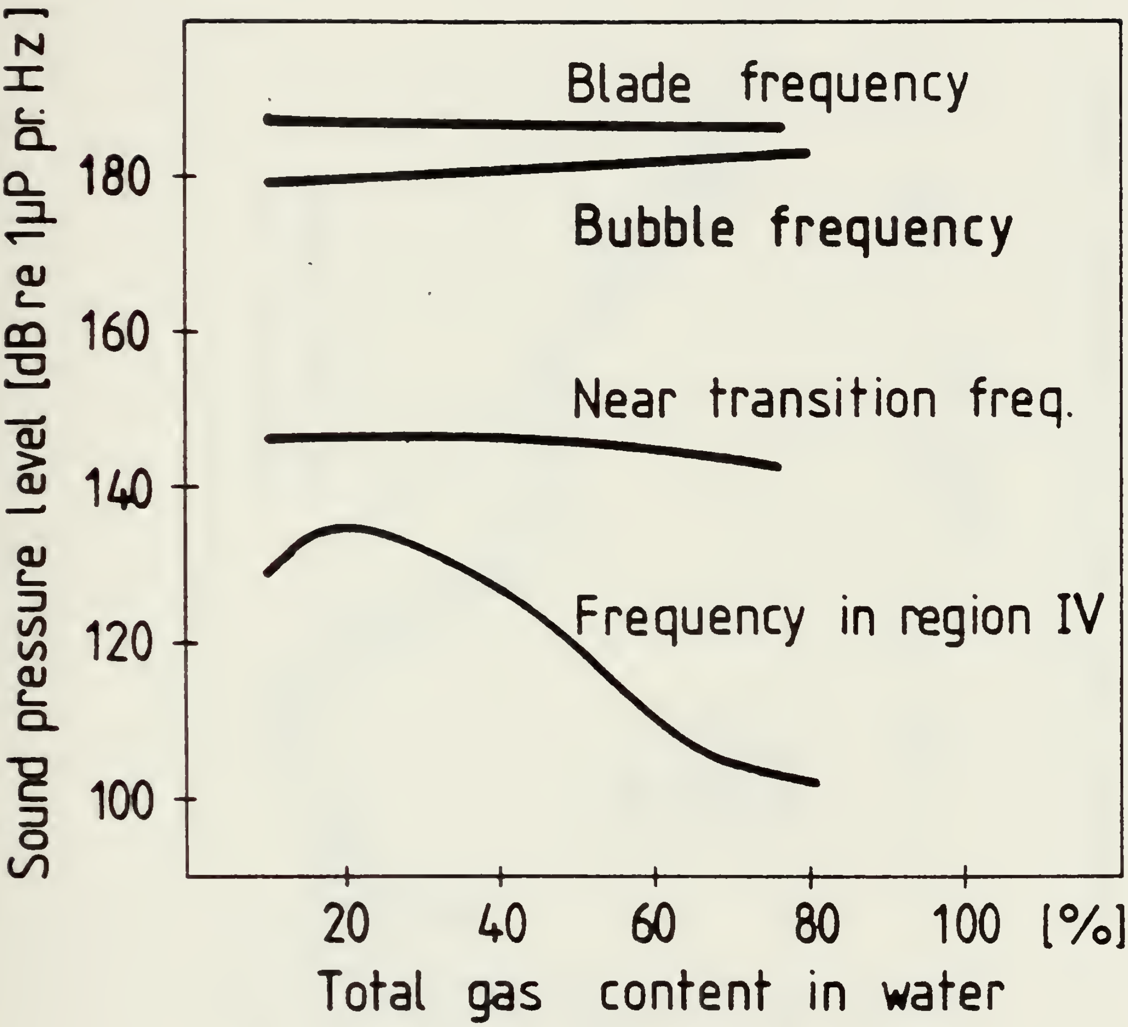

Fig. 17. Spectrum Level as a Function of Total Gas Content

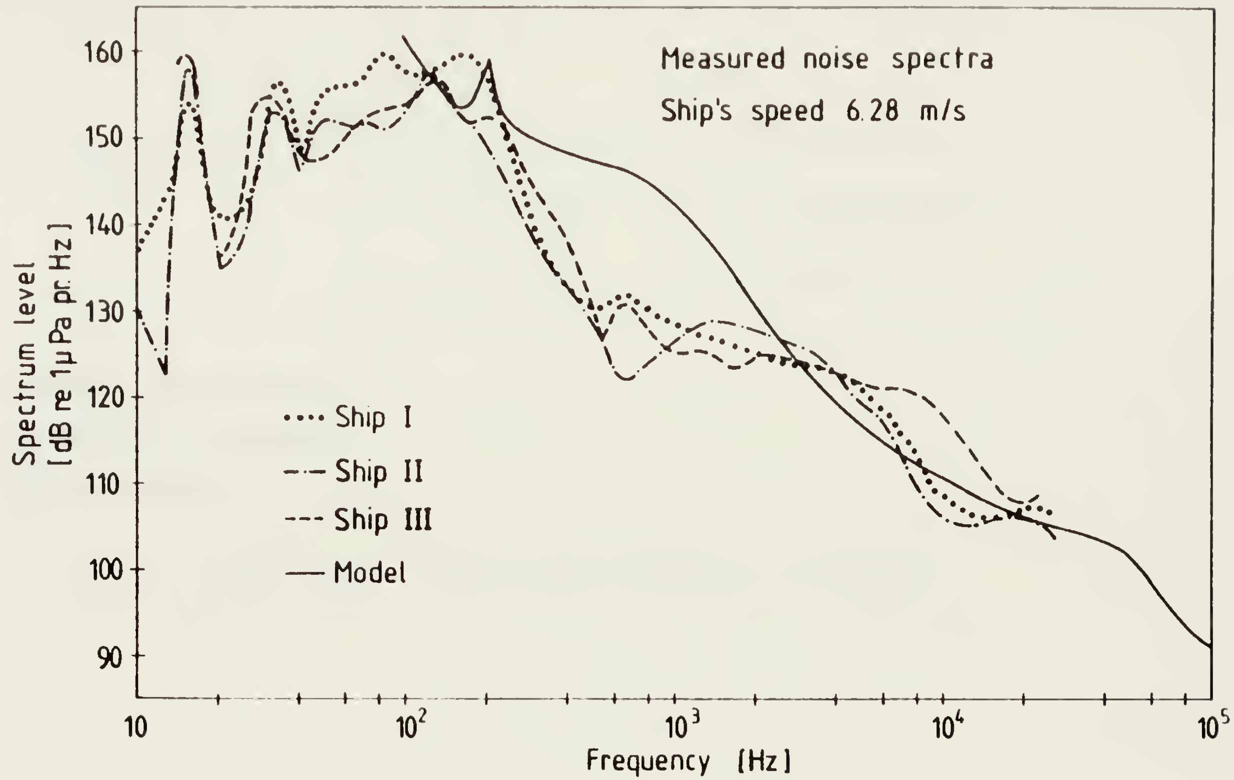

Fig. 18. Measured Model and Full Scale Noise Spectra.

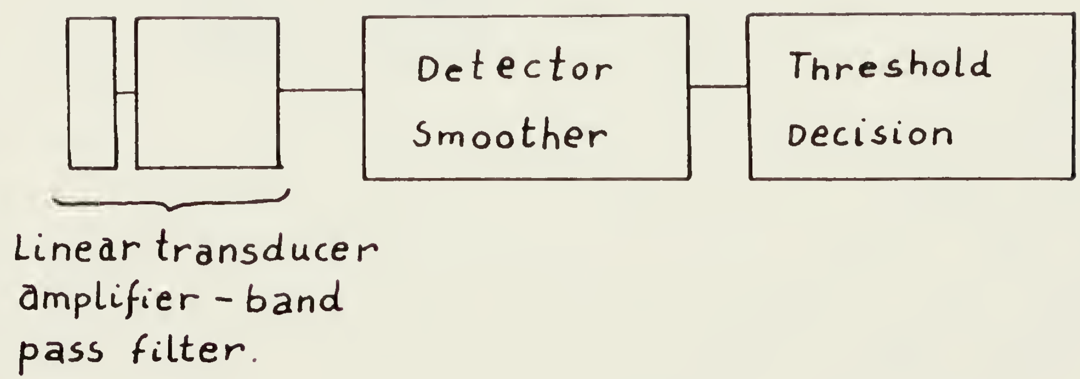

Fig. 19. Square Law Detector Scheme.

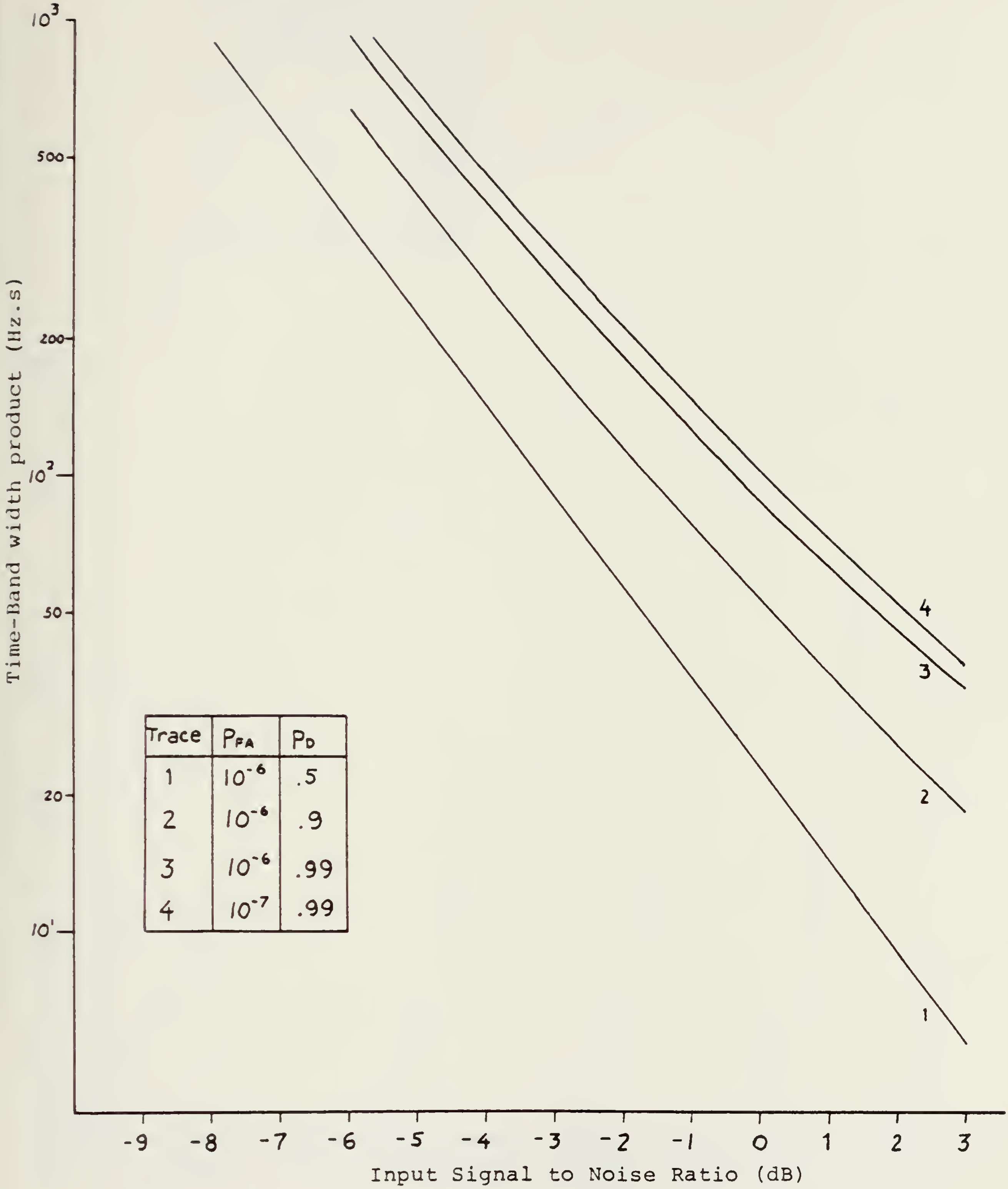

Fig. 20. Required Input S/N Ratio and BT Product for Various Operating Probabilities.

Trace	Threshold above NL	P_{FA}
1	.88	10^{-6}
2	1.0	2×10^{-8}
3	1.5	1×10^{-18}
4	2.0	1×10^{-35}
5	2.5	1×10^{-54}
6	3.0	1×10^{-98}

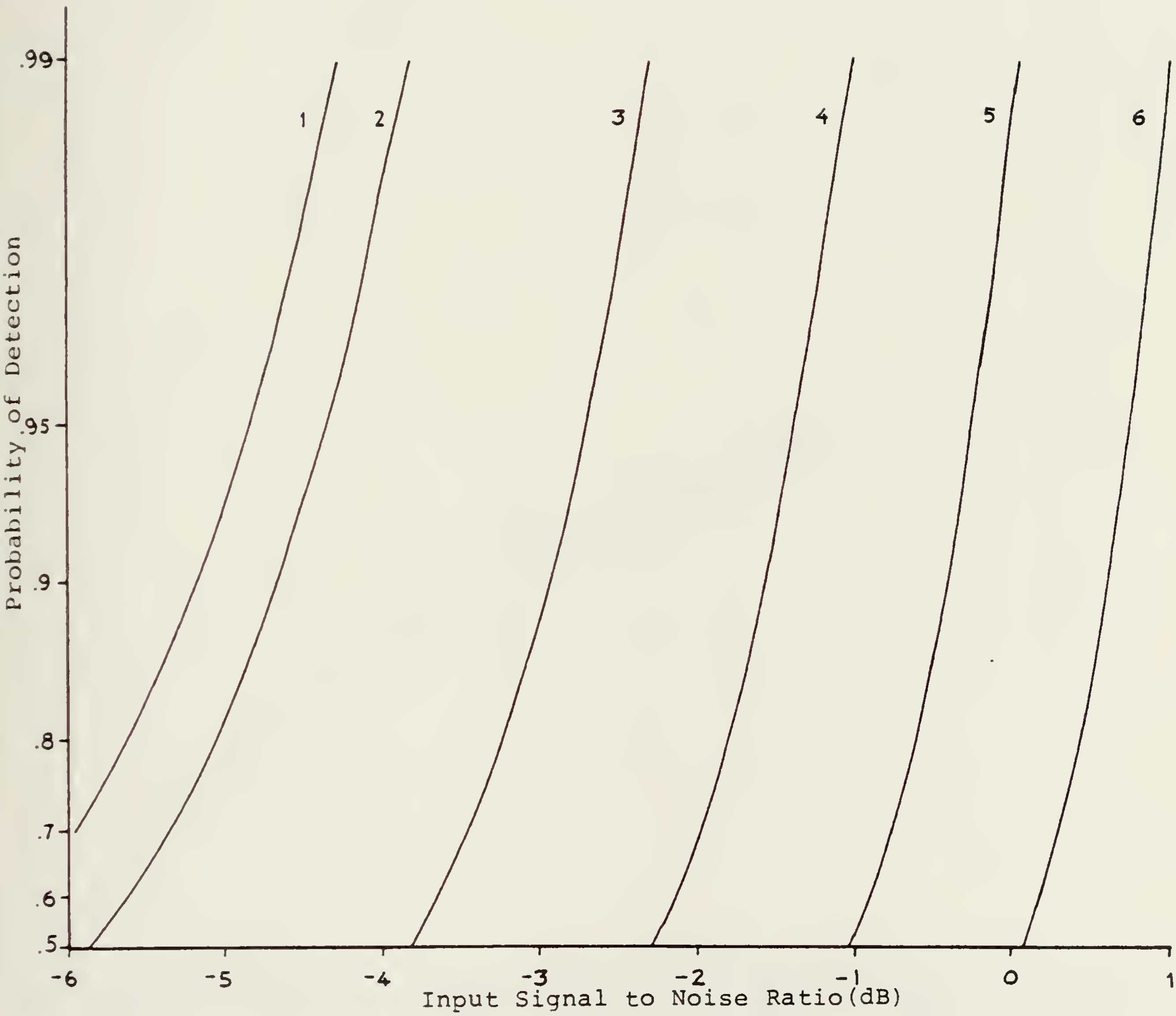

Fig. 21. Probability of Detection Versus Input S/N Ratio for Various Thresholds.

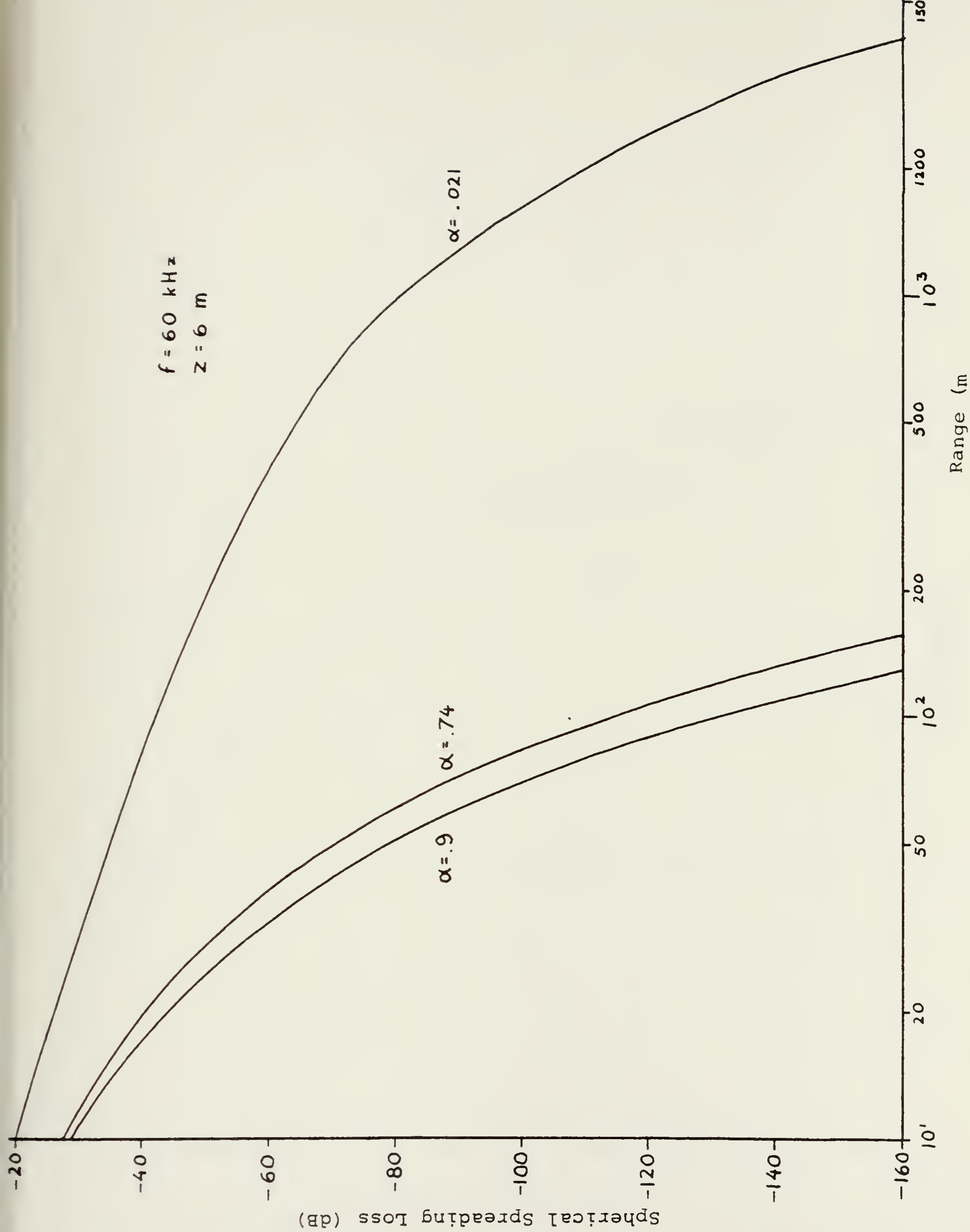

Fig. 22. -20logR -αR Versus R for Frequency of 60 kHz.

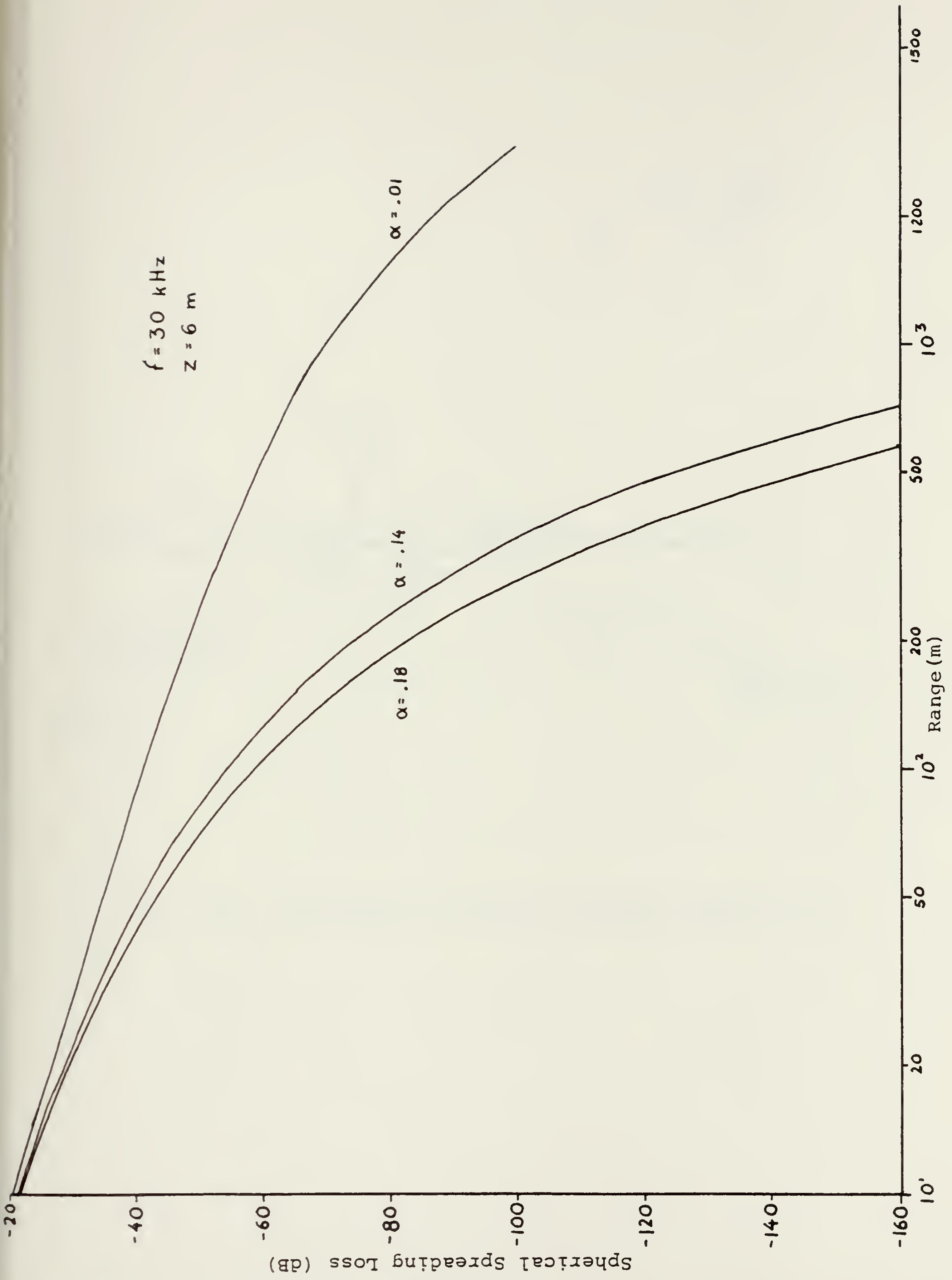

Fig. 23. -20logR -αR Versus R for a Frequency of 30 kHz.

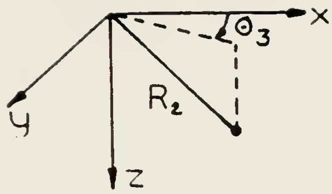

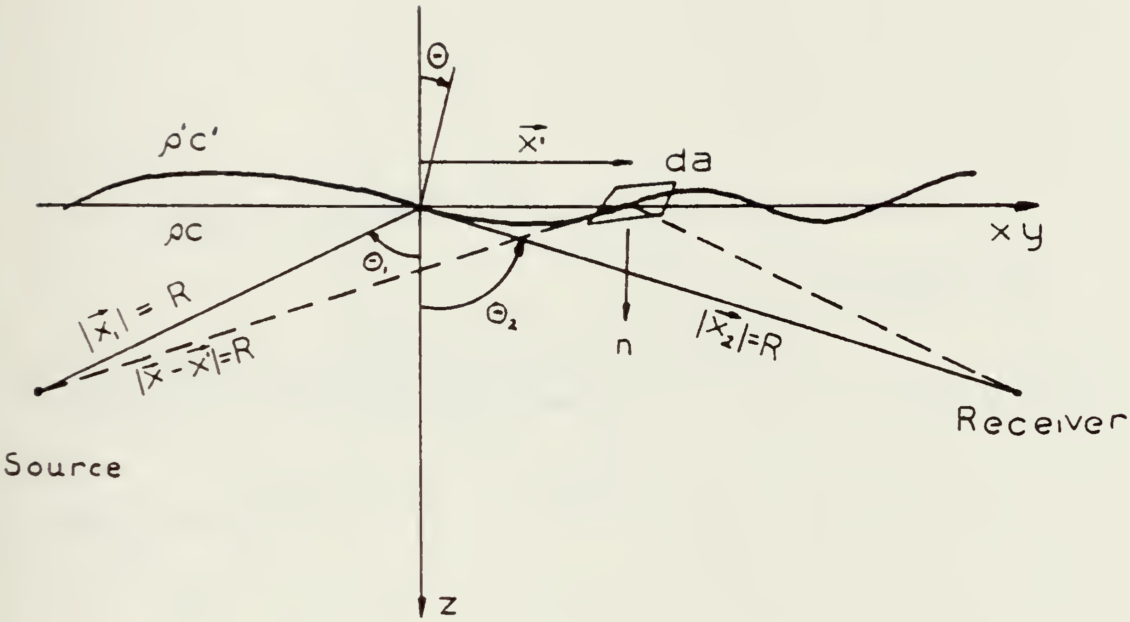

Fig. 24a. Geometry at the Sea Surface Scattering.

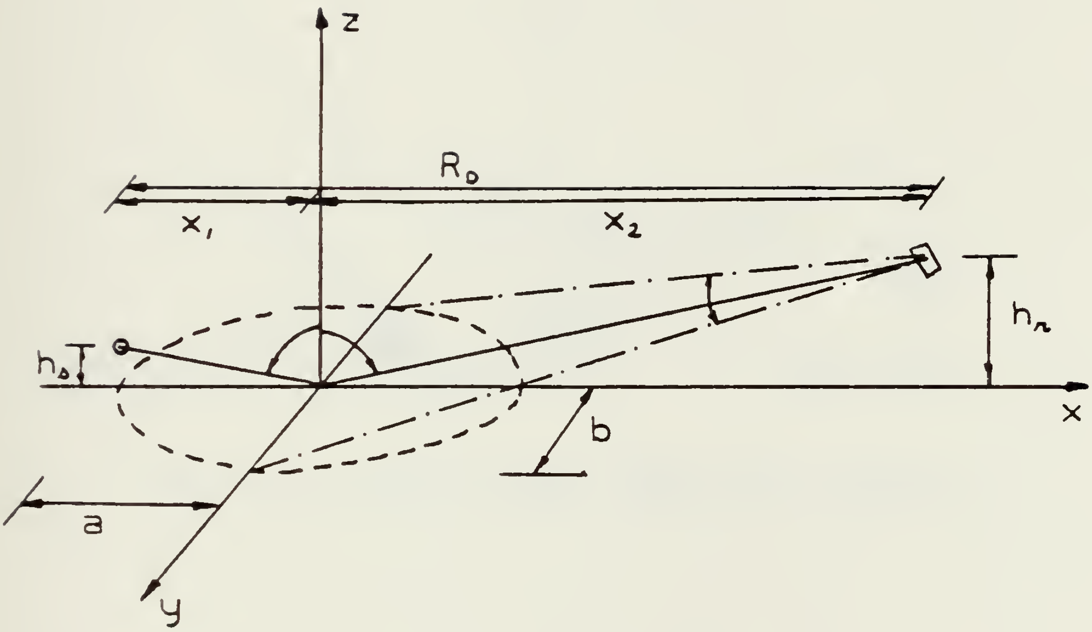

Fig. 24b. Specular Scattering Geometry.

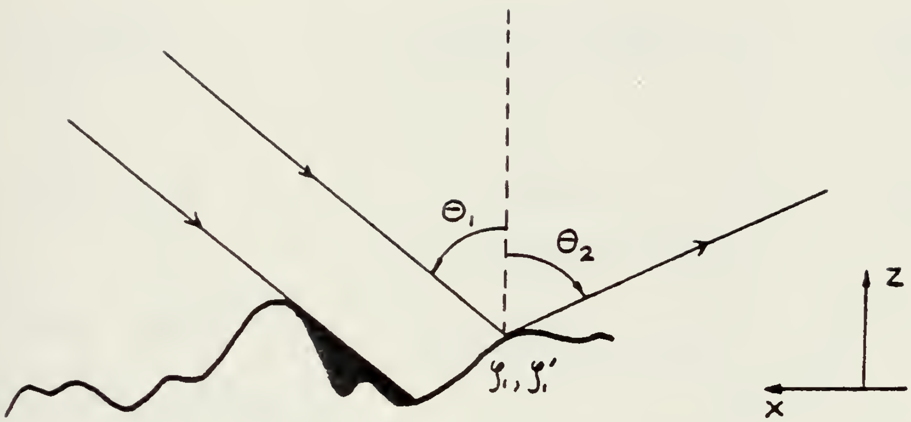

Fig. 25. Rough Surface Shadowing Geometry.

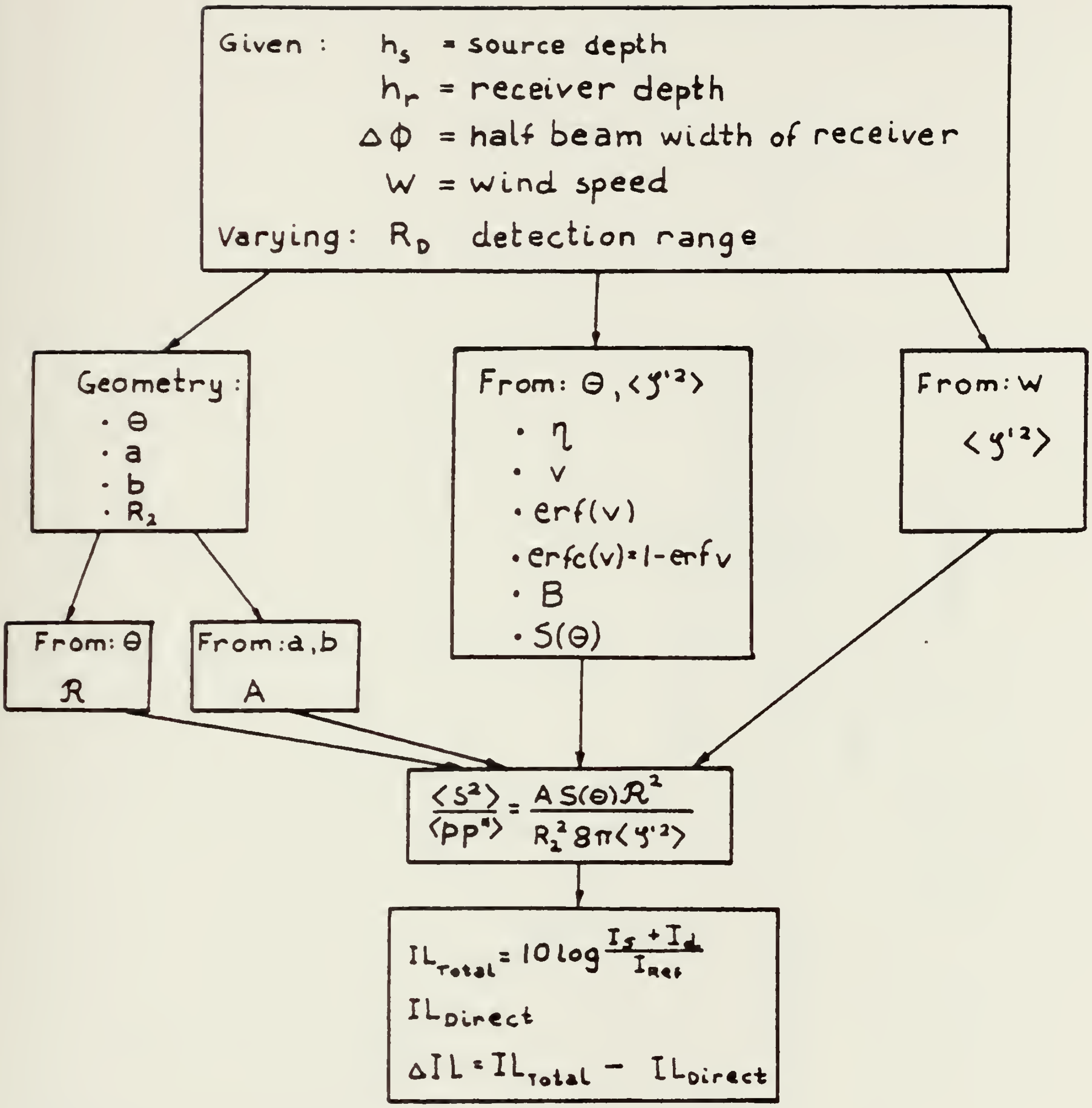

Fig. 26. Calculation Scheme of the Surface Scattering Effect.

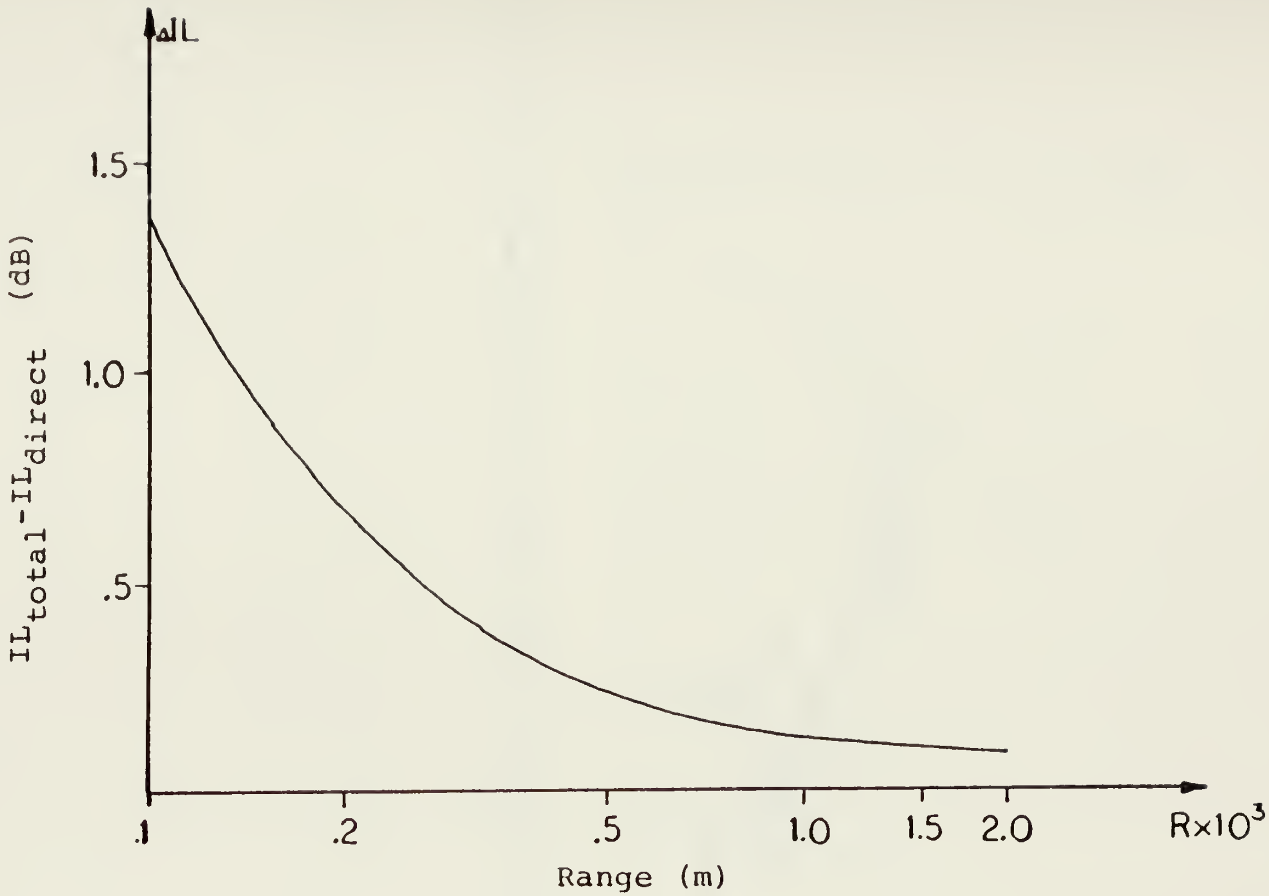

Fig. 27. ΔIL Versus R.

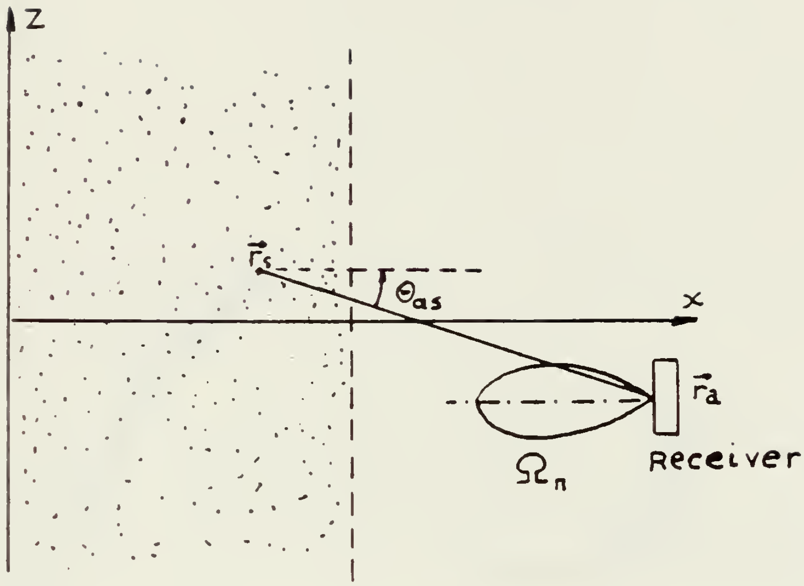

Fig. 28. Geometry of the Subsurface Propagation Model.

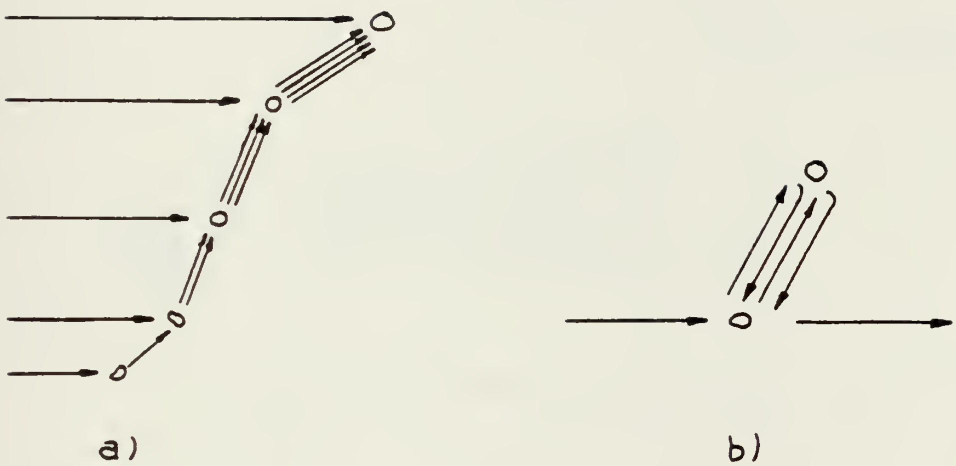

Fig. 29. a) Chains of Successive Scattering.

b) Scattering Pattern Going Through the Same Scatterer More than Once.

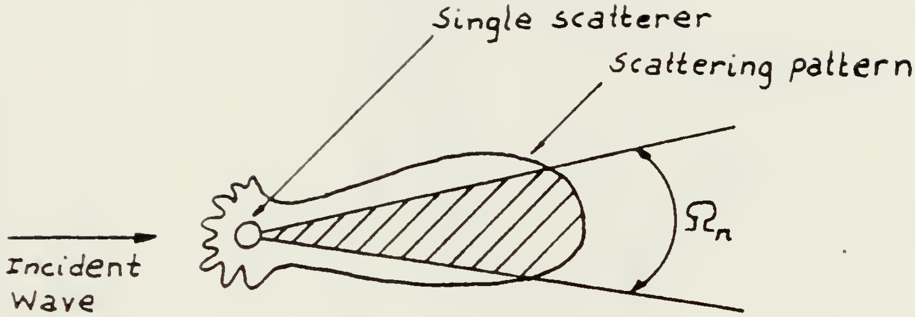

Fig. 30. Scattering Pattern.

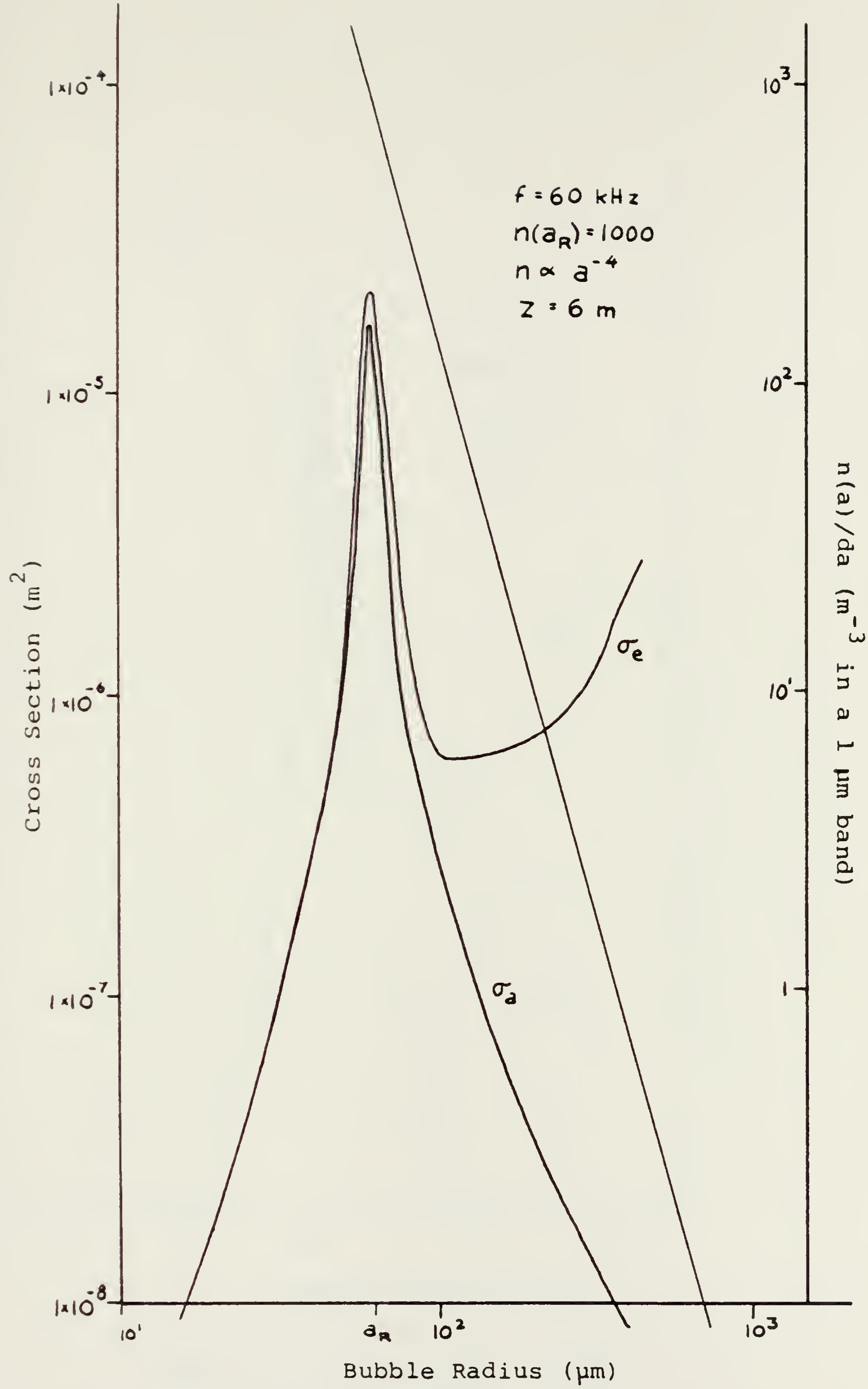

Fig. 31. σ_e and σ_a for 60 kHz.

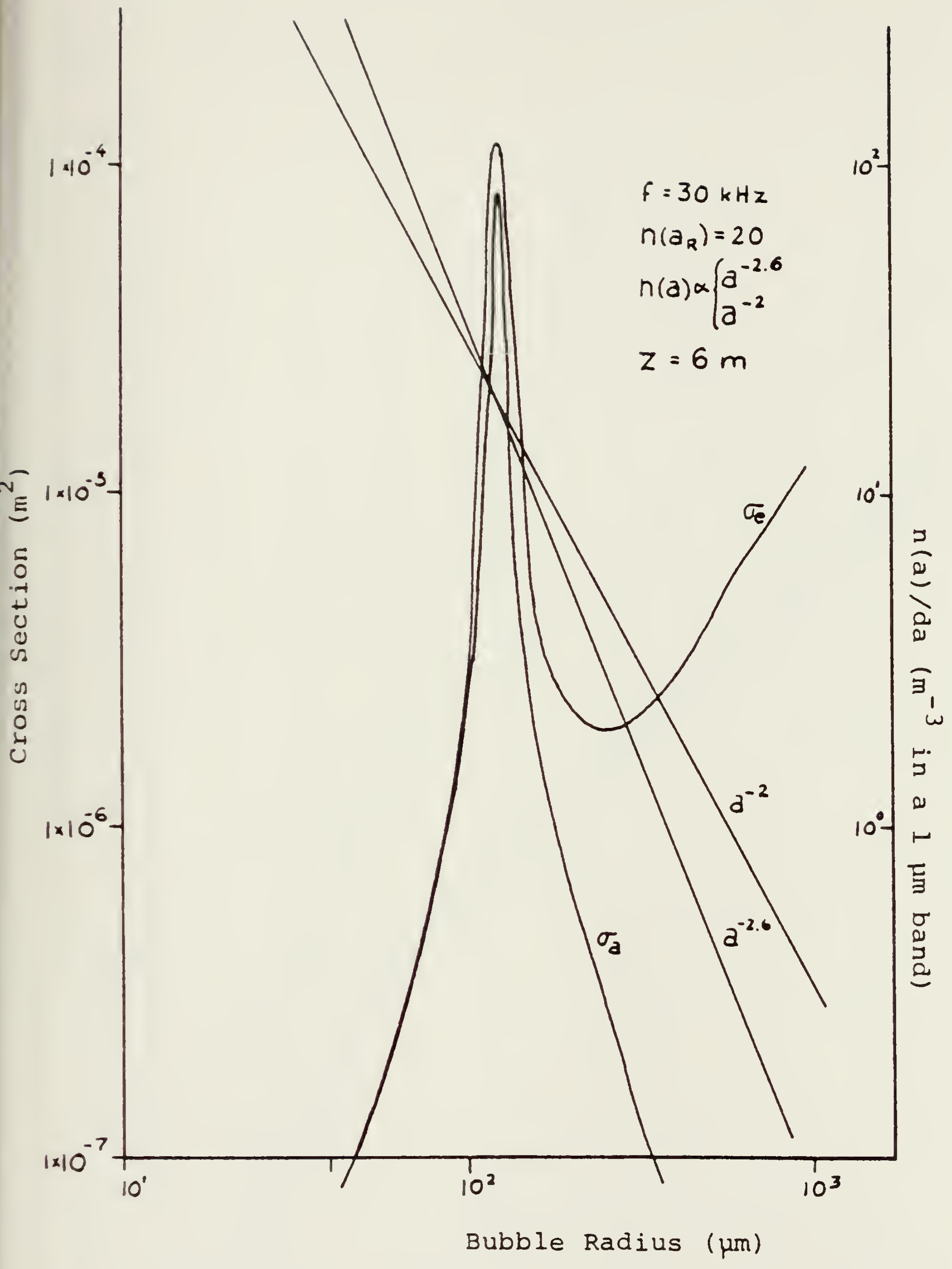

Fig. 32. σ_e and σ_a for 30 kHz.

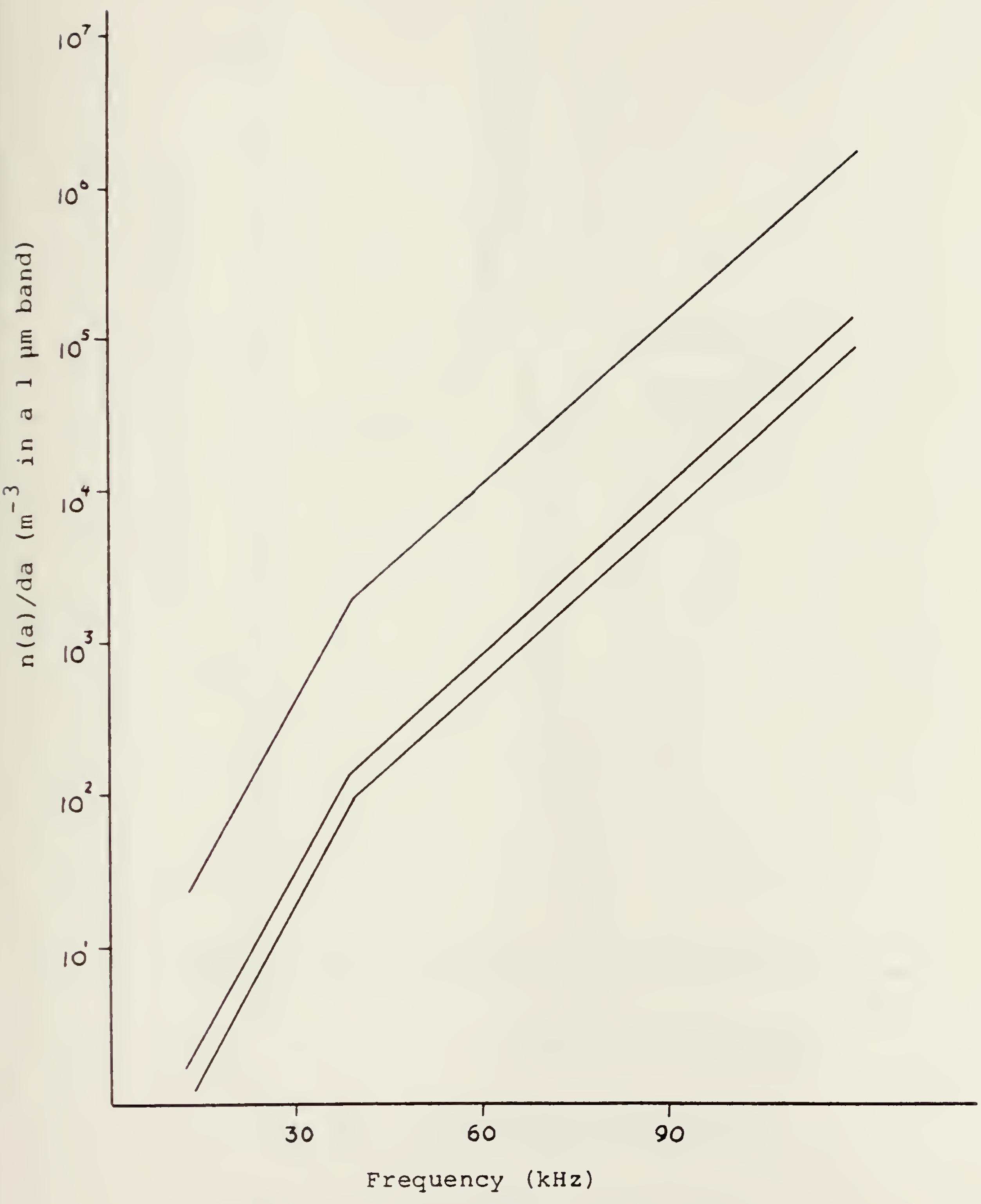

Fig. 33. Interpolated Bubble Data.

Fig. 34. $\sigma_e(a)n(a)da$ for 60 kHz.

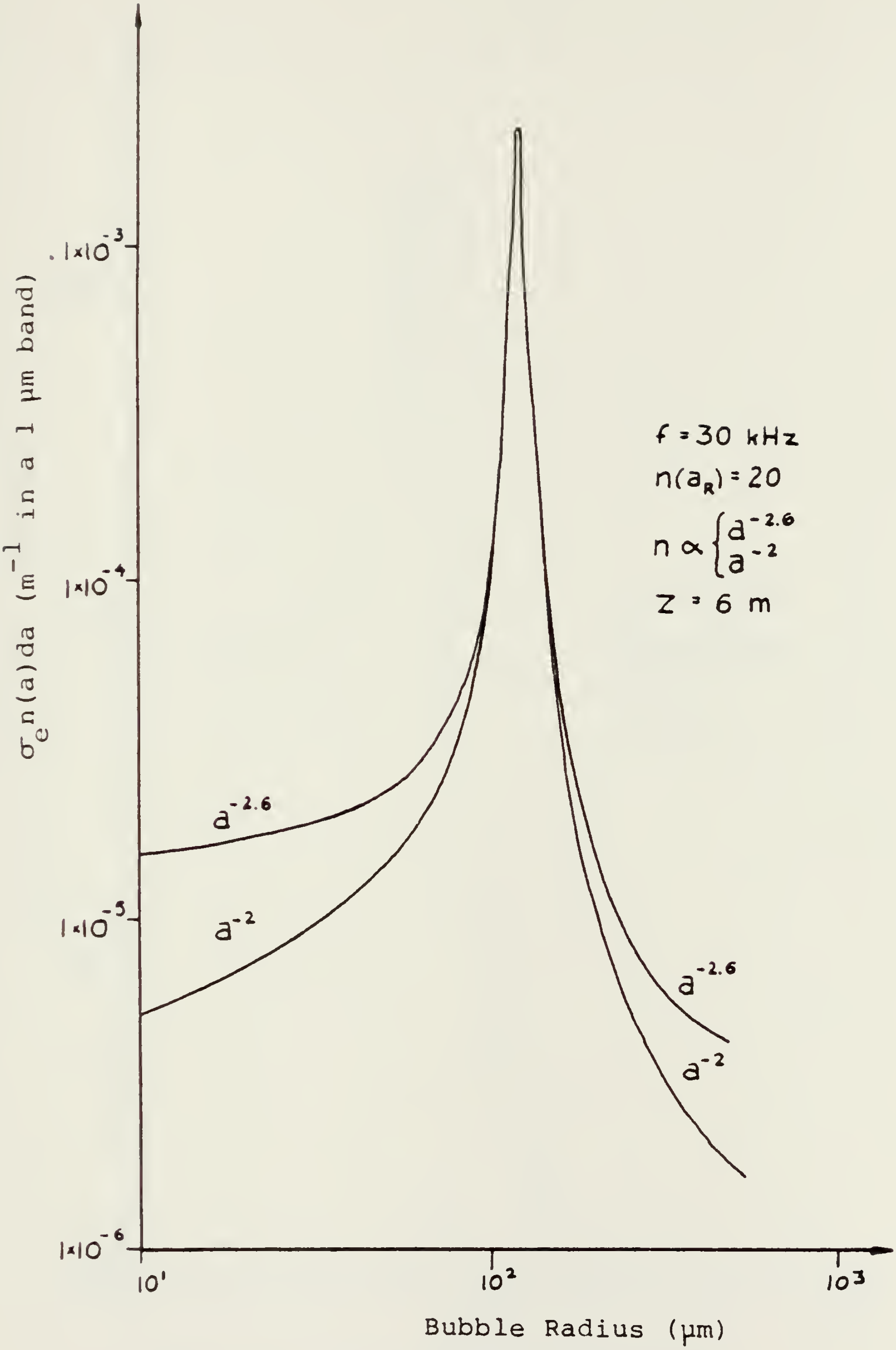

Fig. 35. $\sigma_e(a)n(a)da$ for 30 kHz.

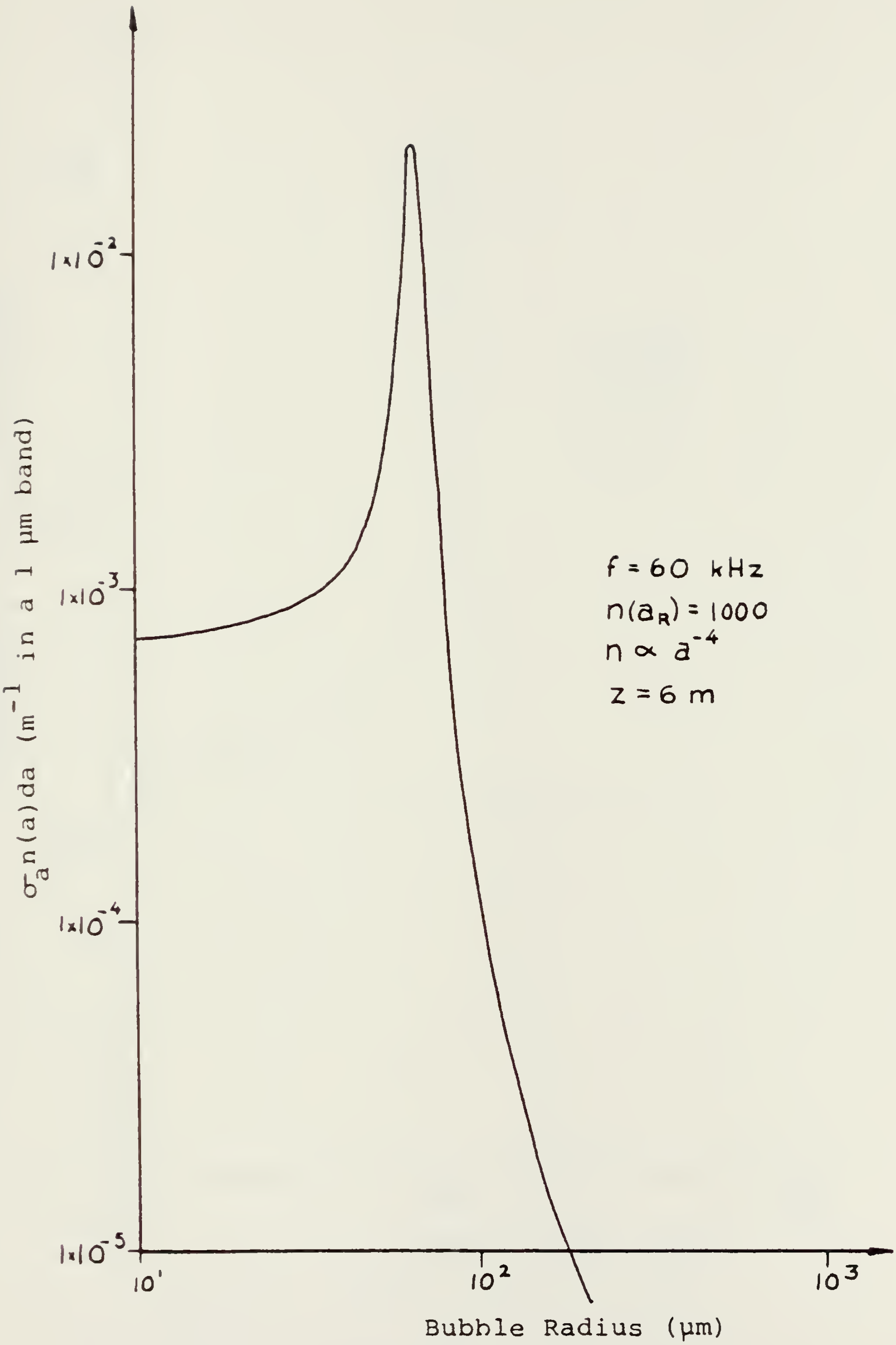

Fig. 36. $\sigma_a(a)n(a)da$ for 60 kHz.

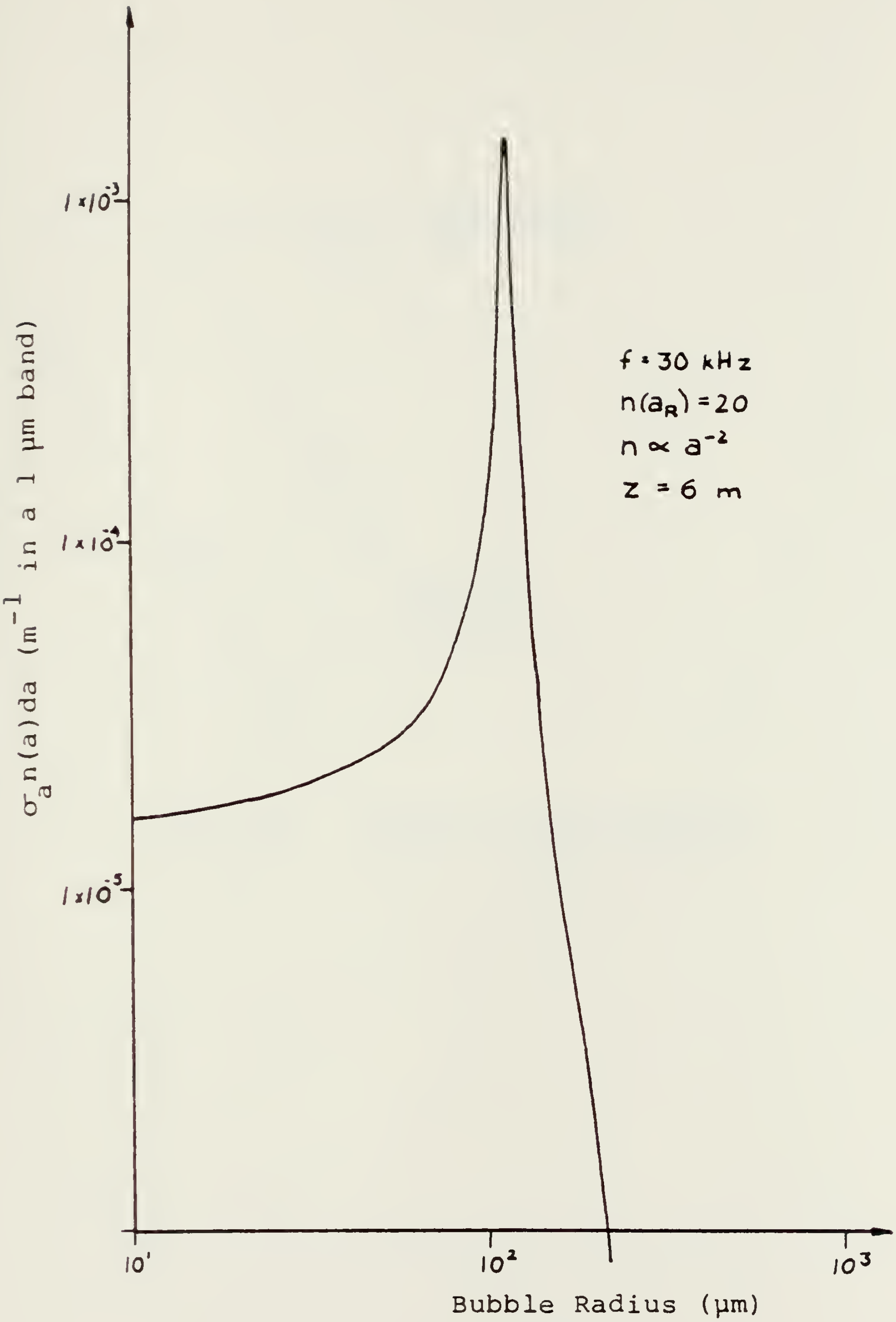

Fig. 37. $\sigma_a(a)n(a)da$ for 30 kHz.

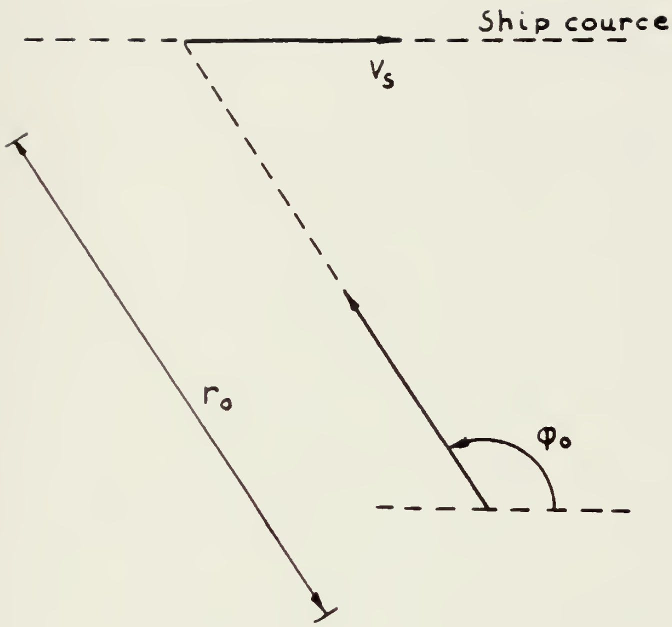

Fig. 38. Pursuit Homing Geometry.

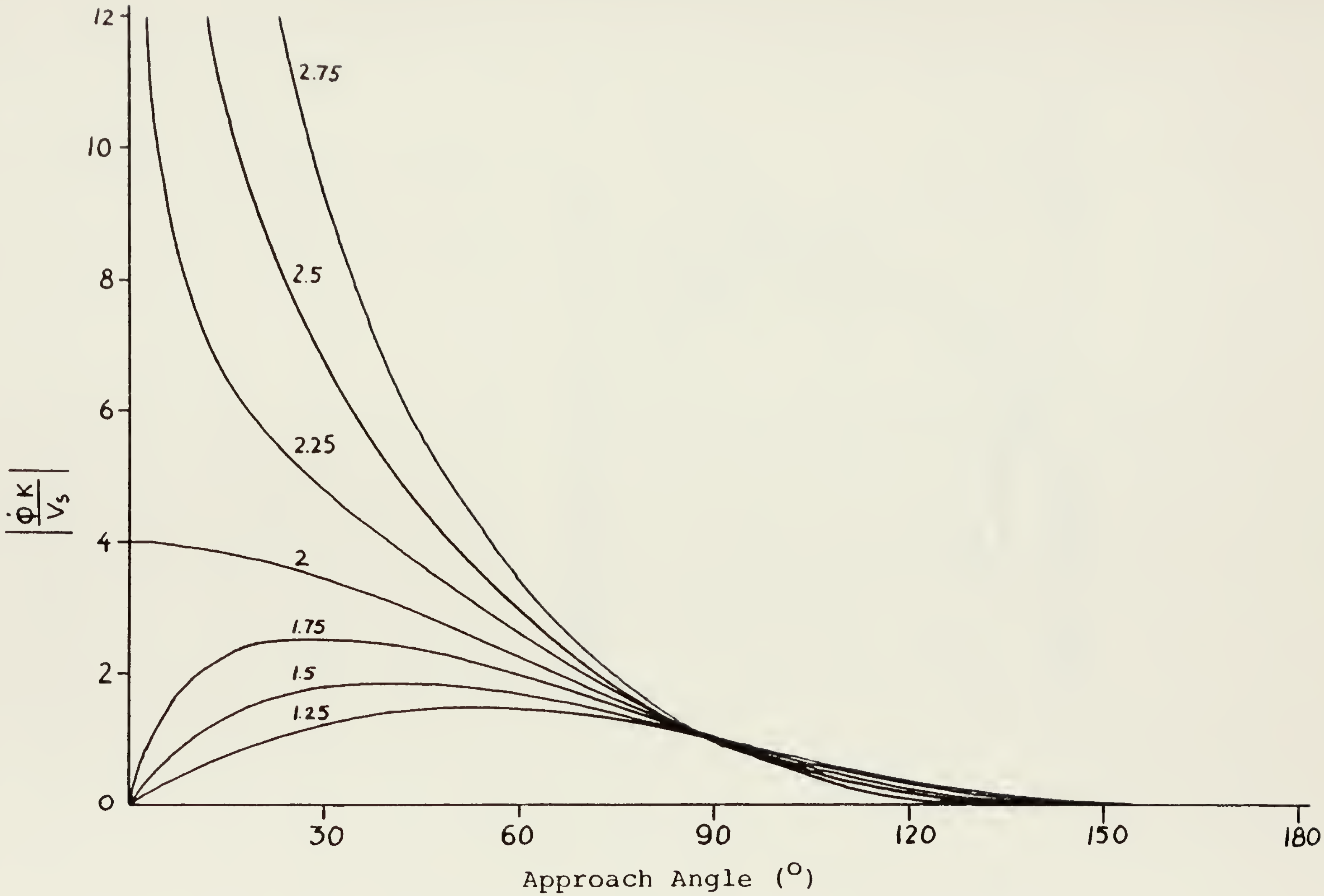

Fig. 39. $|\dot{\phi}K/V_s|$ as a Function of ϕ With Parameter p.

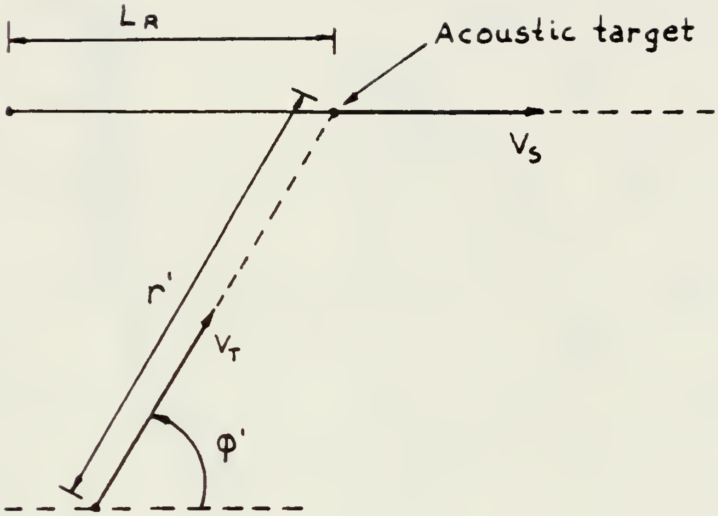

Fig. 40. Hit Criterion Geometry.

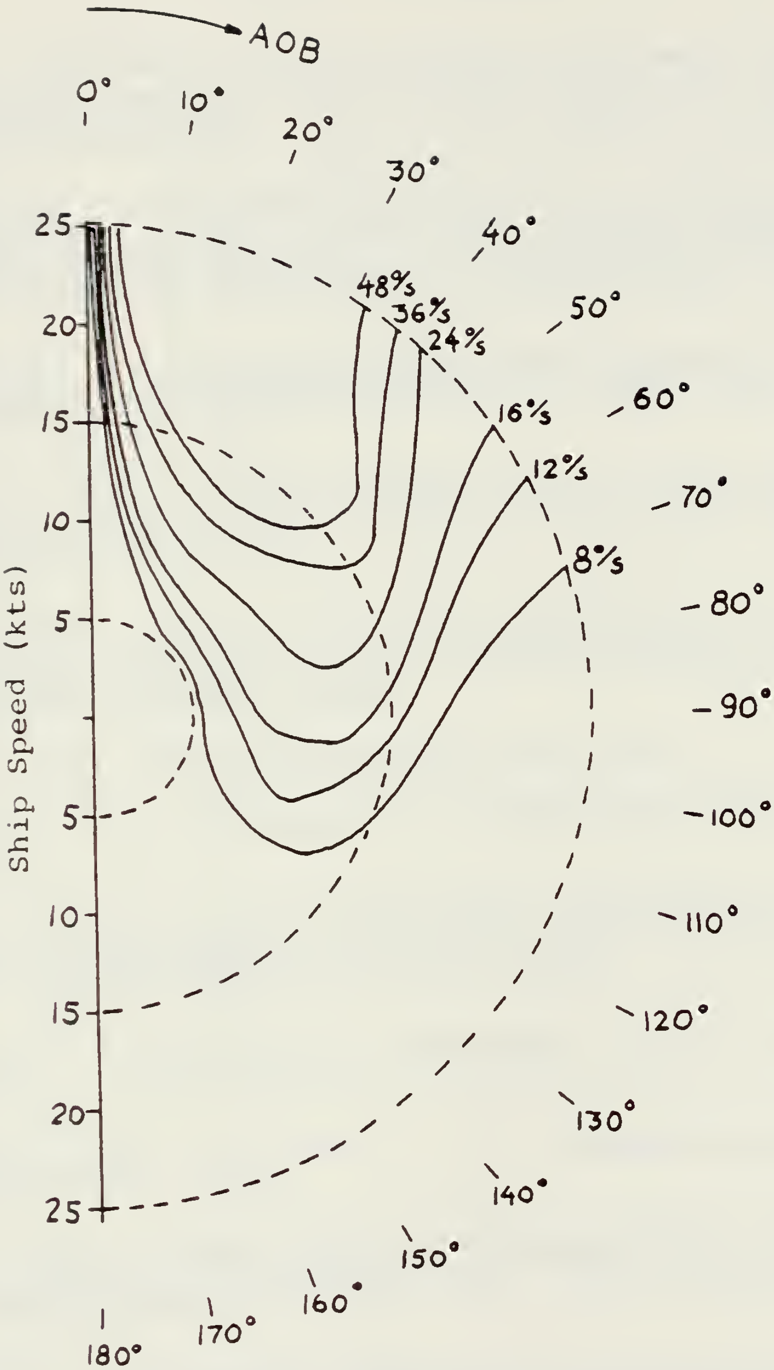

Fig. 41. AOB-limitation Versus Ship Speed with Parameter Maximum Turn Rate.

LIST OF REFERENCES

1. IKU (Continental Shelf Institute, Norway), Bölgedata fra Kontinetalsokkelen (translated, Wave Data from the Continental Shelf), IK U B 772/77/TA/mg, October 1977.

2. Lövik, A., Akustisk Måling av Vind og Bölgeinduserte Gassbobler i Havet (translated, Acoustic Measurements of Wind and Wave Induced Air Bubbles in the Ocean), NTH ELAB Report STF 44A7914, pp. 15-16, May 1979.

3. Medwin, H., In Situ Acoustic Measurements of Bubble Populations in Coastal Waters, J. Geoph. Res., V. 75, pp. 599-611, 1971.

4. Wenz, G. M., Acoustic Ambient Noise in the Ocean Spectra and Sources, J.A.S.A., V. 34, pp. 1936-1956, 1962.

5. Norwegian Defence Research Establishment, Devision for Underwater Warfare, Typical Sound Velocity Curves in Norwegian Coastal Waters.

6. U.S. Navy, N.O. Publication 700, 1969.

7. Urick, R. J., Principles of Underwater Sound, McGraw-Hill, 1975.

8. Thorp, W. H., Deep Ocean Sound Attenuation in the Sub- and Low-Kilocycle-per-Second Region, J.A.S.A., V. 38, pp. 648-654, 1965.

9. Ross, D., Mechanics of Underwater Sound, Pergamon Press, 1976.

10. Morse, P.M. and Ingard, K. V., Theoretical Acoustics, McGraw-Hill, 1968.

11. Lövik, A., A Theoretical and Experimental Investigation on Propeller Cavitation Noise, NTH ELAB Report STF 44A80121, February 1980.

12. Lövik, A., Acoustic Detection of Gas Bubbles in Water, NTH ELAB Report STF 44A80122, pp. 25-38, February 1980.

13. Cox, C. S., and Munk, W. H., Measurements of the Roughness of the Sea Surface from Photographs of the Sun's Glitter, J. Optic, Soc. Am., V. 44, pp. 838-850, 1954.
Cox, C. S., and Munk, W. H., Statistics of the Sea Surface Derived from the Sun Glitter, J. Marine Res., V. 13, pp. 198-227, 1954.

14. Pierson, W. M., and Moskowitz, L., A Proposed Spectral Form for Fully Developed Wind Seas Based on Similarity Theory of S. A. Kitaigorodskic, J. Geoph. Res., V. 69, pp. 518.-5190, 1964.

15. Tolstoy, I. and Clay, C., Ocean Acoustics, McGraw-Hill, 1966.

16. Fortuin, L., The Wave Equation in a Medium with a Time-dependent Boundary, J.A.S.A., V. 53, pp. 302-305, 1972.

17. Beckmann, P., Shadowing of Randomly Rough Surfaces, Trans IEEE, Antenna Propagation, V. 13, pp. 384-388, 1965.

18. Wagner, R., Shadowing of Randomly Rough Surfaces, J.A.S.A., V. 41, pp. 138-147, 1967.

19. Kinsler, L. E. and Frey, A. R., Fundamental of Acoustics, Second Edition, Wiley, 1962.

20. Ishimaru, A., Wave Propagation and Scattering in Random Media, V. 2, Academic Press, 1978.

21. Clay, C. and Medwin, H., Acoustical Oceanography, Wiley, 1977.

22. Medwin, H., The Rough Surface and Bubbles Effect on the Sound Propagation in a Surface Duct, NPS-61Md71101A, October 1971.

23. Van Nostrand, D., Principles of Guided Missile Design, McGraw-Hill, 1955.

24. Texas Instruments Inc., TI Programmable 58/59 Math/Utilities, 1978.

25. Texas Instruments Inc., TI Programmable 58/59 Master Library, 1977.

INITIAL DISTRIBUTION LIST

		No. Copies
1.	Defense Technical Information Center Cameron Station Alexandria, Virginia 22314	2
2.	Library, Code 0142 Naval Postgraduate School Monterey, California 93940	2
3.	Department Chairman, Code 61 Department of Physics and Chemistry Naval Postgraduate School Monterey, California 93940	1
4.	NAVMATCOM NOR, Bureau of Weapons N-5078 Haakonsvern Norway	3
5.	KNM "TORDENSKJOLD," Torpedo-/mine-skolen N-5078 Haakonsver Norway	2
6.	Norwegian Defense Research Establishment Devision for Electronic P.O. Box 25, 2007 Kjeller Norway	1
7.	Norwegian Defense Establishment Devision for Underwater Warfare P.O. Box 115, N-3191 Horten Norway	1
8.	Professor K. E. Woehler, Code 61Wh Department of Physics and Chemistry Naval Postgraduate School Monterey, California 93940	1
9.	Professor H. Medwin, Code 61Md Department of Physics and Chemistry Naval Postgraduate School Monterey, California 93940	1
10.	CDR Y. D. Tronstad, RNoN Naustvg. 23, N-5088 Mjölkeråen Norway	3

Thesis
T8127
c.1

193706

Tronstad
The effect of scattering and absorption on noise from a cavitating noise source in the subsurface ocean layer.